

**POLISH ACADEMY OF SCIENCES**

**THERMODYNAMICS AND COMBUSTION COMMITTEE**

# **archives of thermodynamics**



**Wydawnictwo IMP  
Gdańsk**

---

**QUARTERLY**

---

**Vol. 37**

---

**2016**

---

**No. 4**

---

## Editorial Office

---

Archives of Thermodynamics

The Szewalski Institute of Fluid Flow Machinery, Fiszerza 14, 80-231 Gdańsk, Poland,

Tel.: (+48) 58-341-12-71 int. 141, E-mail: redakcja@imp.gda.pl

<http://www.imp.gda.pl/archives-of-thermodynamics/>

<http://at.czasopisma.pan.pl/>

© by the Polish Academy of Science

Publication funding of this journal is provided by resources of the Polish Academy of Sciences and the Szewalski Institute of Fluid-Flow Machinery PASci

### Terms of subscription outside Poland

Annual subscription rate outside Poland (2016) is 120 EUR. Price of single issue is 30 EUR. Back of previously published volumes are available on request. Subscription orders should be sent directly to **IMP PAN Publishers, The Szewalski Institute of Fluid-Flow Machinery PASci, ul. Fiszerza 14, 80-231 Gdansk, Poland**; fax: (+48) 58-341-61-44; e-mail: now@imp.gda.pl. Payments should be transferred to the bank account of IMP PAN: IBAN 28 1130 1121 0006 5498 9520 0011 at Bank Gospodarstwa Krajowego; Code SWIFT: GOSKPLPW

### Warunki prenumeraty w Polsce

Roczna prenumerata (2016 r.) wynosi 168 PLN. Cena pojedynczego numeru wynosi 42 PLN. Osiągalne są również wydania archiwalne. Zamówienia z określeniem okresu prenumeraty, nazwiskiem i adresem odbiorcy należy kierować bezpośrednio do Wydawcy (Instytut Maszyn Przepływowych im. R. Szewalskiego PAN, ul. Fiszerza 14, 80-231 Gdańsk, Aleksandra Nowaczewska, e-mail: now@imp.gda.pl). Wpłaty prosimy kierować na konto Instytutu Maszyn Przepływowych PAN nr 28 1130 1121 0006 5498 9520 0011 w Banku Gospodarstwa Krajowego

### Articles in *Archives of Thermodynamics* are abstracted and indexed within:

Applied Mechanics Reviews • BazTech • Arianta • Baidu Scholar • Cabell's Directory • Celdes • Chemical Abstracts Service (CAS) - CAplus • CNKI Scholar (China National Knowledge Infrastructure) • CNPIEC • DOAJ • EBSCO (relevant databases) • EBSCO Discovery Service • Elsevier - SCOPUS • Genamics JournalSeek • Google Scholar • Inspec • Index Copernicus • J-Gate • Journal TOCs • Naviga (Softweco) • Paperbase • Pirabase • POL-index • Polymer Library • Primo Central (ExLibris) • ProQuest (relevant databases) • ReadCube • Referativnyi Zhurnal (VINITI) • SCImago (SJR) • Summon (Serials Solutions/ProQuest) • TDOne (TDNet) • TEMA Technik und Management • Ulrich's Periodicals Directory/ulrichsweb • WorldCat (OCLC)

Online ISSN 2083-6023

DE GRUYTER – <http://www.degruyter.com/view/j/aoter>

Typeset in L<sup>A</sup>T<sub>E</sub>X

## Condensation of refrigerant R407C in multiport minichannel section

TADEUSZ BOHDAL  
HENRYK CHARUN  
MAŁGORZATA SIKORA\*

Technical University of Koszalin, Department of Heat and Refrigeration Engineering, Raławicka 15-17, 75-620 Koszalin, Poland

**Abstract** Analysis of the state-of-the-art in research of refrigerant condensation in miniature heat exchangers, so-called multiports, was made. Results of refrigerant R407C condensation in a mini condenser made in the form of two bundles of tubular minichannels from stainless steel with an inside diameter 0.64 mm and length 100 mm have been presented. Two exchangers consisted of four minichannels and 8 minichannels have been investigated. The values of average heat transfer coefficient and frictional pressure drops throughout the condensation process were designated. The impact of the vapor quality of refrigerant and the mass flux density on the intensity of heat transfer and flow resistance were illustrated. A comparative analysis of test results for various refrigerants in both mini heat exchangers were made.

**Keywords:** Condensation; Minichannels; R407C refrigerant; Heat exchanger

### Nomenclature

- $A$  – inner surface of the heat transfer,  $m^2$   
 $d$  – diameter, m  
 $f$  – functional symbol  
 $G$  – mass flux density,  $kg/(m^2s)$   
 $L$  – length, m  
 $\dot{m}$  – mass flux,  $kg/s$

---

\*Corresponding Author. E-mail: malgorzata.sikora@tu.koszalin.pl

$n$	–	number of minichannels
$p$	–	pressure, Pa
$\Delta p$	–	pressure drop, Pa
$q$	–	heat flux density, W/m <sup>2</sup>
$\dot{Q}$	–	heat flux from electric heating, W
$T$	–	temperature, °C
$x$	–	vapour quality,

**Greek symbols**

$\alpha$	–	heat transfer coefficient, W/(m <sup>2</sup> K)
$\rho$	–	mass density, kg/m <sup>3</sup>

**Subscripts**

$a$	–	average
$f$	–	fluid
$s$	–	saturation
$w$	–	wall

## 1 Introduction

At the turn of the XX and XXI century was observed a rapid development of technological progress. It is manifested by qualitative and quantitative increase in production of equipment, especially in the two fields: in the aerospace and electronics. These fields are inextricably linked and determine the trend of these devices miniaturization. It should be noted that the absolute value of thermal power in computer systems is not very large, but the heat flux density, with is the amount of heat transferred by the heat exchange surface area reaches a significant value, even more than 1000 W/cm<sup>2</sup>, as indicated by Baummer *et al.* [1]. The traditional ways of transmitting or receiving such heat flux density are not very useful. Discussion of current methods and recommendations for future includes work of the Obhan and Garimella [15]. The use of two-phase flow, mediating in the heat exchange is a priority in these situations. The practical utilization is reduced to implementation of the convective heat exchange intensification methods with the phase changes. One of the passive methods of the convective heat transfer intensification process is to reduce the channels internal diameter for the agents with implementing the process of heat transfer [12,14]. The measure of the effectiveness of this intensification is increase of the heat transfer coefficient. It can be said that the construction of modern refrigeration and air conditioning heat exchangers should meet the technical and environmental criteria, like: compact dimensions, high heat transfer efficiency, and minimal impact on the environment [3,4,13].

Due to the withdrawal of refrigerant R134a from use, more often are used new, high pressure refrigerants like R404A, R410A, and R407C. From the world literature review results that R407C refrigerant is recommended to use in near future. This zeotropic refrigerant is problematic because of a high temperature glide. Review of the modern calculation methods for heat transfer coefficient and pressure drop in the condensation in conventional and minichannels was reviewed and discussed in [9]. Authors show the usefulness of Silver-Bell-Ghaly [17,3], Thome [18], and Cavallini *et al.* [8] calculation methods. These methods are developed based on a mechanism of zeotropic mixtures flow condensation. Honda *et al.* [10] performed a comparative study of heat transfer during condensation of R407C and R22 refrigerants in a horizontal pipe with an internal diameter approximately 5.38 mm with microfins. It was shown that the heat transfer coefficient of R407C was lower than that of R22, and significant differences existed for smaller values of the vapor quality. In the paper by Lie *et al.* [11] were presented the experimental results of R407C and R134a refrigerants boiling in horizontal smooth tubes with internal diameters of 0.83 mm and 2 mm for mass flux density  $G = 200\text{--}400\text{ kg/m}^2\text{s}$ , heat flux density  $q = 5\text{--}15\text{ kW/m}^2$ , vapour quality  $x = 0.2\text{--}0.8$ , and saturation temperature  $T_s = 5\text{--}15\text{ }^\circ\text{C}$ . In the paper was shown that the friction pressure drop for R407C boiling in minichannels is lower than for R134a. The authors developed their own empirical correlations. The paper of Zhang *et al.* [19] presented the results of R22, R410A, and R407C refrigerant condensation in single circular minichannels with internal diameters of 1.088 and 1.289 mm, with parameters in the ranges of:  $T_s = 30\text{--}40\text{ }^\circ\text{C}$ ,  $G = 300\text{--}600\text{ kg/m}^2\text{s}$ ,  $x = 0.1\text{--}0.9$ . As expected, it was found that pressure drops increase when the mass flux density,  $G$ , and vapor quality,  $x$ , increase, but in the range of  $x > 0.8$ , this influence is much smaller. This underlined the dependence of the two-phase flow regime type on the flow resistance. For higher values of  $x$ , there was observed a transition from the annular flow to the mist flow. Additionally, the influence of the channel diameter and refrigerant type on pressure drops was shown [5].

## 2 Experimental investigations

### 2.1 Object of the experiments

The object of the experimental studies were two bundles of tubular minichannels (multiports) of the design shown in Fig. 1. Bundle of the tubular

minichannels called, MULTI-4 consisted, of 4 minichannels made from stainless steel with an internal diameter  $d = 0.64$  mm and length  $L = 100$  mm. In the case of tube bundle called MULTI-8 uses an 8 tubular minichannels with the same internal diameter and length.

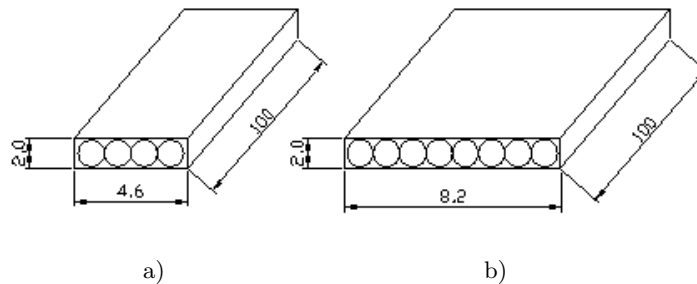


Figure 1: Dimensional diagram of the testing minichannels bundles: a) MULTI-4, b) MULTI-8.

## 2.2 Testing facility

The experimental investigations were made on the test stand, which diagram is showed in Fig. 2, and external appearance in Fig.3 [6,7]. The basic element of the test stand was a operating distance (1), along with the testing mini heat exchanger. It was placed in the horizontal axis of the rectangular water channel 2 made of aluminum with internal dimensions of  $28 \times 24$  mm. To measure section (1) refrigerant was brought from the compressor (3) discharge side. Prior to flow to the minichannel inlet section the superheated steam of refrigerant flows through a tube in tube heat exchanger (10) cooled with water. The application of this heat exchanger is not only allowed to the removal of overheating heat, but also for the preparation of refrigerant in the form of dry saturated steam with a vapor quality  $x = 1$  (or close to this state). After condensation of the refrigerant vapor flow through miniature heat exchanger, the refrigerant liquid flow to sub cooler (11), from which the flow rate of refrigerant through was measured by Coriolis flowmeter (15). Control posts were also measured the refrigerant mass flow rate through the vascular system hallmarked. Then the refrigerant returns to the refrigeration system supplied with the unit (3), with air-cooled condenser (4) and the lamelled air cooler (8). Tubular minichannels included in the multiport were supplied parallel of refrigerant according to the diagram in Fig. 3.

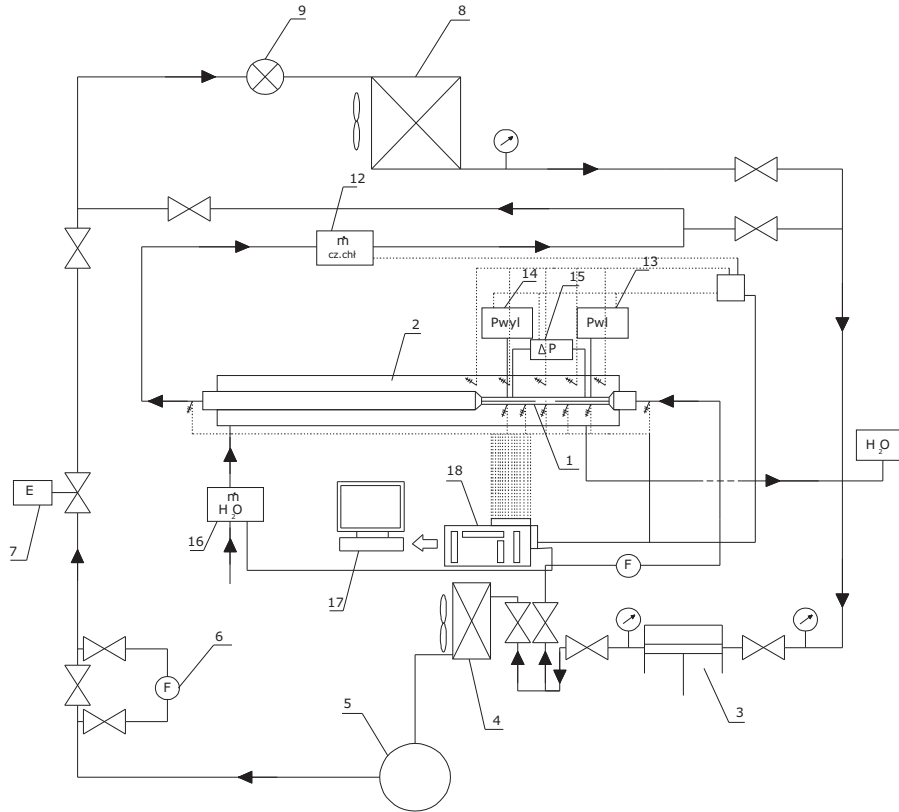


Figure 2: Schematic diagram of the test stand: 1 – test section, 2 – water channel, 3 – refrigeration compressor installation, 4 – air cooled condenser, 5 – liquid vessel, 6 – filter–dryer of refrigerant, 7 – electromagnetic valve, 8 – lamellated air cooler, 9 – expansion valve, 12 – electronic flowmeter of refrigerant, 13 – refrigerant’s pressure pickup on the inlet to the measuring section, 14 – refrigerant’s pressure pickup on the outlet to the measuring section, 15 – refrigerant’s differential pressure transducer, 16 – water electronic flowmeter, 17 – computer, 18 – data acquisition system.

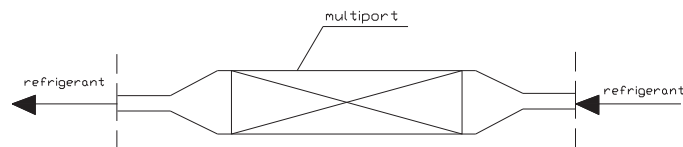


Figure 3: Supply diagram of the multiports minichannels by the refrigerant.

Multiports were mounted interchangeably as a part of measuring section (1) of the test stand shown in Fig. 2. On the length  $L$  of the multiport mounted nine K-type thermocouples to measure temperature distribution on multiports outer wall. After taking into account the thermal resistance and bringing the related corrections, specified average temperature of the pipe minichannels inner wall surface in that section. The cooling water temperature distribution in nine sections was also measured. Directly measured mass flux density of refrigerant condensing in the flow through the multiport and the heat flux density by the methodology proposed by the Shin and Kim [16].

This method consists of heat transfer coefficient determination from the water side at a specific temperature difference of the minichannel wall,  $T_w$ , and water,  $T_f$ . Test section was heated by electric heater. The construction of the test section for this aim is shown in Fig. 4.

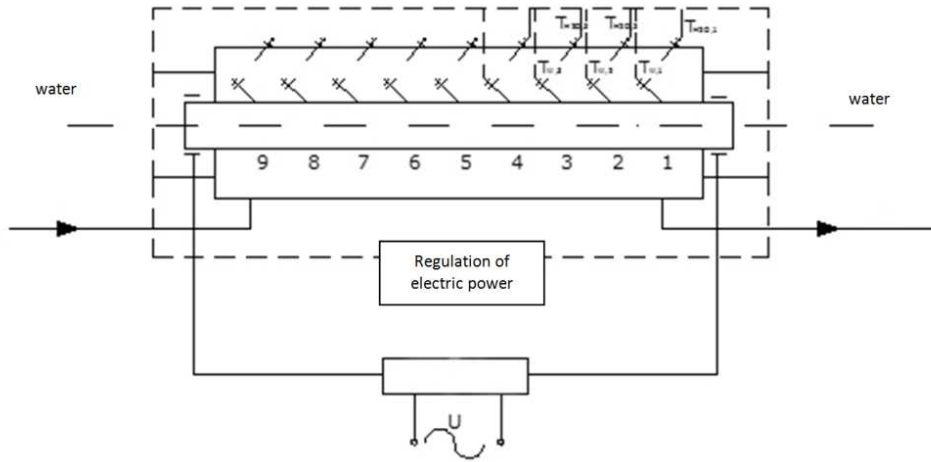


Figure 4: Scheme of the test section used for the indirect determination of heat amount received by cooling water in minichannel electrically heated.

In line with the law of Joule the heat flux density on a minichannel was specified :

$$q_i = \frac{\dot{Q}_i}{\pi d L_i}, \quad (1)$$

where  $L_i$  is the length of minichannel,  $\dot{Q}$  is the heat flux from electric heating, and subscript  $i$  denotes the number of cross-section.

Using the temperatures of channel wall  $T_w$  and cooling water  $T_f$  in chosen cross-section  $i$ , characteristics of  $q_i = f(T_{w,i} - T_{f,i})$  was made, which allow to calculate the heat flux density during condensation of refrigerant after measuring of wall and cooling water temperature (here  $f$  is the functional symbol).

Directly was measured also the refrigerant pressure at the inlet and outlet of multiport as well as the pressure drop,  $\Delta p$ , in the flow. These parameters allowed for determination of an average value of the vapor quality,  $x_a$ , and medium mass flux density  $G$ , pressure drop ( $\Delta p/L$ ), which enabled subsequently elaboration of the experimental thermal-hydraulic characteristics of the condensation process.

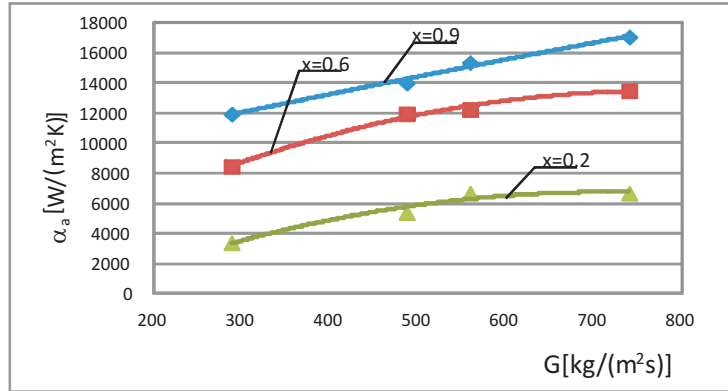
### 3 Results of the investigations

An experimental heat-flow researches were performed for condensation of the R407C refrigerant in multiports MULTI-4 and MULTI-8 (Fig. 1). The average values of heat transfer coefficient and pressure drop were defined. Mass flux density of the refrigerant was determined from direct measurement of the mass flow rate of refrigerant at the inlet to multiport by using the relationship

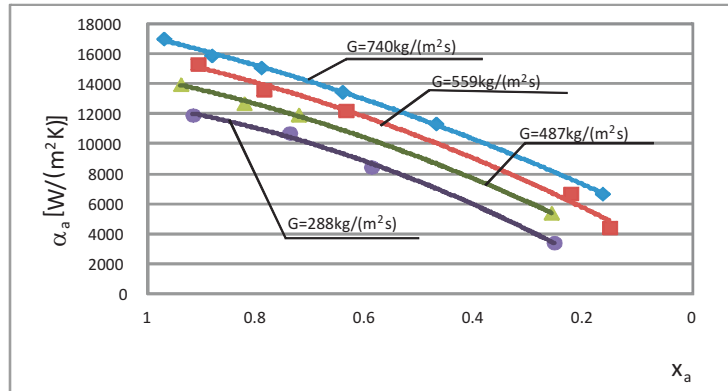
$$G = \frac{\dot{m}}{n \frac{\pi d^2}{4}}, \quad (2)$$

where  $\dot{m}$  is the mass flow,  $n$  is the number of minichannels parallel supplied ( $n = 4$  for MULTI-4 and  $n = 8$  for MULTI-8), and  $d$  is the internal diameter of the minichannel ( $d = 0.64$  mm). The heat transfer density,  $q$ , is related to  $1 \text{ m}^2$  multiport inner surface of the heat transfer:  $A = n \pi d L$ , where  $L$  is the length of minichannels in multiport.

Figures 5–7 shows the dependence of the average (marked with subscript  $a$ ) heat transfer coefficient,  $\alpha_a$ , and flow resistance,  $(\Delta p/L)_a$ , in two models of interpretation, first when the mass flux density,  $G$ , with  $x_a = \text{const}$ , and second when it dependence on the  $x_a$ , the  $G = \text{const}$ .

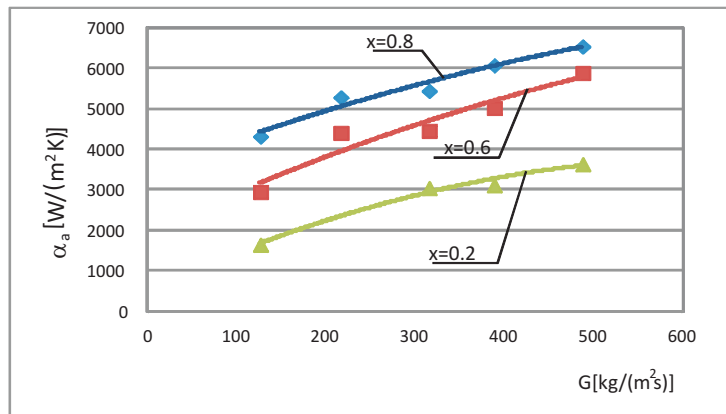


a)

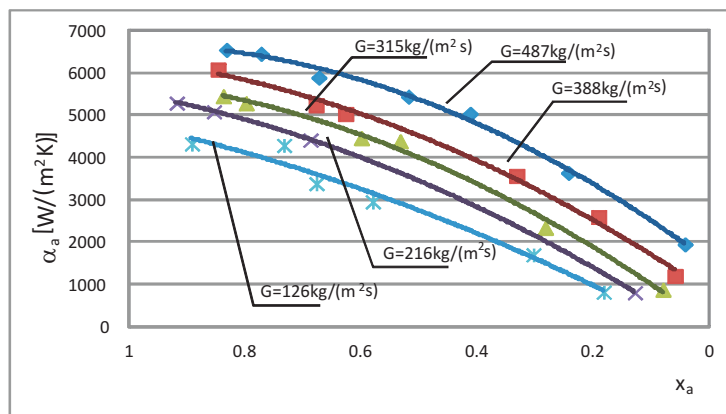


b)

Figure 5: Experimental investigation results of the dependence of the average heat transfer coefficient,  $\alpha_a$ , on: a) mass flux density,  $G$ , for  $x_a = \text{const}$ ; b) average vapor quality,  $x_a$ , for  $G = \text{const}$ ; multipoint MULTI-4, refrigerant – R407C.

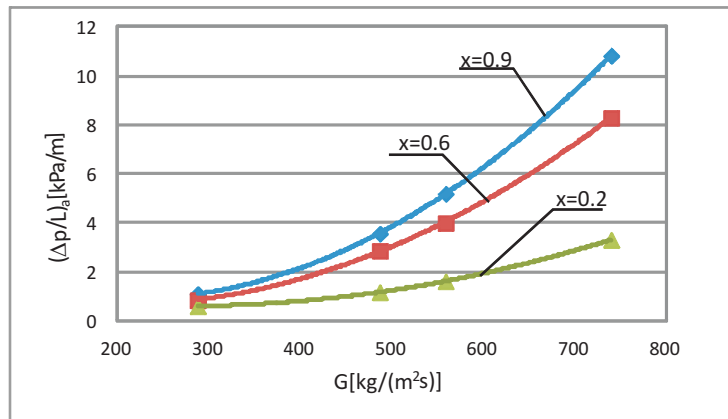


a)

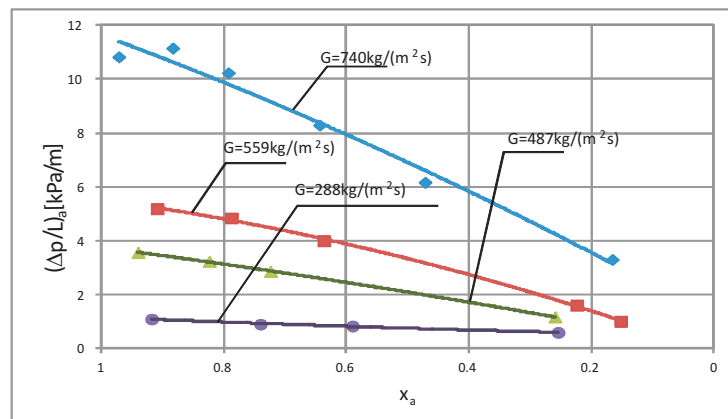


b)

Figure 6: Experimental investigation results of the dependence of the average heat transfer coefficient,  $\alpha_a$ , on: a) mass flux density,  $G$ , for  $x_a = \text{const}$ ; b) average vapor quality,  $x_a$ , for  $G = \text{const}$ ; multiport MULTI-8, refrigerant – R407C.

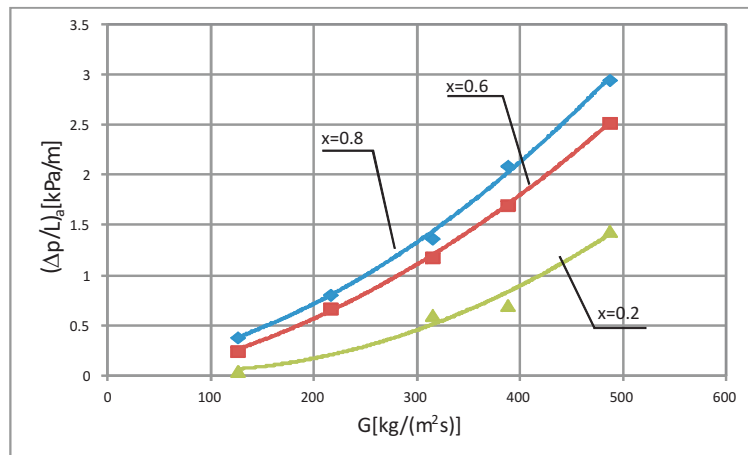


a)

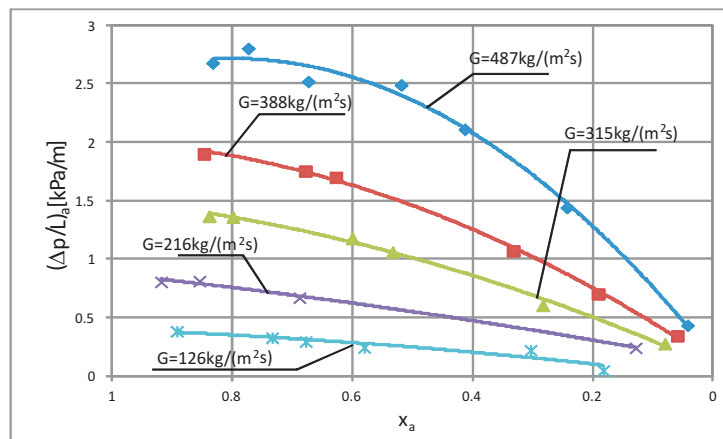


b)

Figure 7: Experimental investigation results of the dependence of the average pressure drop,  $(\Delta p/L)_a$ , on: a) mass flux density,  $G$ , for  $x_a = \text{const}$ ; b) average vapor quality,  $x_a$ , for  $G = \text{const}$ ; multiport MULTI-4, refrigerant – R407C.



a)



b)

Figure 8: Experimental investigation results of the dependence of the average pressure drop,  $(\Delta p/L)_a$ , on: a) mass flux density,  $G$ , for  $x_a = \text{const}$ .; b) average vapor quality,  $x_a$ , for  $G = \text{const}$ .; multiport MULTI-8, refrigerant – R407C.

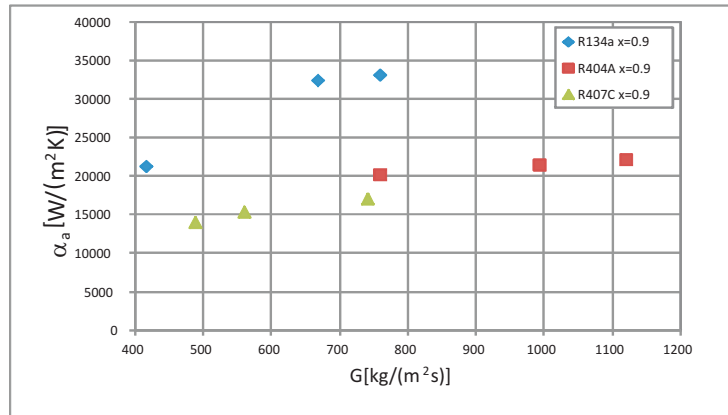
## 4 Analysis of experimental results

The heat-flow characteristics of R407C refrigerant condensation allow for a comparative analysis of the test parameters. They concerned the condensation in tubular multiports MULTI-4 and MULTI-8 (Fig. 1), which differed in the number of tubular minichannels. Based on the analysis, the following observations can be made.

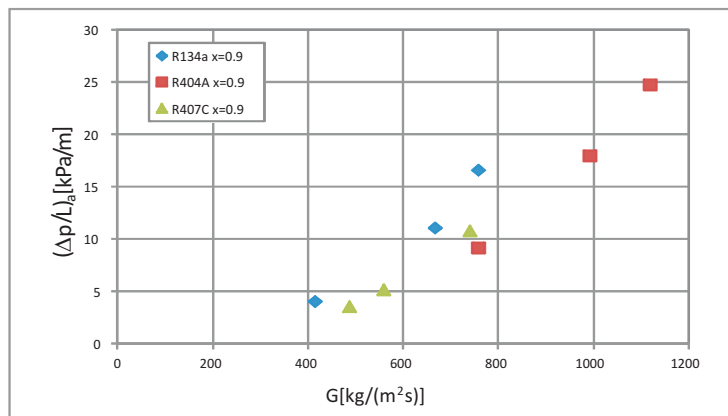
Thermal characteristics of condensation in type  $\alpha_a = f(G)$ , for a constant level of average vapor quality  $x_a = \text{const}$  showed an increase in the average heat transfer coefficient,  $\alpha_a$ , with increase in mass flux density,  $G$  of refrigerant. On the basis of diagrams the characteristics of  $\alpha_a = f(x_a)$ , with  $G = \text{const}$  shows that the  $\alpha_a$  coefficient decreases when average vapor quality,  $x_a$ , decrease too. The nature of these average thermal characteristics direction and the average flow resistance characteristics is similar to the characteristics obtained for the condensation process in single minichannels [12].

In the case of multiport, which is fed by  $n$  number parallel minichannels, mass flux density was calculated from Eq. (1). This means that for the same values of mass flow rate,  $\dot{m}$ , the average mass flux density,  $G$ , in multiports made from  $n$  minichannels is  $n$  times smaller (and decreases with increasing on number of parallel minichannels). This results in effects on the value of the heat transfer coefficient,  $\alpha_a$ . For the same value  $\dot{m} = \text{const}$  flowing to the multiport, value of the average heat transfer coefficient,  $\alpha_a$ , is growing when the process takes place in a single minichannel, and for multiport MULTI-4 is also higher than for the MULTI-8. It is interesting to compare the characteristics of condensation process obtained according to the type of a refrigerant [7]. Figures 9 and 10 show a example characteristics for MULTI-4 and MULTI-8.

Figure 9 presents a comparative approach to the effects of three refrigerants (R134a, R407C, and R404A) on the thermal and flow characteristics of condensation in multiport from 4 minichannels MULTI-4. The results show that for R134a refrigerant obtained the highest values of the average heat transfer coefficient  $\alpha_a$  (and the pressure drop  $(\Delta p/L)_a$ ). Refrigerant R134a is an intermediate pressure refrigerant (in terms of pressure and saturation temperature during the condensation process). Refrigerants R407C and R404A belong to a group of high-pressure refrigerants. Value of the  $\alpha_a$  coefficient and pressure drop  $(\Delta p/L)_a$  are higher for the R404A refrigerant then for R407C, but this increase is in the range from 10 to 15%. Figure 10 shows a comparison of thermal and flow characteristics for R134a



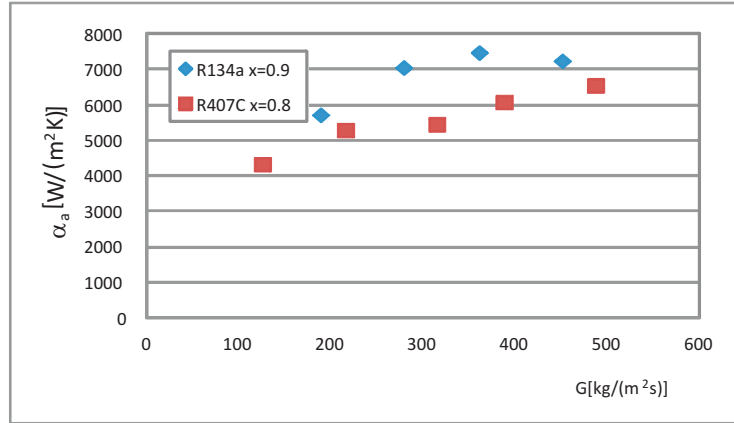
a)



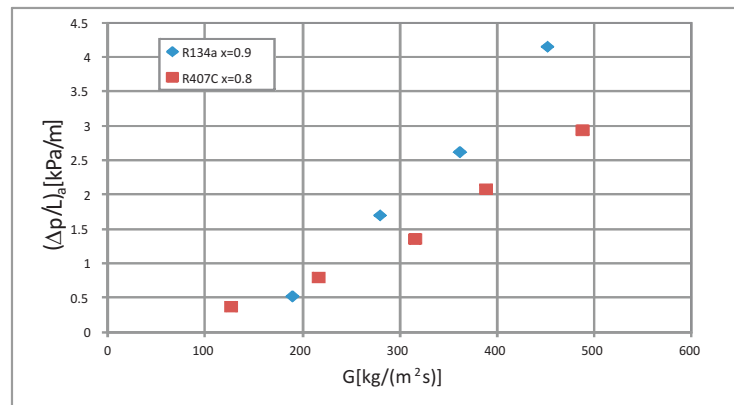
b)

Figure 9: Sample comparative characteristics of the condensation of R134a, R407C and R404A refrigerants in multiport MULTI-4, for  $x_a = 0.9$ : a)  $\alpha_a = f(G)$ , b)  $(\Delta p/L)_a = f(G)$ .

and R407C refrigerants for multiport MULTI-8. The increase in flow resistance for R407C refrigerant is a lack of acceptance for the analysis of the test results at a lower average vapor quality.



a)



b)

Figure 10: Sample comparative characteristics of the condensation of R134a, R407C and R404A refrigerants in multiport MULTI-8, for  $x_a = 0.9$ : a)  $\alpha_a = f(G)$ , b)  $(\Delta p/L)_a = f(G)$ .

## 5 Conclusions

Analysis of the diagrams Leads to the following conclusions:

1. Construction of the compact condensers built on the minichannels contain elements of the multiports forming the heat exchange area. Current state of knowledge in the field of the heat transfer and pressure drop during refrigerants condensation in multiports is definitely unsatisfactory.

2. The results of thermal flow experimental tests of the R134a, R404A, and R407C condensation in multiports from 4 – and 8 minichannels parallel fed, showed that the highest values of average heat transfer coefficient and pressure drop were obtained for R134a.
3. Knowledge of the average values of the heat transfer coefficient and pressure drop during condensation of the refrigerants in multiports is very important for the designers of this miniature heat exchangers type. Raising awareness of energy transfer mechanisms during phase changing in multiports should include their local assessment, depending on vapor quality  $x$  changes. This is also the need to test for other sections of the multiport.

**Acknowledgements** This work was sponsored by the State Committee for Scientific Research, Grant No. N N 512 456 740

*Received 11 December 2012*

## References

- [1] BAUMMER T., CETEGEN E., OHADI M., DESSIATOUN S.: *Force fed evaporation and condensation utilizing advanced microstructured surfaces and microchannels*. Microelectronics J. **39**(2008), 7, 975–980.
- [2] BELL K.J., GHANY M.A.: *An approximate generalized design method for multicomponent partial condenser*. AIChE Symp. Ser. **69**(1973), 131, 72–79.
- [3] BOHDAL T., CHARUN H., KUCZYŃSKI W.: *Investigation of the condensation process in the mini-systems of compressor refrigerating systems*. In: Proc. Conf. COMPRESORS'2009, 1–8.
- [4] BOHDAL T., CHARUN H., SIKORA M.: *Heat transfer during condensation of refrigerants in tubular minichannels*. Arch. Thermodyn. **33**(2012), 2, 3–22.
- [5] BOHDAL T., CHARUN H., SIKORA M.: *Empirical study of heterogeneous refrigerant condensation in pipe minichannels*. Int. J. Refrig. **59**(2015), 210–223.
- [6] BOHDAL T., CHARUN H., KUCZYŃSKI W., SIKORA M.: *Investigation of heat exchange and flow resistances during condensation of refrigeration media in minichannels*. In: Proc. 19th Int. Symp. Research-Education-Technology, 2009 Bremen, 118–121.
- [7] BOHDAL T., CHARUN H., SIKORA M.: *Comparative investigations of the condensation of R134a and R404A refrigerants in pipe minichannels*. Int. J. Heat Mass Trans. **54**(2011), 9-10, 1963–1974.

- [8] CAVALLINI A., CENSI G., DEL COL D., DORETTI L., ROSSETTO L.: *Heat transfer coefficient HFC refrigerants during condensation at high temperature inside a enhanced tube*. In: Proc. Int. Refrigeration and Air Conditioning Conf., Purdue Place Uni., 2002, 563, R8-2.
- [9] FRONK B.M., GARIMELLA S.: *In-tube condensation of zeotropic fluid mixtures: A review*. Int. J. Refrig. **36**(2013), 534–561.
- [10] HONDA H., WIJAYANTA A.T., TAKATA N.: *Condensation of R407C in a horizontal microfin tube*. Int. J. Refrig. **28**(2005), 2, 203–211.
- [11] LIE Y.M., SU F.Q., LAI R.L., LIN T.F.: *Experimental study of evaporation pressure drop characteristics of refrigerants R134a and R407C in horizontal small tubes*. Int. J. Heat Mass Trans. **51**(2008), 1-2, 294–301.
- [12] MIKIELEWICZ D.: *Boiling and condensation in flow in the channels and minichannels*. Wyd. Uczelniane Politechniki Gdańskiej, Gdańsk 2009.
- [13] MIKIELEWICZ D., ANDRZEJCZYK R.: *Comparative study of flow condensation in conventional and small diameter tubes*. Arch. Thermodyn. **33**(2012), 2, 67–83.
- [14] MISHIMA K., HIBIKI T.: *Effect of inner diameter on some characteristics of air-water two-phase flow in capillary tubes*. Trans. ISME B **61**(1995), 589, 99–106.
- [15] OBHAN C.B., GARIMELLA S.: *A comparative analysis of studies on heat transfer and fluid flow in microchannels*. Microscale Thermophys. **5**(2001), 4, 293–311.
- [16] SHIN J.S., KIM M.H.: *An experimental study of condensation heat transfer inside a mini-channel with a new measurement technique*. Int. J. Multiphase Flow **30**(2004), 3, 311–325.
- [17] SILVER L.: *Gas cooling with aqueous condensation*. Trans. Inst. Chem. Eng. **25**(1947), 30–42.
- [18] THOME J.R.: *Condensation in plain horizontal tubes: Recent advances in modeling of the transfer to pure fluids and mixture*. J. Braz. Soc. Mech. Sci. Eng., **27**(2005), 1, 23–30.
- [19] ZHANG H.-Y., LI J.-M., LIU N., WANG B.-X.: *Experimental investigation of condensation heat transfer and pressure drop of R22, R410 and R407C in mini-tubes*. Int. J. Heat Mass Trans. **55**(2012), 13-14, 3522–3532.
- [20] MIKIELEWICZ D., ANDRZEJCZYK R., JAKUBOWSKA B., MIKIELEWICZ J.: *Analytical model with non-adiabatic effects for pressure drop and heat transfer during boiling and condensation flows in conventional channels and minichannels*. Heat Transfer Eng. **37**(2016), 13-14, 1158–1171.

## The methodology of the gas turbine efficiency calculation

JANUSZ KOTOWICZ  
MARCIN JOB  
MATEUSZ BRZĘCZEK\*  
KRZYSZTOF NAWRAT  
JANUSZ MĘDRYCH

Silesian University of Technology, Institute of Power Engineering and Turbomachinery, Konarskiego 18, 44-100 Gliwice, Poland

**Abstract** In the paper a calculation methodology of isentropic efficiency of a compressor and turbine in a gas turbine installation on the basis of polytropic efficiency characteristics is presented. A gas turbine model is developed into software for power plant simulation. There are shown the calculation algorithms based on iterative model for isentropic efficiency of the compressor and for isentropic efficiency of the turbine based on the turbine inlet temperature. The isentropic efficiency characteristics of the compressor and the turbine are developed by means of the above mentioned algorithms. The gas turbine development for the high compressor ratios was the main driving force for this analysis. The obtained gas turbine electric efficiency characteristics show that an increase of pressure ratio above 50 is not justified due to the slight increase in the efficiency with a significant increase of turbine inlet combustor outlet and temperature.

**Keywords:** Gas turbine; Polytropic efficiency; Isentropic efficiency

### Nomenclature

0 – 9 – characteristic points  
 $a$  – air / flue gas  
 $AF$  – air filter

---

\*Corresponding Author. E-mail: mateusz.brzeczek@polsl.pl

$c$	–	cooling air
$C$	–	compressor
$CCGT$	–	combined cycle gas turbine
$CCH$	–	combustor chamber
$CO$	–	cooler
$COT$	–	combustor outlet temperature
$\bar{C}$	–	average specific heat
$G$	–	generator
$LHV$	–	lower heating value
$\dot{m}$	–	mass flow
$p$	–	pressure
$R$	–	individual gas constant value
$SC$	–	simple cycle
$t$ or $T$	–	temperature
$T$	–	turbine
$TBC$	–	thermal barrier coatings
$TIT$	–	turbine inlet temperature
$\dot{Q}$	–	heat flux
( $C$ )	–	conservative scenario
( $O$ )	–	optimistic scenario

#### Greek symbols

$\beta$	–	pressure ratio
$\Delta$	–	derivation
$\eta$	–	efficiency
$\tilde{\mu}$	–	polytropic exponent

#### Subscripts

$CCGT$	–	combined cycle gas turbine
$el$	–	electrical
$est$	–	establish
$f$	–	fuel
$FC$	–	fuel compressor
$gross$	–	gross
$GT$	–	gas turbine
$i$	–	internal/isentropic
$in$	–	inlet
$m$	–	mechanical
$max$	–	maximal
$net$	–	net
$out$	–	outlet
$p$	–	polytropic
$s$	–	waste heat
$ST$	–	steam turbine
$t$	–	thermal
$\zeta$	–	pressure loss
$\cdot$	–	division of subscripts

**Superscripts**

$C$	–	compressor
$p$	–	polytropic
$T$	–	turbine
$\eta$	–	efficiency
$\tilde{\mu}$	–	polytropic exponent

**1 Introduction**

Gas turbines are the machines consisting of the air compressor and the expander, mostly connected together by common shaft, and of a combustion chamber placed between them. In the energy sector these machines are used as an autonomous units called simple cycle (SC) or as a components of a gas turbine combined cycle gas turbine units (CCGT). The simple cycle units are characterized by lower powers and light, container-construction allowing for easy transport. Gas turbines used in CCGT units often have electric power exceeding 300 MW. In countries such as Poland, where the ratio of natural gas to coal prices is unfavorable – SC units are not built due to the lack of investment profitability, gas turbines are working there only in a combined cycle [1–3].

Thermal efficiency of CCGT units is defined by the relationship

$$\eta_{t\ CCGT} = \frac{N_{iGT} + N_{iST}}{\dot{Q}_{in}}, \quad (1)$$

where  $N_{iGT}$ ,  $N_{iST}$  are internal power of gas turbine and steam turbine, respectively, and  $\dot{Q}_{in}$  is a heat flow fed to the gas turbine. Equation (1) can be rewritten as

$$\eta_{t\ CCGT} = \eta_{t\ GT} + \eta_{t\ ST} (1 - \eta_{t\ GT}), \quad (2)$$

where  $\eta_{t\ GT}$  and  $\eta_{t\ ST}$  are the thermal efficiency of a gas turbine and steam turbine, respectively, and are defined as

$$\eta_{t\ GT} = \frac{N_{iGT}}{\dot{Q}_{in}}, \quad (3)$$

$$\eta_{t\ ST} = \frac{N_{iST}}{\dot{Q}_{4a}}, \quad (4)$$

where  $\dot{Q}_{4a}$  is a heat flow at the gas turbine outlet. Relationship (2) is presented graphically in Fig. 1.

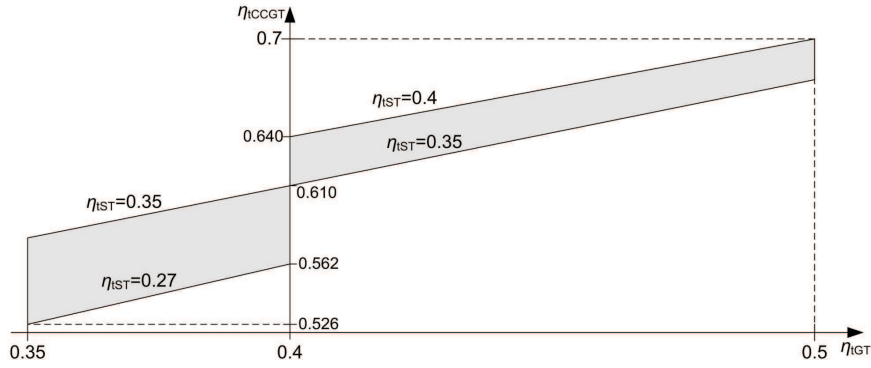


Figure 1: Thermal efficiency of the CCGT unit in a function of gas turbine and steam turbine cycle thermal efficiencies.

Currently achieved thermal efficiency of the gas turbines are around 40%, and the steam turbine cycle they are up to above 35%. Thus, the left side of vertical axis shows the currently achieved efficiency of the CCGT units. The right side of Eq. (2) represents the potential for increasing the CCGT efficiency. The derivation of Eq. (2) returns the condition for the CCGT efficiency increase

$$\Delta\eta_{tCCGT} = \frac{\partial\eta_{tCCGT}}{\partial\eta_{tGT}}\Delta\eta_{tGT} + \frac{\partial\eta_{tCCGT}}{\partial\eta_{tST}}\Delta\eta_{tST}. \quad (5)$$

Based on Eq.(5) for the values of  $\Delta\eta_{tGT} = 0.4$  and  $\Delta\eta_{tST} = 0.35$  the derivatives of  $\frac{\partial\eta_{tCCGT}}{\partial\eta_{tGT}} \cong 0.65$  and  $\frac{\partial\eta_{tCCGT}}{\partial\eta_{tST}} \cong 0.6$  are determined [1,2]. This means that the increase in the gas turbine efficiency  $\Delta\eta_{tGT}$  by 1 pp translates into a higher CCGT efficiency increase than in the analogous rise in steam turbine cycle ( $\Delta\eta_{tST}$ ). This is the first argument suggesting a search direction to increase CCGT efficiency in the first place through the increase in gas turbine efficiency. The second, but much more important argument is the unit investment cost (referred to 1 MW of generated power), which in the case of the gas turbine installation are 4–5 times lower than in steam turbine part. Therefore, the present paper concentrates on gas turbines [3–7].

The gas turbine efficiency depends primarily on the compressor pressure ratio and the highest temperature in the cycle, which is the combustor outlet temperature (COT). However, usually considered as the most important temperature in the gas turbine cycle is the average turbine inlet temperature (TIT), defined by ISO-2314 standard. For stoichiometric combustion

conditions the COT would significantly exceed the value of 2000 °C. Today, most manufactures use the COT of 1500 °C. Only one of the leading producers introduced the COT at the level of 1600 °C, and conducts research towards the use of 1700 °C [8,9]. In comparison TIT achieves value range of 1300–1400 °C, rarely reaching 1500 °C.

Limitations of these temperatures result from the application of thermal barrier coatings (TBC), which cover elements exposed to the highest temperatures. Assumed that currently used TBC allow for continuous operation at a temperature not exceeding 1200 °C. Presently used cooling technologies allow for the flue gas temperature reduction at the cooled surface by  $\Delta t = 300\text{--}400$  K, therefore the highest temperature (COT or TIT) can reach 1500–1600 °C. Raising TIT by 100 to 200 K is associated with the increase in  $\Delta t$ , i.e., to the value  $\Delta t = 500\text{--}600$  K. Such actions were the object of scrutiny of producers more than 10 years ago [10,11], but there is no information in the literature about their realization. An exception is the paper Hada *et al.* [12], from Mitsubishi Heavy Industries, Ltd., which indicates that the key to the creation of a J-class turbine with  $TIT = 1600$  °C (M701J and M501J for 50 Hz and 60 Hz, respectively), i.e., the temperature higher by 100 °C than the reference G-class, was to improve cooling technology and search for materials with lower thermal conductivity of TBC. Each of them allowed to increase  $TIT$  by 50 °C. Data provided there also suggests that cooling technologies allow to reduce the surface temperature by  $\Delta t = 550$  K in the G-class turbine, while the TBC with lowered temperature by 50 K, allows to use the alloys with allowable temperature of 700–900 °C. For the J-class turbine the cooling technology reduces surface temperature by  $\Delta t = 600$  K, and the TBC by 100 K (hence  $TIT = 900 + 600 + 100 = 1600$ ; °C). In Japan there is also ongoing research on the turbine with  $TIT = 1700$  °C [13].

In the case of the analyzes of gas turbines in a wide range of pressure ratio and TIT a significant mistake is to assume constant internal efficiency value, therefore the paper presents the calculation method of the gas turbine with variable isentropic efficiency of the compressor and the turbine depending on the pressure ratio and TIT.

## 2 Gas turbine model

The gas turbine is modeled using commercial PC-based software application for design and performance evolution of thermal power plant systems,

GateCycle. Figure 2 shows a scheme of the gas turbine. Composition and parameters of ambient air are set according to ISO-2314 ( $t_{0a} = 15^\circ\text{C}$ ,  $p_{0a} = 101.325\text{ kPa}$ ). Assumed fuel is the natural gas composed of: 98.21%  $\text{CH}_4$ , 1.27%  $\text{N}_2$ , and 0.52%  $\text{CO}_2$ , with temperature and pressure at the combustor inlet equal to  $15^\circ\text{C}$  and  $3.5\text{ MPa}$ , respectively. The lower heating value (LHV) of the fuel is equal to  $LHV = 48\,110.54\text{ kJ/kg}$  (according to ISO 6976:1995/1996). Table 1 summarizes the main parameters of the gas turbine installation.

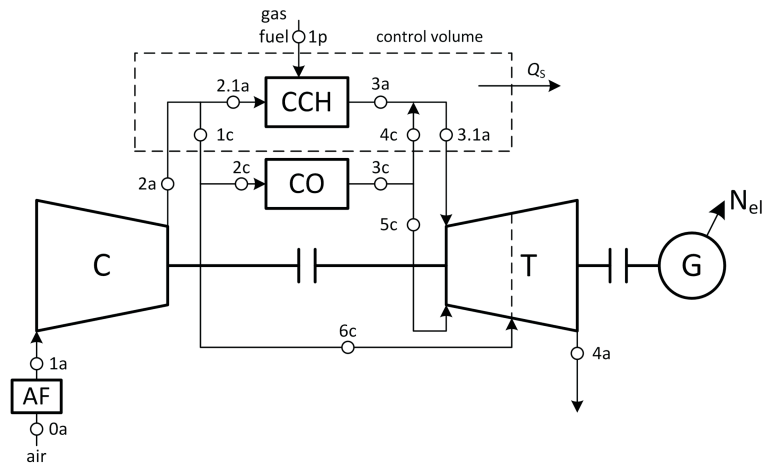


Figure 2: Scheme of the gas turbine: AF – air filter, C – compressor, CO – cooler, CCH – combustion chamber, T – turbine, G – generator,  $Q_s$  – waste heat.

Table 1: The main parameters of the gas turbine installation.

Parameter	Symbol	Value	Unit
Gas turbine electric power	$N_{el\ GT}$	200	MW
Mechanical efficiency	$\eta_m$	99.5	%
Generator efficiency	$\eta_g$	98.5	%
Compressor inlet pressure loss (air filter)	$\xi_{in}$	1	%
Combustion chamber pressure loss	$\xi_{CCH}$	4.5	%
Gas turbine outlet pressure loss	$\xi_{out}$	3.8	%

The turbine cooling air flow is equal to 20% of the compressor inlet flow, from which 12% is cooled to  $200^\circ\text{C}$  (3c) and used for cooling the combustor

(8% in 4c) and the first stage of turbine (4% in 5c), the remaining 8% is used for cooling the following turbine stages (6c).

The gas turbine outlet temperature is maintained at the level of  $t_{4a} = 630^\circ\text{C}$ . Depending on the pressure ratio,  $\beta$ , the COT is adjusted to obtain the desired temperature ( $t_{3a}$ ). Turbine outlet pressure is set at  $p_{4a} = 105.327\text{ kPa}$ , based on the outlet pressure loss

$$p_{4a} = \frac{p_{0a}}{1 - \xi_{out}} \quad (6)$$

Isentropic efficiency of the compressor and the turbine are determined on the basis of polytropic efficiency. Calculation path is presented in the following sections.

### 3 Calculation algorithm of the compressor

The compressor work does not depend on the parameters of the turbine, so in the first place calculations for the air compressor was performed to give the isentropic efficiency graph,  $\eta_{iC}$  as a function  $\beta$ . The calculations are based on the compressor polytropic efficiency graph (Fig. 3), adopted on the basis of [14] for conservative (C) and optimistic (O) scenario.

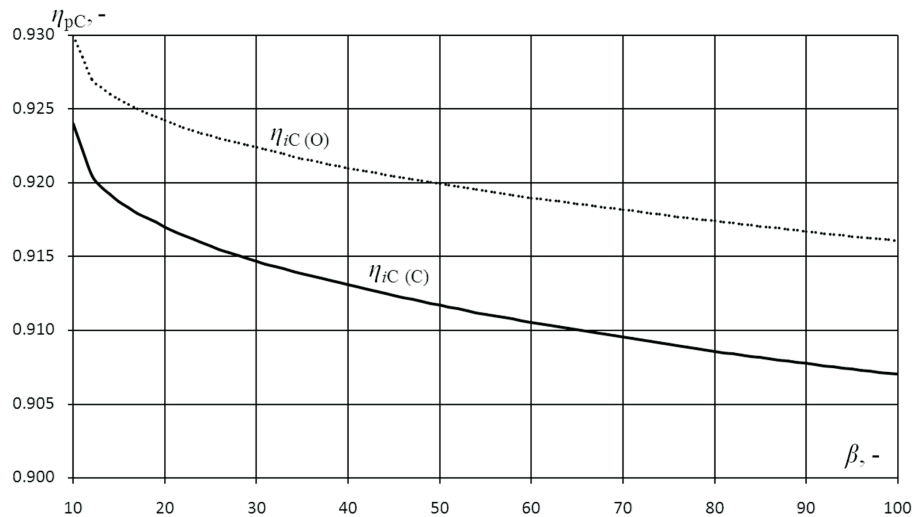


Figure 3: The compressor polytropic efficiency as a function of pressure ratio for conservative (C) and optimistic (O) scenario.

Compressor isentropic efficiency is determined from the relationship described in [15]:

$$\eta_{iC} = \frac{\beta^{\mu_C} - 1}{\beta^{\eta_{pC}} - 1}, \quad (7)$$

where

$$\tilde{\mu}_C = \frac{R}{\tilde{C}_{psC}}, \quad (8)$$

is the average isentropic exponent,  $R$  is the individual gas constant value, and  $\tilde{C}_{psC}$  is the average specific heat for the isentropic conversion, here determined from relation

$$\tilde{C}_{psC} = \frac{\left[ C_{ps}(T_{1a}) \ln\left(\frac{T_{1a}}{T_0}\right) - C_{ps}(T_{2a}) \ln\left(\frac{T_{2a}}{T_0}\right) \right]}{\ln\left(\frac{T_{1a}}{T_{2a}}\right)}, \quad (9)$$

where  $C_{ps}(T)$  is specific heat of air and its values are read for known temperatures ( $T_{1a}$  and  $T_{2a}$ ), gas composition and the reference temperature ( $T_0$ ) from ideal gas parametric tables, e.g. [15,16].

Block diagram of the calculation algorithm for the compressor is presented in Fig. 4. In a first place the compressor polytropic efficiency,  $\eta_{pC}$ , is read from the graph (Fig. 3) for the analyzed pressure ratio,  $\beta$ . Based on the Eqs. (7)–(9) isentropic efficiency of the compressor,  $\eta_{iC}$ , is calculated with initial assumption of  $C_{ps}(T_{1a}) = \tilde{C}_{psC}$ . Then, compressor outlet temperature  $T_{2a}$  and current values of  $\tilde{C}_{psC}$  and  $(\eta_{iC})_t$  are determined. The calculations are completed when the absolute difference between the previous and the current efficiency value is less than a predefined calculation precision,  $\Delta\eta_{\max}$ . Otherwise, the next iterations of compression calculations is performed for current efficiency until the predefined precision is complied.

The resulting characteristics of compressor isentropic efficiency are presented in Fig. 5, while the compressor outlet temperature is shown in Fig. 6. It is assumed that the maximum acceptable compressor outlet temperature is about 600 °C due to design restrictions. This temperature level is reached for pressure ratio  $\beta = 40$ . Thus, to apply a higher  $\beta$  a solution reducing the temperature is needed, e.g., compressor with air intercooling or the use of new materials.

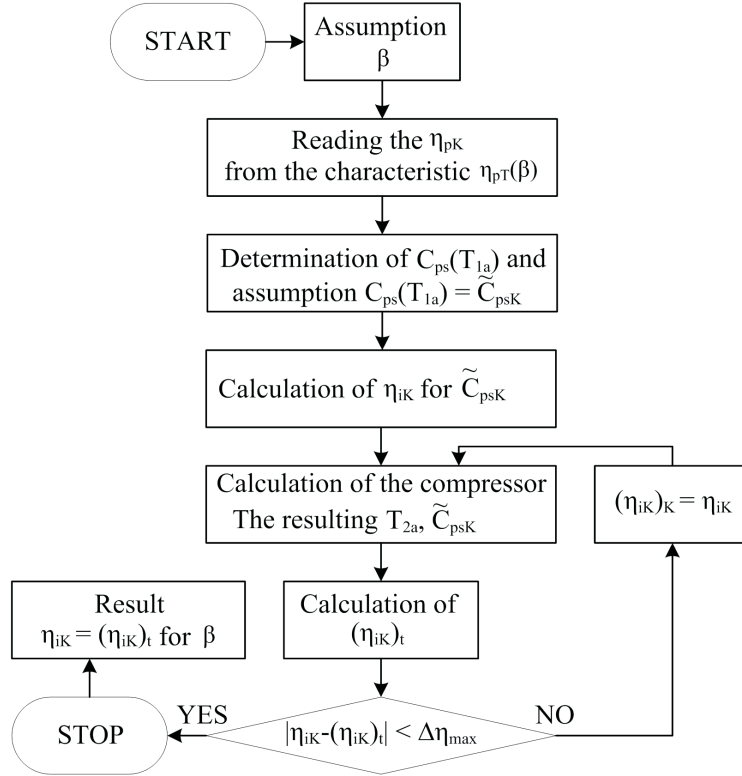


Figure 4: Block diagram of the calculation algorithm for the compressor.

## 4 Calculation algorithm of the turbine

The next step is to calculate the turbine isentropic efficiency,  $\eta_{iT}$ , on the basis of polytropic efficiency characteristics presented in Fig. 7, which depends mainly on the turbine inlet temperature and, in the second place, on the pressure ratio.

The value of  $\beta = 0$  is theoretical, to actual  $\eta_{pT}$  value for assumed  $\beta$  is obtained by adding the corresponding value according to the relation

$$\eta_{pT}(\beta, TIT) = \eta_{pT}(TIT, \beta = 0) + 0.00225 \beta . \quad (10)$$

The turbine inlet temperature is determined according to ISO-2314 standard [15]. It is a theoretical temperature before the first stage stationary blades. Simplification is here assumed that the total turbine cooling flow

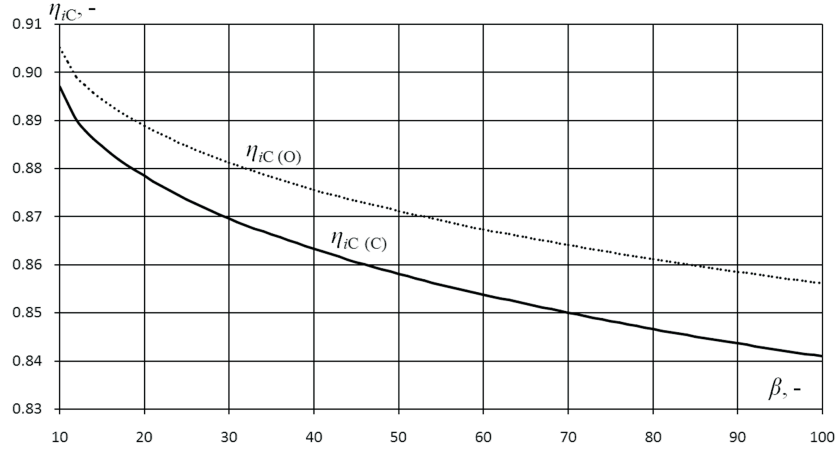


Figure 5: The compressor isentropic efficiency as a function of pressure ratio for conservative (C) and optimistic (O) scenario.

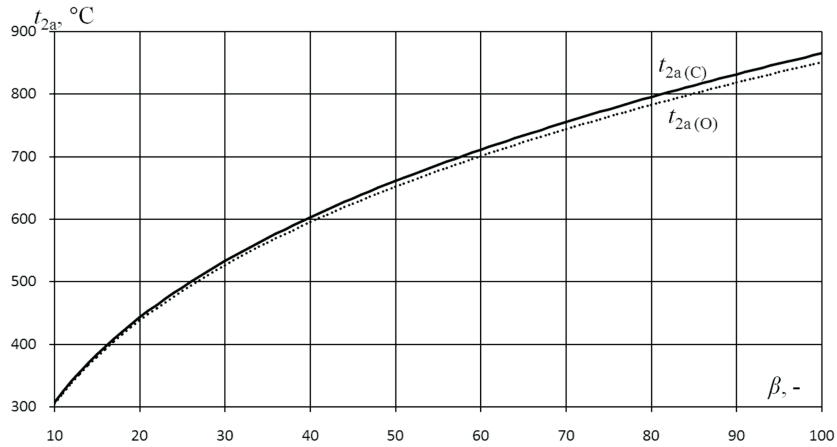


Figure 6: The compressor outlet temperature as a function of pressure ratio for conservative (C) and optimistic (O) scenario.

is mixed with the gas flow from combustor prior to entering the turbine, as illustrated in Fig. 8.

The turbine isentropic efficiency is determined from the relationship, described in detail in [15]

$$\eta_{iT} = \frac{1 - \beta^{-\mu T} \eta_{pT}}{1 - \beta^{-\mu T}}, \quad (11)$$

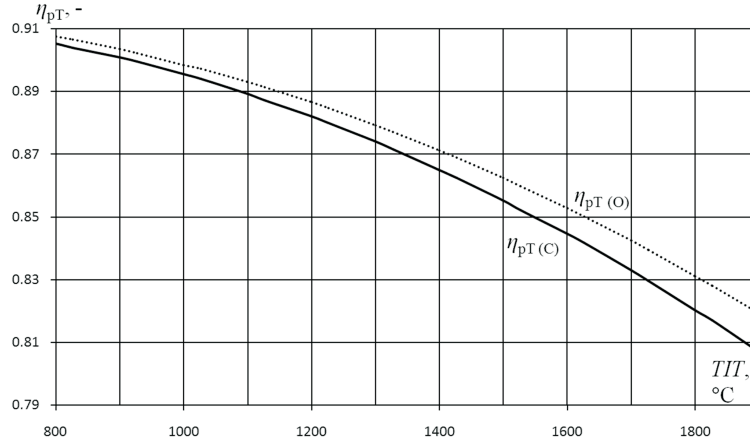


Figure 7: Turbine polytropic efficiency in function of turbine inlet temperature for  $\beta = 0$  for conservative (C) and optimistic (O) scenario.

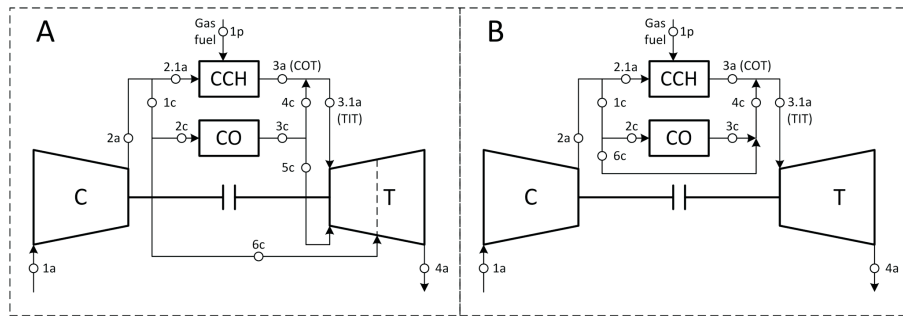


Figure 8: Diagram showing the relationship between the turbine inlet temperature (TIT) and the turbine cooling air: A – the real system, B – the system according to [17].

where

$$\tilde{\mu}_T = \frac{R}{\tilde{C}_{psT}}. \quad (12)$$

The average specific heat for isentropic conversion in turbine,  $\tilde{C}_{psT}$ , is determined similar to (9) from relationship

$$\tilde{C}_{psT} = \frac{[C_{ps}(TIT) \ln\left(\frac{TIT}{T_0}\right) - C_{ps}(T_{4a}) \ln\left(\frac{T_{4a}}{T_0}\right)]}{\ln\left(\frac{TIT}{T_{4a}}\right)}, \quad (13)$$

where  $C_{ps}(T)$  is specific heat of the flue gas with given composition and temperature, read from the ideal gas parametric tables, e.g., in [15,16].

If simplification in accordance with ISO-2314 is not applied, the calculation need to be done for each of the turbine stages resulting from the cooling, separately. This is caused by mixing of the flue gas with the cooling air, which changes the gas composition and temperature affecting its parameters ( $\tilde{C}_{psT}$ ). Calculation of  $\eta_{iT}$  is performed iteratively according to the algorithm illustrated in Fig. 9. For the known compressor parameters

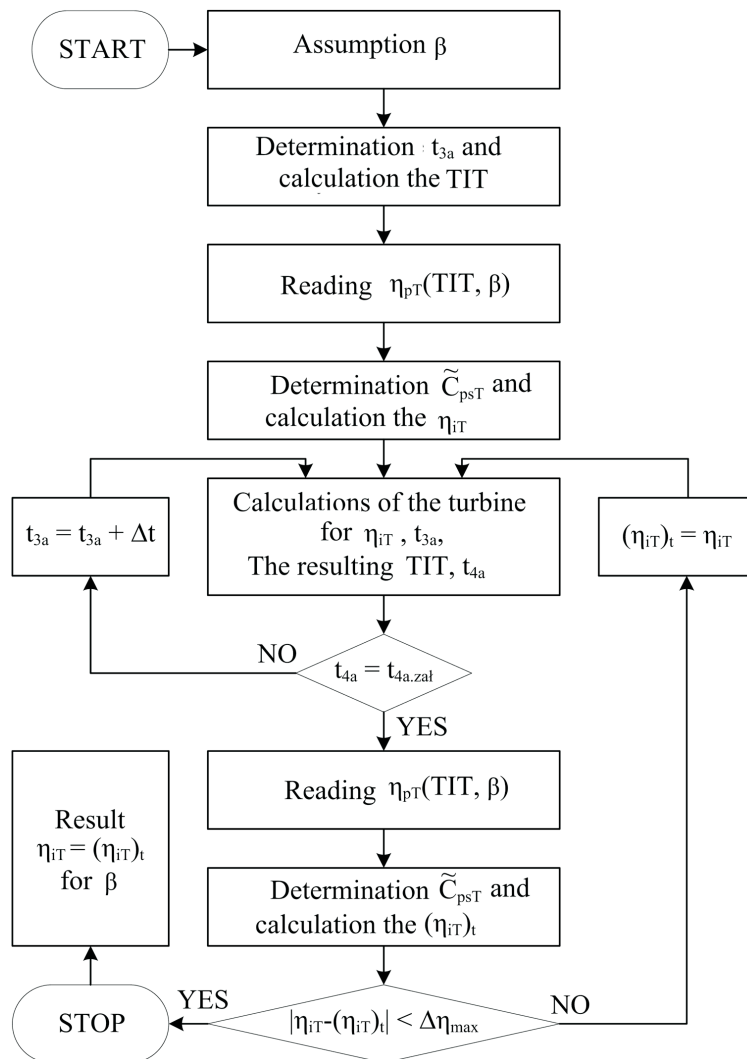


Figure 9: Block diagram of the calculation algorithm for the turbine.

at given  $\beta$  calculations for the turbine can be performed. The objective for the turbine is constant turbine outlet temperature  $(t_{4a})_{est} = 630 \text{ }^\circ\text{C}$ , which means that initially the combustor outlet temperature,  $t_{3a}$ , and the resulting TIT, are unknown. Therefore, at first TIT must be determined on the basis of preassumed  $t_{3a}$ . For given  $\beta$  and initial TIT the turbine polytropic efficiency,  $\eta_{pT}$ , is read and basing on Eqs. (11)–(13) isentropic efficiency,  $\eta_{iT}$ , is calculated. Then, calculations for the turbine are performed and  $(t_{4a})_{est} = t_{4a}$  is not met, the small iteration loop is realized by adjusting  $t_{3a}$ . After the temperature condition is fulfilled, the current values of  $\eta_{pT}$  and  $\eta_{iT}$  are re-determined for obtained results. In analogy to the compressor, turbine calculations are completed when the resulted  $(\eta_{iT})_t$  precision is met.

The obtained turbine isentropic efficiency characteristics are shown in Fig. 10, while the resulted temperatures of combustor outlet and turbine inlet are shown in Fig. 11. The resulting turbine isentropic efficiency can be applied only for the analyzed case, since they depend on TIT,  $T_{4a}$  and flue gas composition. For new assumptions the efficiency must be recalculated according to the presented algorithm (Fig. 9).

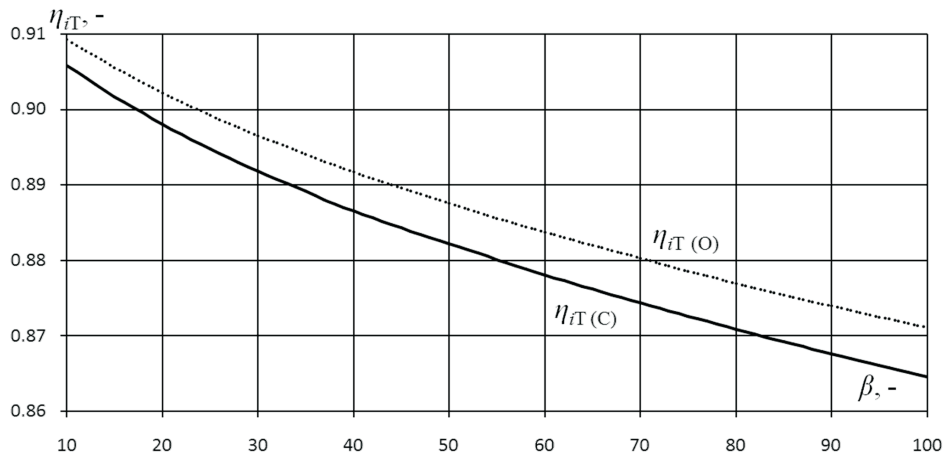


Figure 10: The turbine isentropic efficiency in as a function of pressure ratio as for conservative (C) and optimistic (O) scenario.

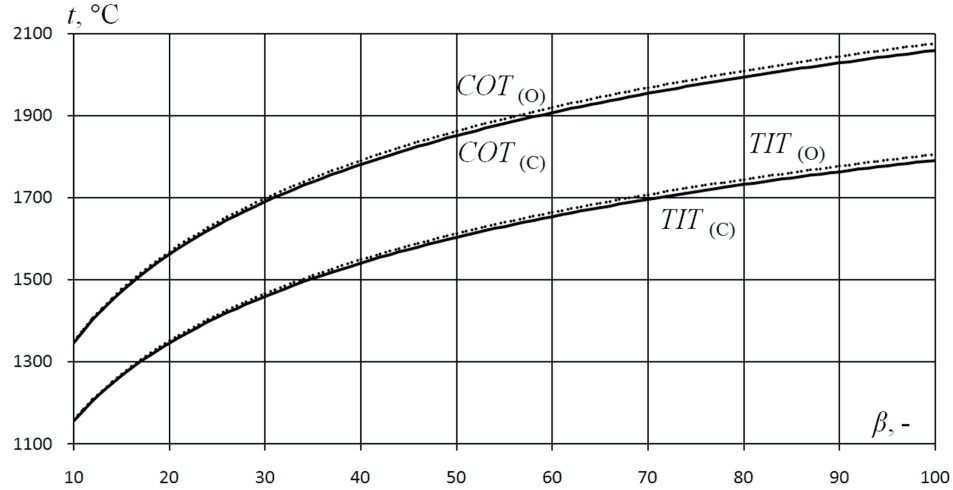


Figure 11: The temperatures of combustor outlet and turbine inlet as a function of pressure ratio for conservative (C) and optimistic (O) scenario.

## 5 Gas turbine efficiency analysis

Gross electric efficiency of the gas turbine,  $\eta_{elGT.gross}$ , is determined using the lower heating value,  $LHV$ , of the fuel, according to relation

$$\eta_{elGT.gross} = \frac{N_{elGT}}{\dot{m}_f LHV}, \quad (14)$$

while the net efficiency takes into account the gas turbine own needs

$$\eta_{elGT.net} = \frac{N_{elGT.gross} - \Delta N_{GT} + N_{FC}}{\dot{m}_f LHV}, \quad (15)$$

where  $\dot{m}_f$  is the mass flowrate of fuel. The gas turbine own needs,  $\Delta N_{GT}$ , are assumed to be 0.22% of the gas turbine electric power,  $\Delta N_{GT}$ , and  $N_{FC}$  is the fuel compressor power. The resulting gross and net electric efficiency of the gas turbine in function of the pressure ratio are shown in Fig. 12. Chosen characteristic parameters of the gas turbine installation for maximum achieved efficiency are summarized in Tab. 2.

## 6 Conclusions

A relatively high cost of the steam turbine installation compared to the gas turbine determines the direction of the combined cycle gas turbine unit

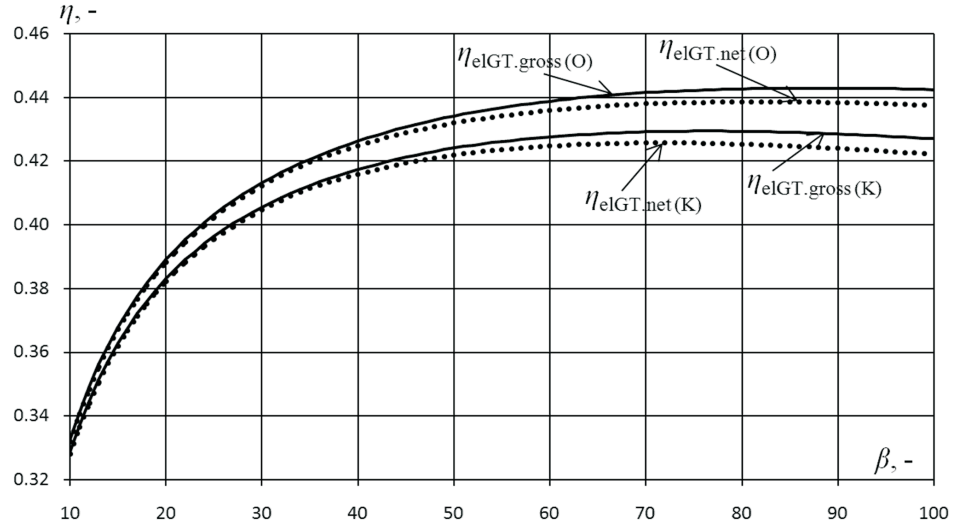


Figure 12: Gross and net efficiency of the gas turbine installation as a function of pressure ratio for conservative (C) and optimistic (O) scenario.

Table 2: Characteristic parameters of the gas turbine installation for chosen  $\beta$ .

Symbol	Unit	Conservative scenario (C)		Optimistic scenario (O)	
Function max.		$\eta_{elGT.gross}$	$\eta_{elGT.net}$	$\eta_{elGT.gross}$	$\eta_{elGT.net}$
$\beta$	–	76	71	87.0	82
$COT$	°C	1979.2	1958.8	2034.7	2016.7
$TIT$	°C	1718.9	1700.5	1768.0	1751.8
$\eta_{iT}$	–	0.8723	0.8740	0.8748	0.8764
$\eta_{iC}$	–	0.8480	0.8497	0.8593	0.8607
$t_{2a}$	°C	779.6	759.3	807.9	790.1
$\eta_{elGT.gross}$	–	0.4294	0.4293	0.4429	0.4428
$\eta_{elGT.net}$	–	0.4256	0.4257	0.4385	0.4386

efficiency increase. Current barrier of net electric efficiency of the CCGT plant amounting 61% can be exceeded in the near future through the increase in the gas turbine efficiency, what can be realized in two ways. The first concept is to use gas turbines with standard pressure ratios (about 20), with a high turbine inlet temperature at the level of 1700 °C (J-class turbines). The condition for success is the use of modern gas turbine cooling

concepts (steam cooling) and the reduction of  $\text{NO}_x$  emission. An alternative solution is the use of higher pressure ratios at the level of 40–50 with lower TIT (about 1500–1550 °C).

The presented calculation algorithms allowed to obtain isentropic efficiency characteristics for the compressor and the turbine depending on the pressure ratio and the turbine inlet temperature.

The analysis revealed that the gas turbine efficiency reaches its optimum at a range of high pressure ratios ( $\beta = 70\text{--}90$ ). However, for such high  $\beta$  the compressor outlet temperature is far beyond 600 °C, temperature limit in the compressor. Thus, the use of such high  $\beta$  would require fundamental modifications in the compressor design, e.g., by using a two-stage compressor with intercooling of the compressed air. The resulting TIT values for the pressure ratios above 40 also exceed the values in modern gas turbines. The use of such high temperatures requires a more efficient cooling of the turbine blades or the use of more durable materials.

The obtained gas turbine electric efficiency characteristics shows that an increase of pressure ratio above 50 is not justified due to the slight increase in the efficiency with a significant growth of compressor outlet and turbine inlet temperatures.

*Received April 2014*

## References

- [1] CHMIELNIAK T.: *Energy Technologies*. WNT, Warsaw 2008 (in Polish).
- [2] SZARGUT J., ZIĘBIK A.: *Fundamentals of Thermal Energy*. PWN, Warsaw 1998 (in Polish).
- [3] KOTOWICZ J.: *Combined Cycle Power Plants*. Wydawnictwo Kaprint, Lublin 2008 (in Polish).
- [4] KOTOWICZ J., BARTELA Ł.: *The thermodynamic and economic optimization of a gas-steam power plant by means of genetic algorithms*. Rynek Energii **75**(2008), 2, 31–38 (in Polish).
- [5] KOTOWICZ J., BARTELA Ł.: *The influence of economic parameters on the optimal values of the design variables of a combined cycle plant*. Energy **35**(2010), 2, 911–919.
- [6] KOTOWICZ J., JOB M.: *Thermodynamic and economic analysis of a gas turbine combined cycle plant with oxy-combustion*. Arch. Thermodyn. **34**(2013), 4, 215–233.
- [7] KOTOWICZ J., BARTELA Ł.: *Analysis of operation of the gas turbine in a poligeneration combined cycle*. Arch. Thermodyn. **34**(2013), 4, 137–159.

- [8] *Heavy Duty Gas Turbines & Combined Cycle*. General Electric. [http://site.ge-energy.com/prod\\_serv/products/gas\\_turbines\\_cc/en/index.htm](http://site.ge-energy.com/prod_serv/products/gas_turbines_cc/en/index.htm) (accessed on 15.04.2014).
- [9] *Gas turbines*. Mitsubishi Heavy Industries, Ltd. [http://www.mhi.co.jp/en/products/category/gas\\_turbin.html](http://www.mhi.co.jp/en/products/category/gas_turbin.html) (accessed on 15.04.2014).
- [10] FACCHINI B., INNOCENTI L., CARVNEVALE E.: *Evaluation and comparison of different blade cooling solutions to improve cooling efficiency and gas turbine performances*. In: Proc. ASME Turbo Expo 2001, 2001-GT-0571, June 2001, New Orleans.
- [11] JORDAL K. *et al.*: *New possibilities for combined cycles through advanced steam technology*. In: Proc. ASME Turbo Expo 2002, GT-2002-30151, June 2002, Amsterdam, The Netherlands.
- [12] HADA S., YURI M., MASADA J., ITO E., TSUKAGOSHI K.: *Evolution and future trend of large frame gas turbines a new 1600 degree C, J class gas turbine*. In: Proc. ASME Expo 2012, GT2012-68574, June 11–15, 2012, Copenhagen.
- [13] ITO E., OKADA I., TSUKAGOSHI K., MUYAMA A., MASADA J.: *Development of key Technologies for next generation gas turbine*. In: Proc. ASME Turbo Expo 2007: Gas Turbine Technical Congress and Exposition, GT2007-41023, May 17–20, 2007, Montreal.
- [14] WETTSTEIN H.E.: *The potential of GT combined cycles for ultra high efficiency*. In: Proc. ASME Turbo Expo 2012, GT2012-68586. Denmark, 2012.
- [15] CHMIELNIAK T., RUSIN A., CZWIERTNIA K.: *Gas Turbines*. Ossolineum, Wrocław 2001 (in Polish).
- [16] SZARGUT J.: *Thermodynamics*. PWN, Warsaw 2000 (in Polish).
- [17] ISO 2314:2009 Standard: *Gas turbines – Acceptance tests*.



archives  
of thermodynamics

Vol. 37(2016), No. 4, 37–53

DOI: 10.1515/aoter-2016-0026

## Combined use of coal mine gases for efficient energy generation

STEFAN POSTRZEDNIK\*

Silesian University of Technology, Institute of Thermal Engineering,  
Konarskiego 18, 44-100 Gliwice, Poland

**Abstract** There are two basic types of coal mine gases: gas from demethanation of coal deposits, and ventilation gas; containing combustible ingredients (mainly methane,  $\text{CH}_4$ ). Effective use of these gases is an important technical and ecological issue (greenhouse gas emissions), mainly due to the presence of methane in these gases. Serious difficulties in this area (e.g. using them as the fuel for internal combustion (IC) engine) occur mainly in relation to the ventilation gas, whereas the gas from demethanation of coal deposits can be used directly as the fuel for internal combustion engines. The proposed solution of this problem shows that the simple mixing of these two gases (without supplying of oxygen from ambient air) is the effective way to producing the gaseous combustible mixture, which can be used for the fueling of internal combustion gas engines. To evaluate the energy usefulness of this way produced combustible mixture the process indicator has been proposed, which expresses the share of the chemical energy supplied with the ventilation gas, in the whole chemical energy of the produced fuel combustible mixture. It was also established how (e.g., by appropriate choice of the mixed gas streams) can be achieved significantly higher values of the characteristic process indicator, while retaining full energy usefulness of the gained gaseous mixture to power combustion engines.

**Keywords:** Mine firedamp gases; Preparing of flammable mixture; Fuelling of IC engines

---

\*Corresponding Author. E-mail: stefan.postrzednik@polsl.pl

## 1 Introduction – general characteristics of the issue

In areas belonging to coal mines remain at the disposal two main process gases (containing combustible ingredients – mainly methane,  $\text{CH}_4$ ; next other components: nitrogen,  $\text{N}_2$ , and oxygen,  $\text{O}_2$ , in proportion as in the air [1–3]):

- gas from demethanation of coal deposits (with the methane content about  $\text{CH}_{4,p} \approx 50\%$ , at dry gas state, which often constitutes a serious fire hazard in the mine),
- ventilation gas (methane content  $\text{CH}_{4,w} \leq 1.0\%$ , at dry gas state, most commonly lead out through ventilation shafts into the environment).

Effective and reasonable use of these gases is an important technical and ecological issue (greenhouse gas emissions), mainly due to the presence of methane in these gases [4,5]. Serious difficulties in this area (e.g. using them as the fuel for internal combustion (IC) engine) occur mainly in relation to the ventilation gas, whereas the gas from demethanation of coal deposits can be used directly as the fuel for IC engines [6–8].

By analyzing the chemical composition of the mine gases in terms of the basic stoichiometric conditions of the combustion process – it can be stated, that in the typical ventilation gas the amount of oxidant (air, oxygen  $\text{O}_2$ ) is present in large excess (or deficient of appropriate combustible components, mainly methane in relation to stoichiometric needs. A different situation is characterized by utilization of the gas from demethanation of coal deposits; the main combustible component methane occurs in relative stoichiometric excess, which means that for the full and complete combustion of this gas an additional amount of oxidant (air, oxygen  $\text{O}_2$ ) should be supplied into the combustion chamber [2,9]. In view of the above it was noted, that it is possible to prepare the good gas combustible mixture (mainly in the aspect of the appropriate oxygen excess ratio,  $\lambda$  [7,8]) – by adequate mixing of the ventilation gas stream with the gas stream from demethanation of coal deposits.

The analysis presented in the paper refers to desirability of the implementation of a properly organized mixing process of the gas stream from demethanation of coal deposits with the adequate stream of the ventilation gas; and of course all without downloading additional air (oxygen  $\text{O}_2$ ) from

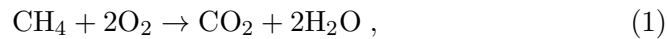
the environment.

For assessment of the energy usefulness of the specific produced gas fuel mixture special process indicator,  $\Omega$ , is defined, which value expresses the share of the chemical energy supplied with the ventilation gas,  $E_{ch,w}$ , in the whole chemical energy,  $E_{ch,m}$  of the produced gas fuel combustible mixture. An complex analysis of the values thus defined process indicator was done, and on this way successfully confirmed its practical usefulness in the complex investigation of the whole issue.

## 2 Basic stoichiometric conditions for the flammable gas mixture

Any portion of the mine gas (ventilation, as well as demethanation gas) may be treated in general as a mixture of the methane,  $\text{CH}_4$ , and air (main components: oxygen,  $\text{O}_2$ , and nitrogen,  $\text{N}_2$ ).

The combustion of the main combustible component (methane of the mine gas takes place according to the scheme



which means that the specific minimum oxygen demand for the methane is

$$n_{ox,\min} = 2 \text{ kmol}_{\text{O}_2} / \text{kmol}_{\text{CH}_4} , \quad (2)$$

while the specific minimum demand of the air, respectively

$$n'_{a,\min} = 2/0.21 \text{ kmol}_{\text{air}} / \text{kmol}_{\text{CH}_4} = 9.524 \text{ kmol}_{\text{air}} / \text{kmol}_{\text{CH}_4} . \quad (3)$$

The real combustion process takes place at a certain excess of the air (so also the oxygen  $\text{O}_2$ ), which is expressed by the air excess ratio  $\lambda \geq 1$  [6,7]. Therefore, the actual specific amount of air supplied is

$$n'_a = \lambda n'_{a,\min}, \text{ so also the oxygen } n'_{ox} = \lambda n_{ox,\min} . \quad (4)$$

The real content of the methane in the prepared flammable gas mixture equals

$$z_M = \frac{1}{(1 + \lambda n'_{a,\min})} , \quad (5)$$

and because  $n'_{a,\min} = 9,524 \text{ kmol}_{\text{air}} / \text{kmol}_{\text{CH}_4}$  can be rewritten as

$$z_M = \frac{1}{(1 + 9.524 \lambda)} . \quad (6)$$

Interdependence of stoichiometric parameters ( $z_M$ ,  $\lambda \geq 1$ ) conditioning the correctness of the combustion process, and resulting directly from formulas (5) and (6) are illustrated in Fig. 1.

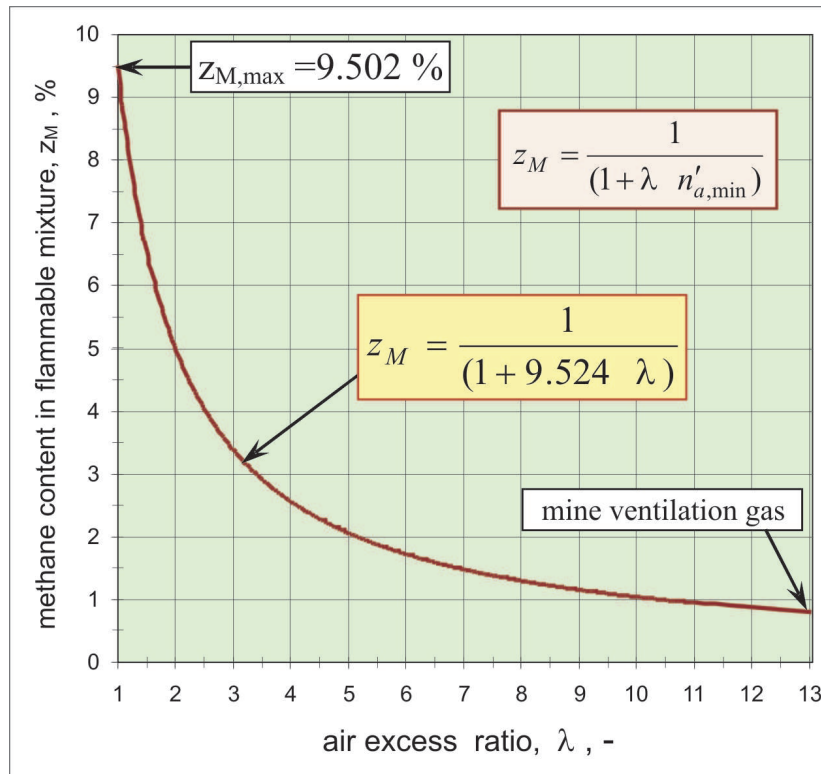


Figure 1: Stoichiometric parameters of the methane combustion mixture.

The maximum value of the methane content in the flammable mixture,  $z_{M,\max}$ , is obtained for  $\lambda = 1$ , and next after using Eq. (6) the standard value is obtained:  $z_{M,\max} = z_{M,\lambda=1} = 9.502\%$ . From this follows a significant limitation  $z_M \leq z_{M,\max}$ , whereby the maximum value  $z_{M,\max}$  is obtained for the so-called stoichiometric mixture (at the value:  $\lambda = 1$ ).

The above observation indicates that the methane content,  $z_M$ , in real, good prepared (in the aspect of the oxygen excess ratio,  $\lambda$ ) flammable mixtures does not exceed the predetermined value  $z_{M,\max} = 9.502\%$ , because otherwise the combustion would be deficient (the presence of carbon monoxide, CO, in the exhaust gas), and even incomplete (the soot appears in combustion products).

The gas air-methane mixture with a slightly higher content of methane  $\text{CH}_4$ , it means at  $z_M > z_{M,\max}$  can also be ignited (it is also usually a serious mine explosion hazard); however, a combustible mixture by more than stoichiometric participation of methane should not be directly used [7,8] for fueling of different energy plants (e.g., boilers, gas turbines, internal combustion engines).

### 3 Preparation and use of the mine gas combustible mixture

Basic mine gases differ in chemical composition (especially in the methane content), so consequently in the calorific value and its energy usefulness [7]. The typical ranges of the methane content are [6,9]:  $z_{M,w} = 0.5\text{--}1.2\%$  – in the ventilation gas;  $z_{M,p} = 40\text{--}60\%$  – gas from demethanation of coal deposits. As average values (typical for the Silesian Mining Region, in Poland) used next for presented exemplary calculations are taken:  $z_{M,w} = 0.8\%$  and  $z_{M,p} = 50\%$ .

By analyzing the chemical composition of the mine gases in terms of the basic stoichiometric conditions of the combustion process it can be stated, that in the case of typical ventilation gas the amount of oxidant (air, oxygen) is present in large excess (or deficient of combustible component, methane) in relation to stoichiometric needs. Meanwhile by utilization of the gas from demethanation of coal deposits the main combustible component methane occurs in relative excess (because usually the methane content  $z_{M,p} > z_{M,\max}$ ), which means that for the full and complete combustion of this gas an additional specific amount of oxidant (air, oxygen) should be supplied into the combustion chamber. Therefore should be noted, that it is possible to prepare the good gas combustible mixture (mainly in the aspect of the oxygen excess ratio  $\lambda \geq 1$ ), by adequate mixing of the ventilation gas stream with the gas stream from demethanation of coal deposits; and of course all without downloading additional air (oxygen) from the environment.

The base system for preparing of the flammable mixture using the gas stream from demethanation of coal deposits and adequate stream of the ventilation gas is shown in Fig. 2.

Combustible mixture prepared on this way (by mixing of the ventilation gas with the gas from demethanation of coal deposits) can be next effectively used for fueling of the combustion engines.

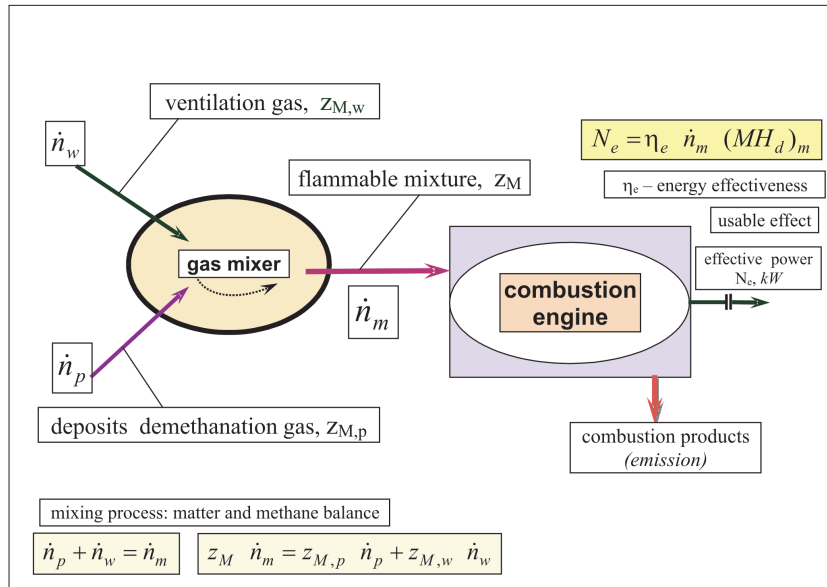


Figure 2: Preparing of the mine gas combustibile mixture with fueling of IC engine.

Internal combustion engines (both spark and compression ignition) are fuelled mostly with classic liquid fuels (petrol – for spark ignition (SI), diesel oil – for compression ignition (CI)) [3,7]. The classic system of the spark ignition combustion engine is presented in the Fig. 3. In case of spark ignition engines, in which the ignition of the earlier prepared vaporised fuel-air mixture is realised by the spark energy source, the liquid fuel (petrol) can be totally replaced by the gas fuels practically without additional troubles. This possibility is essentially restricted in case of compression ignition engines, because ignitability of the gaseous fuels is mostly not so good as ignitability of the diesel oil.

Self-ignition of the gas fuels appears only at considerable higher temperatures in comparison to self-ignition of classical diesel oil. Adequate solution, if this problem can be practically achieved by using of the dual fuelling system is illustrated in Fig. 4.

The diesel engine will be basically filled out with the gas fuel, but for ignition of the prepared fuel gas-air mixture a specified, minimal amount of the liquid fuel (diesel oil) should be at first additionally injected into the combustion chamber [7,8].

The lower heating value of the pure methane equals  $(MH_d)_M = 802.32$

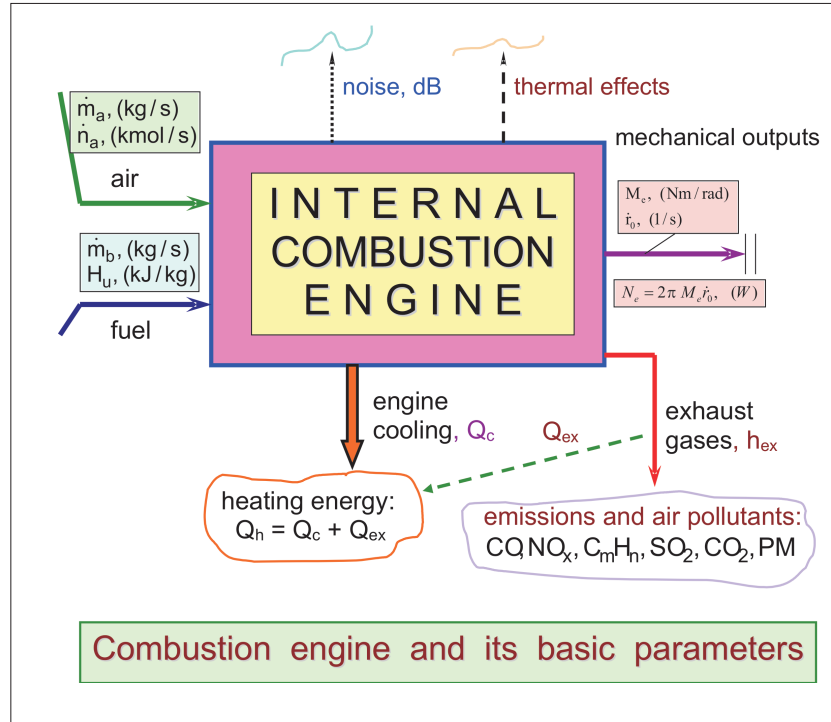


Figure 3: Classic system of the spark ignition (SI) combustion engine.

MJ/kmol<sub>CH<sub>4</sub></sub>, and therefore adequate  $(MH_d)_w \approx 8.826$  MJ/kmol<sub>gas</sub>  $\approx 394.02$  kJ/m<sub>n</sub><sup>3</sup> for the ventilation gas, and for the gas from demethanation of coal deposits:  $(MH_d)_p \approx 381.10$  MJ/kmol<sub>gas</sub>  $\approx 17013.39$  kJ/m<sub>n</sub><sup>3</sup>.

As regards to the methane stoichiometric mixture ( $\lambda = 1$ ), for which the value of methane content  $z_M = z_{M,max} = 9.502\%$ , its caloric value equals  $(MH_d)_{mix,\lambda=1} = 76.24$  MJ/kmol  $\approx 3403.41$  kJ/m<sub>nmix</sub><sup>3</sup>.

This specific indicator is particularly relevant to the possibility and the efficiency use of this fuel for effective powering [8] of IC engines.

#### 4 Basic dependences and balance relations

The basic stream of the produced flammable mixture  $\dot{n}_m$  is the sum of two basic gas streams ( $\dot{n}_p$ ,  $\dot{n}_w$ ) flowing into the system, (Fig. 2)

$$\dot{n}_m = \dot{n}_p + \dot{n}_w. \quad (7)$$

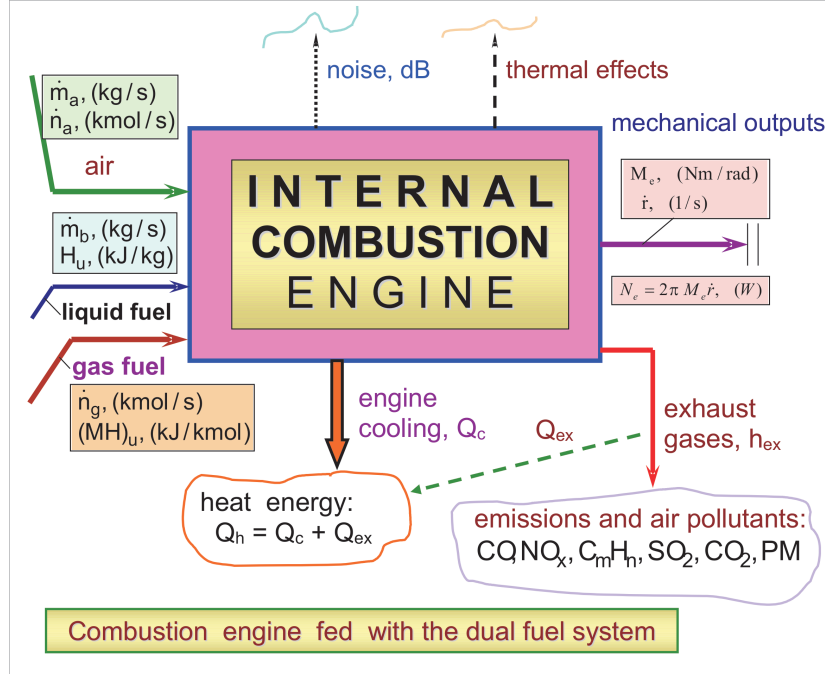


Figure 4: Compression ignition (CI) combustion engine with a dual fuel supply system.

The substance balance of the methane for the mixing process obtains the relationship

$$z_{M,p} \dot{n}_p + z_{M,w} \dot{n}_w = z_{M,m} \dot{n}_m, \quad (8)$$

where:  $z_{M,m}$ , – content of the methane in the produced flammable mixture,  $z_{M,w}$ , – methane content in the ventilation gas,  $z_{M,p}$ , – content of the methane in the gas from demethanation of coal deposits.

Connecting the balance relations (7) and (8) the content of the methane in the produced combustible mixture takes the form

$$z_{M,m} = \frac{1}{\dot{n}_p + \dot{n}_w} (z_{M,p} \dot{n}_p + z_{M,w} \dot{n}_w), \quad (9)$$

and finally

$$z_{M,m} = \frac{1}{1 + \left(\frac{\dot{n}_p}{\dot{n}_w}\right)} \left[ z_{M,w} + z_{M,p} \left(\frac{\dot{n}_p}{\dot{n}_w}\right) \right] \quad (10)$$

From relation (10) can be concluded, that by increase of the relative amount of the gas from demethanation of coal deposits  $(\dot{n}_p/\dot{n}_w) \uparrow$ , increases the

share of the methane  $z_M \uparrow$  in the flammable mixture, up to the limit value  $z_{M,max} = z_{M,\lambda=1} \approx 9.502\%$ . This relation is illustrated in Fig. 5.

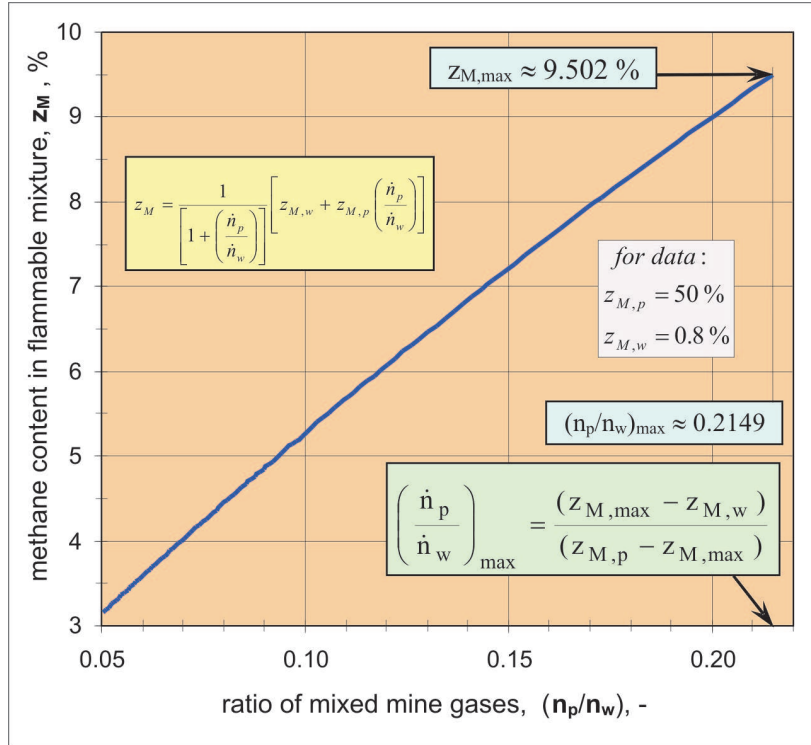


Figure 5: Influence of mine gases relative amount on the methane share in the combustion mixture.

The limitation (6) should be taken into account, which together with relation (10) enables to determine the maximum value of the relative mine gas amount

$$\left(\frac{\dot{n}_p}{\dot{n}_w}\right)_{\max} = \frac{z_{M,\max} - z_{M,w}}{z_{M,p} - z_{M,\max}}, \quad (11)$$

whereby the value  $z_{M,\max} = z_{M,\lambda=1} \approx 9.502\%$ , whence it follows also  $(n_p/n_w)_{\max} \approx 0.2149$ .

Connecting Eqs. (5) and (11) following relationship is obtained

$$\lambda = \frac{[(1 - z_{M,w}) + (1 - z_{M,p}) \left(\frac{\dot{n}_p}{\dot{n}_w}\right)]}{n'_{a,\min} [z_{M,w} + z_{M,p} \left(\frac{\dot{n}_p}{\dot{n}_w}\right)]}, \quad (12)$$

which allows to determine the actual value of the air excess ratio ( $\lambda \geq 1$ ); whereby parameter used  $n'_{a,min} \approx 9.524 \text{ kmol}_{air}/\text{kmol}_{CH_4}$ , and the another typical values of representative characteristic parameters can be taken as  $z_{M,w} = 0.8\%$  and  $z_{M,p} = 50.0\%$ .

In order to achieve the assumed value of the air (oxygen) excess ratio  $\lambda \geq 1$  should be, using Eq. (12), respectively, choose the quotient of mine gas streams as

$$\left(\frac{\dot{n}_p}{\dot{n}_w}\right) = \frac{1 - z_{M,w}(1 + \lambda n'_{a,min})}{z_{M,p}(1 + \lambda n'_{a,min}) - 1}, \quad \lambda \geq 1, \quad (13)$$

while limiting  $(\dot{n}_p/\dot{n}_w) \leq (\dot{n}_p/\dot{n}_w)_{max}$  resulting from Eq. (11).

Basing on Eq. (13) the influence of the assumed value of the air excess ratio  $\lambda \geq 1$ , on the value of the analyzed relative mine gas streams  $(\dot{n}_p/\dot{n}_w) \leq (\dot{n}_p/\dot{n}_w)_{max}$  is depicted in Fig. 6.

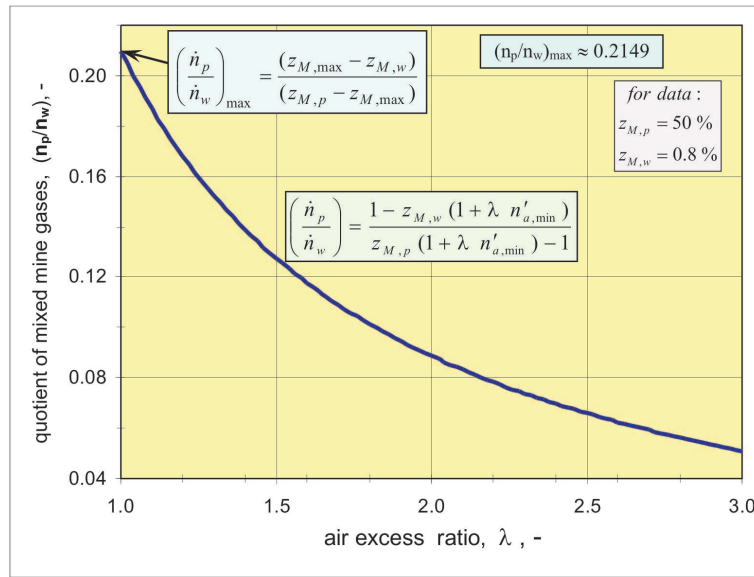


Figure 6: Influence of the air excess ratio on the relative amount of mixed mine gases.

Taking into account the stoichiometric state of the air excess ratio  $\lambda = 1$ , the maximum value of the demethanation gas relative amount results directly from Eq. (13)

$$\left(\frac{\dot{n}_p}{\dot{n}_w}\right)_{max} = \frac{1 - z_{M,w}(1 + n'_{a,min})}{z_{M,p}(1 + n'_{a,min}) - 1}, \quad (14)$$

which dependence directly corresponds with relation (11).

The air excess ratio ( $\lambda_{\max} \geq \lambda \geq 1$ ) reaches the maximum value at the zero value of the ratio ( $\dot{n}_p/\dot{n}_w \rightarrow 0$ ), and then

$$\lambda_{\max} = \frac{(1 - z_{M,w})}{n'_{a,\min} z_{M,w}}. \quad (15)$$

whereby  $n'_{a,\min} \approx 9.524 \text{ kmol}_{air}/\text{kmol}_{CH_4}$ , and for the value  $z_{M,w} = 0.8\%$   $\lambda_{\max} = 13.02$  is obtained.

Often also (at  $z_{M,w} = 0.8\%$ ) may appear that the produced gas fuel mixture is outside the flammability. Although allowing higher content of the methane in the ventilation gas (Fig. 1), e.g., for  $Z_{M,w} \approx 2\%$  the maximum of the air (oxygen) excess ratio reaches value about  $\lambda_{\max} = 5.145$ , and it means that in this case the prepared mine gases mixture will burn in principle without any problems.

## 5 Energy usefulness of formed mine gases mixture

The main quantity determining the energy usefulness of the mine gases prepared mixture is its lower heating value  $(MH_d)_m$ , which depends basically from the actual methane content,  $z_M$ , resulting directly from Eq. (10), because

$$(MH_d)_m = z_M (MH_d)_M, \quad z_M \leq z_{M,\max} \approx 9.502\%, \quad (16)$$

where:  $(MH_d)_M = 802.32 \text{ MJ/kmol}$  – lower heating value of the pure methane.

After substituting dependence (10) in relation (16) is achieved

$$(MH_d)_m = \frac{(MH_d)_M}{1 + \left(\frac{\dot{n}_p}{\dot{n}_w}\right)} \left[ z_{M,w} + z_{M,p} \left(\frac{\dot{n}_p}{\dot{n}_w}\right) \right], \quad (17)$$

and next the maximum value equals

$$(MH_d)_{m,\max} = z_{M,\max} (MH_d)_M, \quad (18)$$

since  $z_{M,\max} \approx 9.502\%$  therefore finally  $(MH_d)_{m,\max} = 0.09502 \times 802.32 = 76.24 \text{ MJ/kmol}$ .

The quotient of the mixed mine gases ( $\dot{n}_p/\dot{n}_w$ ) is limited:  $(\dot{n}_p/\dot{n}_w) \leq (\dot{n}_p/\dot{n}_w)_{\max}$ , which recognizes from formula (14), and therefore principally

indicates the maximum value of the relative amounts of the gas from demethanation of coal deposits.

Finally the relative value of the lower heating value,  $(MH_d)_m$ , of the formed mine gas mixture in relation to lower heating value,  $(MH_d)_M$ , of pure methane presents the formula

$$\frac{(MH_d)_m}{(MH_d)_M} = \frac{1}{\left[1 + \left(\frac{\dot{n}_p}{\dot{n}_w}\right)\right]} \left[ z_{M,w} + z_{M,p} \left(\frac{\dot{n}_p}{\dot{n}_w}\right) \right], \quad (19)$$

which informs, that the analyzed relative lower heating value  $(MH_d)_m / (MH_d)_M$  grows with increase of the technology gases quotient  $(\dot{n}_p / \dot{n}_w)$ . This dependence, resulting from Eq. (17), is illustrated in Fig. 7.

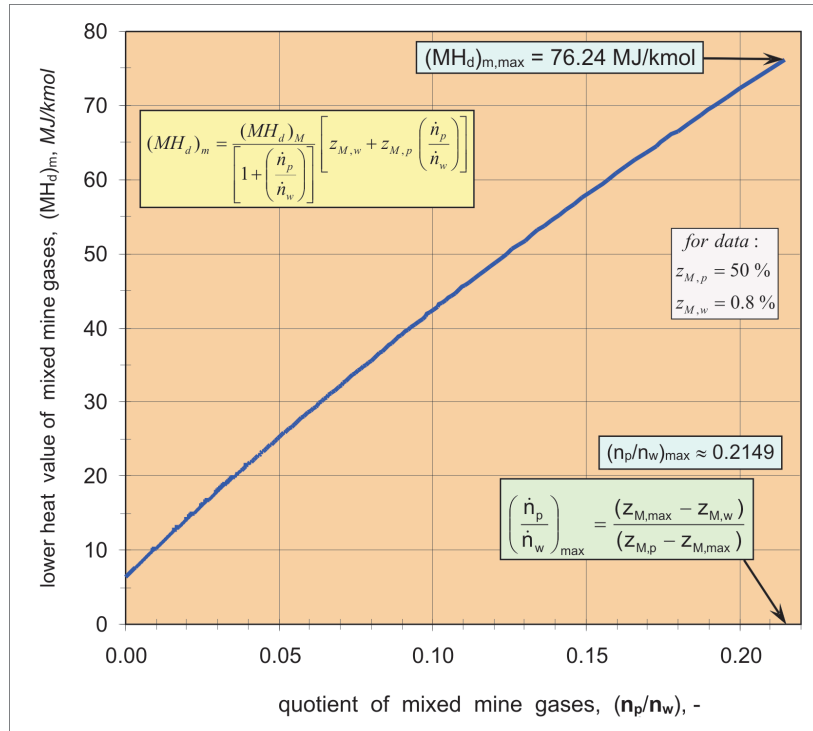


Figure 7: Influence of mine gases relative amount on the lower heat value  $(MH_d)_m$  of flammable mixture.

Bearing in mind the objective of application it should consider how does the share of chemical energy supplied with ventilation gas,  $E_{ch,w}$ , in the

entirely stream of chemical energy,  $E_{ch,m}$ , of produced combustion mixture; this expresses the process indicator defined as

$$\Omega \stackrel{df}{=} \frac{\dot{E}_{ch,w}}{\dot{E}_{ch,m}} = \left( \frac{z_{M,w}}{z_{M,m}} \right) \left( \frac{\dot{n}_w}{\dot{n}_m} \right). \quad (20)$$

The quotient of gas flows equals:

$$\frac{\dot{n}_w}{\dot{n}_m} = \frac{1}{1 + \left( \frac{\dot{n}_p}{\dot{n}_w} \right)}, \quad (21)$$

then according to definition (20) the process indicator results

$$\Omega = \frac{z_{M,w}}{z_{M,m}} \frac{1}{1 + \left( \frac{\dot{n}_p}{\dot{n}_w} \right)}. \quad (22)$$

In turn, after inserting Eq. (10) into (22) is obtained

$$\Omega = \frac{z_{M,w}}{z_{M,w} + z_{M,p} \left( \frac{\dot{n}_p}{\dot{n}_w} \right)}. \quad (23)$$

Influence of the relative amounts of mixed gases,  $(\dot{n}_p/\dot{n}_w)$ , on the achieved values of characteristic process indicator is illustrated in Fig. 8.

The process indicator minimal value,  $\Omega_{min}$ , is to be achieved at the air excess ratio  $\lambda = 1$ ; it can be deduced due to relation (14), so after taking into account Eqs. (14) and (23) is obtained

$$\Omega_{min} = \frac{z_{M,w}}{z_{M,w} + z_{M,p} \left[ \frac{1 - z_{M,w} (1 + n'_{a,min})}{z_{M,p} (1 + n'_{a,min}) - 1} \right]}, \quad (24)$$

where:  $n'_{a,min} \approx 9.524 \text{ kmol}_{air}/\text{kmol}_{CH_4}$ .

For the values  $z_{M,w} = 0.8\%$  and  $z_{M,p} = 50.0\%$  is obtained the basic minimal value  $\Omega_{min} = 6.9304\%$ . The values of the process indicator systematically increase ( $\Omega > \Omega_{min} \approx 6.9304\%$ ) with the dropping the quotient of mixed mine gases amount  $(\dot{n}_p/\dot{n}_w) < (\dot{n}_p/\dot{n}_w)_{max}$ , what should be emphasized in terms of the energy utilization efficiency of the mine gases used.

In the general case, using relation (13), according to which

$$\left( \frac{\dot{n}_p}{\dot{n}_w} \right) = \frac{1 - z_{M,w} (1 + \lambda n'_{a,min})}{z_{M,p} (1 + \lambda n'_{a,min}) - 1} \quad \text{at} \quad \lambda \geq 1 \quad (25)$$

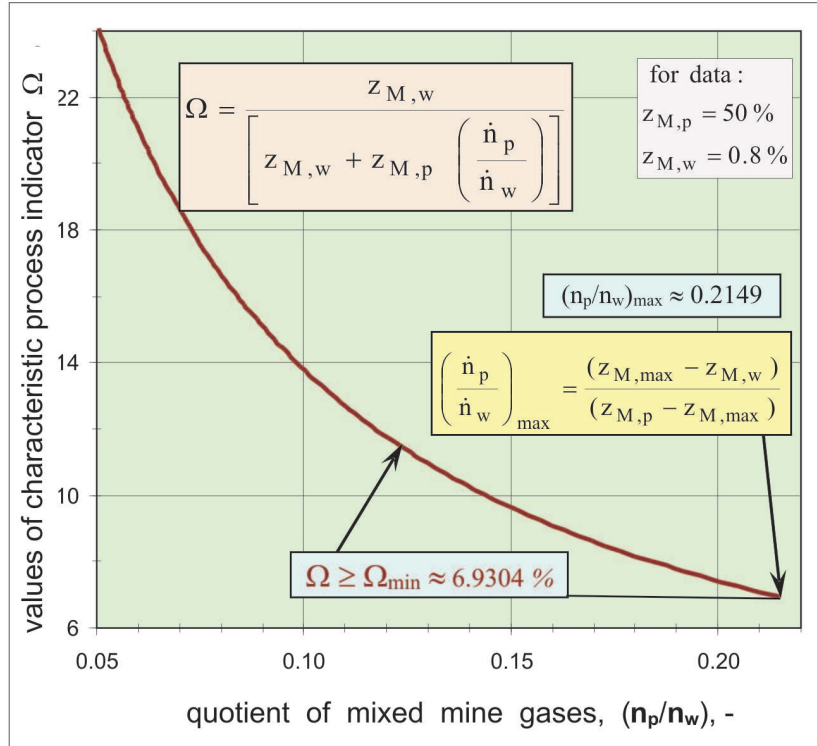


Figure 8: Influence of the mixed gases relative amount on the values of process indicator.

the analyzed dependence (23) takes the form

$$\Omega = \frac{z_{M,w}}{z_{M,w} + z_{M,p} \frac{1 - z_{M,w} (1 + \lambda n'_{a,\min})}{z_{M,p} (1 + \lambda n'_{a,\min}) - 1}}, \quad (26)$$

with which is possible to analyze the effect of the air (oxygen) excess ratio  $\lambda \geq 1$  on the values of the process indicator. The achieved solution of the analyzed problem is illustrated in the Fig. 9.

With the increase of the air excess ratio (at  $\lambda > 1$ ) simultaneously grows the process indicator ( $\Omega > \Omega_{\min} \approx 6.9304\%$ ), and it is worth emphasizing in terms of the system energy utilization efficiency.

Results of the several experimental investigations [7,8] confirm that for powering of the internal combustion gas engines is preferable to use the so-called over-stoichiometric flammable mixtures, i.e., those which are characterized by a slightly higher values ( $1.5 > \lambda > 1.0$ ) of the air (oxygen)

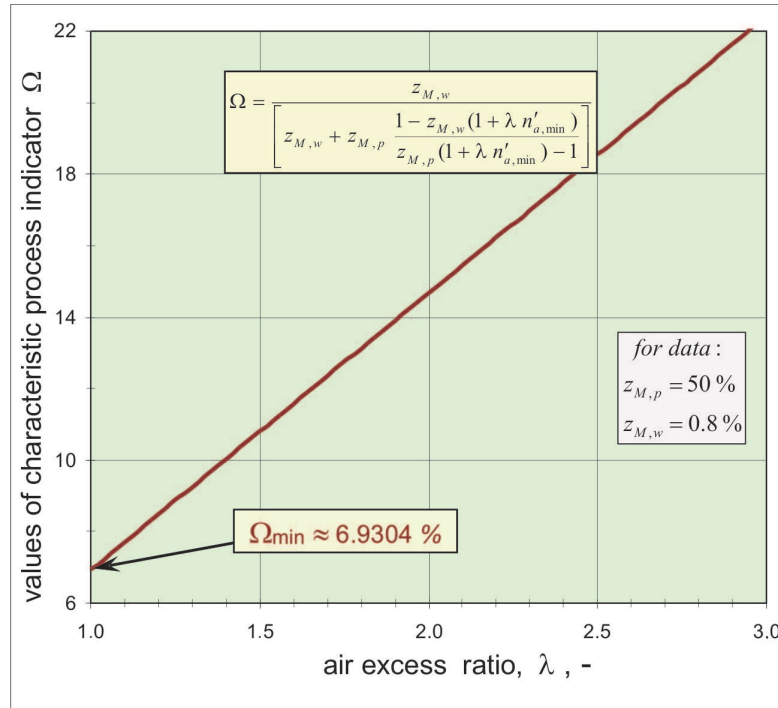


Figure 9: Influence of the air (oxygen) excess ratio on the values of process indicator.

excess ratio. This procedure, by applying the over-stoichiometric air excess ( $1.5 > \lambda > 1.0$ ) allows for achieving of higher values of effective energy efficiency of the internal combustion gas engine. In this situation appears also the possibility of achieving much higher values of the efficiency process indicator, which determines the chemical energy supplied with ventilation gas in relation to the entirely stream of chemical energy of the produced flammable gas mixture (Figs. 8 and 9).

The above indicated positive effect confirms the desirability of the analyzed process, based on the adequate mixing of the ventilation gas stream with the gas stream from demethanation of coal deposits; and all without downloading additional air (oxygen) from the environment. In this way there is the possibility of preparing the good combustible mixture, using available mine gases (the ventilation gas and the gas from demethanation of coal deposits), which can be effectively used for powering of combustion engines; alike the spark ignition, as well as self ignition engines.

## 6 Summary and conclusions

In areas belonging to coal mines remain at the disposal two basic types of mine gases; namely gas from demethanation of coal deposits, and - ventilation gas; containing combustible ingredients (mainly methane). Effective use of these gases is an important technical and ecological issue (greenhouse gas emissions), mainly due to the presence of methane in these gases.

The paper pointed out to the desirability of implementation of appropriately selected mixing process of the ventilation gas with the gas from demethanation of coal deposits; and all without downloading additional air (oxygen) from the environment. For the assessment of the energy usefulness of so origin produced combustible mixture has been proposed system indicator, determining amount of the chemical energy supplied with ventilation gas in relation to the entire stream of chemical energy of the produced gas mixture.

The minimal value of the defined system indicator equals to about 6.9304%, and can be achieved for the stoichiometric (at the air excess ratio  $\lambda = 1$ ) gas mixture, what should be emphasized in terms of the energy utilization efficiency of the mine gases used. The performance procedure, by applying the over-stoichiometric air excess ( $1.5 > \lambda > 1.0$ ) allows for achieving of higher values of effective energy efficiency of the internal combustion gas engine.

In the study was also indicated how can be achieved much higher values of the characteristic indicator; with the increase of the air excess ratio (at  $\lambda > 1$ ) simultaneously grows (Fig. 9) the system indicator,  $\Omega > \Omega_{\min}$ ), and it is worth emphasizing in terms of the system energy utilization efficiency.

Finally has been demonstrated that the technology for preparing of the good quality combustible mixture, using available mine gases, can be effectively used for powering internal combustion engines (spark ignition, self-ignition engines), e.g., as driving elements of the cogeneration systems.

**Acknowledgements** The work was systematically supported and successfully performed by using of statutory funding for research on the faculty Institute of Thermal Engineering of the Silesian University of Technology.

*Received 11 December 2012*

## References

- [1] *Assessment of the Worldwide Market Potential for Oxidizing Coal Ventilation Air Methane*. U.S. Environmental Protection Agency, EPA 430-R-03-002. USEPA, 2003.
- [2] BEARD J.T.: *Mine Gases and Ventilation: Theory and Practical Ventilation, 2nd Edn.* Mc.Graw-Hill Book Company. London 1920.
- [3] BIBBLER C., CAROTHERS P.: *Overview of coal mine gas use technologies*. Second Int. Methane Mitigation Conf., Novosibirsk 2000.
- [4] *Global Anthropogenic Non-CO<sub>2</sub> Greenhouse Gas Emissions: 1990 - 2020*. Office of Atmospheric Programs Climate Change Division. U.S. Environmental Protection Agency, Washington 2006.
- [5] MCPHERSON M.J.: *Subsurface Ventilation and Environmental Engineering with Ventilation Planning*. Chapman State & State Hall, New York 1993.
- [6] NAWRAT S., GATNAR K.: *Estimate of condition and capabilities of VAM utilization from underground coal mines*. *Polityka energetyczna* **11**(2008), 2, 69–83 (in Polish).
- [7] POSTRZEDNIK S., ŻMUDKA Z., PRZYBYŁA G.: *Main conditions and effectiveness of gas fuel use for powering of dual fuel IC self-ignition engine*. *Transp Prob.* **10**(2015), 3, 99–111.
- [8] PRZYBYŁA G., POSTRZEDNIK S., ŻMUDKA Z.: *The combustion process analysis of SI engine fuelled with lean air-gas mixture*. *Sci. Mag. Combust. Eng.* **154**(2013), 3, SC-038 (in Polish).
- [9] SOMERS J.M., SCHULTZ H.L.: *Thermal oxidation of coal mine ventilation air methane*. 12th U.S. North American Mine Ventilation Symp. 2008, 301–306.



archives  
of thermodynamics

Vol. 37(2016), No. 4, 55–72

DOI: 10.1515/aoter-2016-0027

## Performance characteristics of low global warming potential R134a alternative refrigerants in ejector-expansion refrigeration system

SHUBHAM MISHRA  
JAHAR SARKAR\*

Department of Mechanical Engineering, Indian Institute of Technology (B.H.U.), Varanasi, UP 221005, India

**Abstract** Performance assessment of ejector-expansion vapor compression refrigeration system with eco-friendly R134a alternative refrigerants (R152a, R1234yf, R600a, R600, R290, R161, R32, and propylene) is presented for air-conditioning application. Ejector has been modeled by considering experimental data based correlations of component efficiencies to take care of all irreversibilities. Ejector area ratio has been optimized based on maximum coefficient of performance (COP) for typical air-conditioner operating temperatures. Selected refrigerants have been compared based on area ratio, pressure lift ratio, entrainment ratio, COP, COP improvement and volumetric cooling capacity. Effects of normal boiling point and critical point on the performances have been studied as well. Using ejector as an expansion device, maximum improvement in COP is noted in R1234yf (10.1%), which reduces the COP deviation with R134a (4.5% less in basic cycle and 2.5% less in ejector cycle). Hence, R1234yf seems to be best alternative for ejector expansion system due to its mild flammability and comparable volumetric capacity and cooling COP. refrigerant R161 is superior to R134a in terms of both COP and volumetric cooling capacity, although may be restricted for low capacity application due to its flammability.

**Keywords:** Eco-friendly refrigerant; Two-phase ejector; Optimization; COP; Area ratio; Critical temperature

---

\*Corresponding Author. E-mail: jsarkar.mec@itbhu.ac.in

## Nomenclature

$a$	–	cross-sectional area, $m^2$
$C$	–	volumetric refrigeration capacity, $kJ/m^3$
COP	–	coefficient of performance
$h$	–	specific enthalpy, $kJ/kg$
$\dot{m}$	–	mass flow rate, $kg/s$
$p$	–	pressure, $kPa$
$PLR$	–	pressure lift ratio
$q$	–	specific cooling effect, $kJ/kg$
$s$	–	specific entropy, $kJ/kgK$
$t$	–	temperature, $^{\circ}C$
$V$	–	fluid velocity, $m/s$
$v$	–	fluid specific volume, $m^3/kg$
$w$	–	specific work, $kJ/kg$
$x$	–	two-phase quality

## Greek symbols

$\eta$	–	component efficiency
$\mu$	–	entrainment ratio
$\phi$	–	ejector area ratio
$\rho$	–	fluid density, $kg/m^3$

## Subscripts

$b$	–	nozzle exit
$c$	–	condenser
$co$	–	compressor
$d$	–	diffuser
$e$	–	evaporator
$m$	–	mixing
$mn$	–	motive nozzle
$sn$	–	suction nozzle

## 1 Introduction

Today world face a lot of environmental problem such as global warming and ozone layer depletion due to use of high global warming potential (GWP) and ozone depletion potential (ODP) substances used as refrigerants. Hence, the conventional refrigerants are being phased out and need to be replaced by zero ODP and low GWP refrigerants. However, the performance level of many alternatives is slightly lower than conventional refrigerant and hence research and development on the performance improvement of vapor compression system by various cycle modifications has gained special interest recently. One of the very promising modifications is ejector expansion technology, which reduces the throttling losses and com-

pressor work in refrigeration cycle. Nowadays, ejector expansion technology is more popular due to its less complex design, no moving parts, low cost and less maintenance cost [1,2]. Use of ejector in subcritical vapour compression cycle was introduced by Kornhauser [3] and in transcritical cycle by Liu *et al.* [4].

Refrigerant R134a is commonly used for both mobile and residential air conditioning applications. Due to high GWP (Tab. 1), R134a is going to be phased-out and various alternative refrigerants have been proposed [5-7]. Within last decades, many prototypes have been made by using some proposed R134a alternative refrigerants, such as hydrocarbons for residential air-conditioner and R134yf for automobile air-conditioner [8]. In the present study, R290, R600, R600a, R1270, R32, R152a, R161, and R1234yf have been selected based on environmental safety (zero ODP and negligible GWP) as R134a alternatives. Detailed physical, environmental and operational properties of selected refrigerant are given in Tab. 1. The research and development activities on ejector expansion vapor compression refrigeration system have achieved a milestone recently. Worldwide research activities on this area can be broadly classified in the following groups: (i) ejector-expansion transcritical refrigeration systems, (ii) energetic and exergetic performance improvements by using various refrigerants, (iii) CFD simulation and design optimization, (iv) experimental studies and ejector flow control, and (v) various ejector based cycle modifications [9-17]. Although, the ejector expansion refrigeration system with R134a has been studied extensively (both theoretical and experimental), similar studies for its alternatives are very limited. Within selected alternatives, only R290, R600a, R32, R152a, and R1234yf have been studied in ejector expansion refrigeration system by various authors [9,12,14] and most of these works have considered constant mixing pressure in ejector, which is not so realistic. With best of author's knowledge, no previous study has considered all these issues.

Present paper focuses on analyzing the performance of vapor compression system with ejector expansion technology by using eco-friendly refrigerants. Suitable R134a substitutes have been selected for air-conditioning application based on environmental criteria. The ejector has been modeled by taking care of pressure drop occur during mixing and it affect on the ejector performance. Comparison of optimum coefficient performance (COP), COP improvement, ejector area ratio, entrainment ratio, pressure lift ratio and volumetric cooling capacity with R134a, and its eight alternative

Table 1: Physical and environmental properties of R134a and its alternatives.

Refrigerant	Normal boiling point (°C)	Critical temperature (°C)	Critical pressure (MPa)	GWP	Flammability	Safety class
R134a	-26.1	101	4.059	1300	inflammable	A1
R152a	-24.1	113.3	4.520	140	flammable	A2
R290	-42.1	96.7	4.247	20	flammable	A3
Propylene	-47.7	92.4	4.665	3	flammable	A3
R600	-0.53	152	3.796	20	flammable	A3
R600a	-11.7	134.7	3.640	3	flammable	A3
R32	-51.7	78.1	5.784	650	slightly	A2L
R1234yf	-29.5	99.7	3.382	4	slightly	A2L
R161	-37.6	102.1	5.010	12	flammable	A3

refrigerants is done by modeling and simulation considering irreversibility in all components. Effects of refrigerant critical temperature and normal boiling point on COP and volumetric refrigeration capacity are analyzed as well.

## 2 Mathematical modeling and simulation

The layout of the ejector expansion vapour compression cycle is shown in Fig. 1 and pressure-enthalpy diagram in Fig. 2. Motive stream from condenser and suction stream from evaporator are expanded through nozzles (1-1b and 2-2b), which are irreversible processes and may be affected by friction and shock. Refrigerant flows from primary nozzle and secondary nozzle then mix in the mixing chamber (1b-3m-2b). In the mixing chamber, two-phase flow streams mixes in a highly irreversible process which may include two-phase mixing shock wave, which is much thicker than a shock wave in gas-dynamics. The large velocity and temperature mismatch between the motive and suction flows as well as mismatch between liquid and vapor velocities may result in viscous losses and heat transfer, as well as several irreversible oblique shocks, which are commonly referred to as shock train. Hence, the process in the mixing chamber may be characterized by both pressure rise due to compression process (two-phase mixing shock wave or shock train) and the pressure drop due to fluid friction. Af-

ter mixing, refrigerant is discharged through the diffuser (3m-3) by pressure rise above evaporator pressure and enters the separator. In the separator, liquid and vapour are separated; liquid is circulated through expansion valve (6-7) and then evaporator (7-2) to give useful cooling whereas vapour is the directed to the compressor (4-5) and then condenser (5-1).

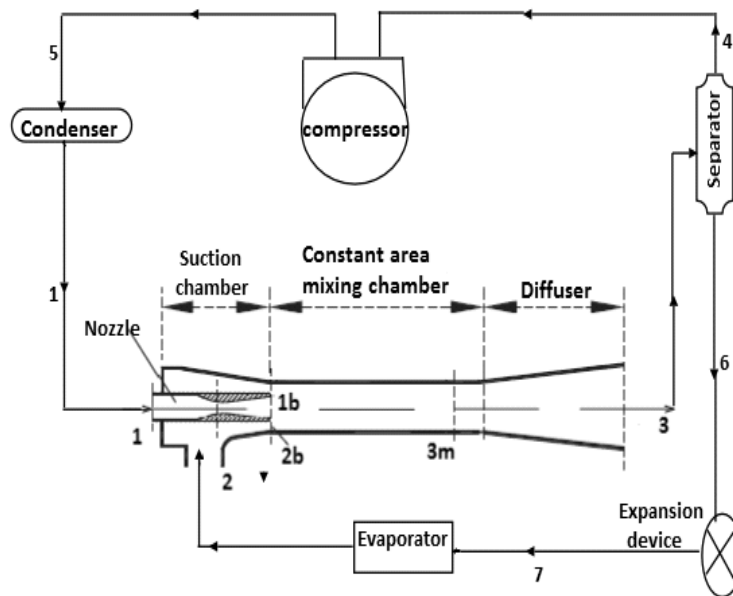


Figure 1: Schematic diagram of ejector expansion refrigeration cycle.

The ejector expansion vapour compression refrigeration cycle has been modeled based on mass, momentum and energy conservations. To simplify the theoretical model, the following assumptions have been made:

- (i) pressure drops in heat exchangers and the connection tubes are negligible,
- (ii) no heat transfer with the environment for the system except in the condenser,
- (iii) refrigerant conditions at the evaporator and condenser exits are saturated,
- (iv) both liquid and vapor streams separated from the separator are saturated,



$$V_{2b} = \sqrt{2(h_2 - h_{2b})}. \quad (4)$$

Then, exit areas of motive and suction nozzles for given flow rates are as follows

$$a_{1b} = \frac{\dot{m}_{mn}}{\rho_{1b}V_{1b}}, \quad (5)$$

$$a_{2b} = \frac{\dot{m}_{sn}}{\rho_{2b}V_{2b}}. \quad (6)$$

Now, the ejector area ratio is defined as [12]

$$\phi = \frac{a_{1b} + a_{2b}}{a_{1b}}. \quad (7)$$

For modeling of the mixing chamber, the mixing efficiency has been used to account for the performance degradation due to both frictional losses as well as two-phase mixing shock wave in the mixing chamber. With assumed mixing efficiency, the mass, momentum and energy balance equations in ejector mixing section for unit total refrigerant mass flow rate are given by a set of equations to be solved simultaneously

$$\rho_{1b}a_{1b}V_{1b} + \rho_{2b}a_{2b}V_{2b} = \rho_{3m}(a_{1b} + a_{2b})V_{3m}, \quad (8)$$

$$p_{2b}(a_{1b} + a_{2b}) + \eta_m [\dot{m}_{mn}V_{1b} + \dot{m}_{sn}V_{2b}] = p_{3m}(a_{1b} + a_{2b}) + (\dot{m}_{mn} + \dot{m}_{sn})V_{3m}, \quad (9)$$

$$\frac{1}{1 + \mu} \left( h_{1b} + \frac{V_{1b}^2}{2} \right) + \frac{\mu}{1 + \mu} \left( h_{2b} + \frac{V_{2b}^2}{2} \right) = h_{3m} + \frac{V_{3m}^2}{2}. \quad (10)$$

At the exit of mixing section, four unknown quantities (density, pressure, enthalpy and velocity) can be found by simultaneous solving of above three equations and property function,  $h_{3m} = f(p_{3m}, \rho_{3m})$ .

Then, by using energy balance and property function, the refrigerant enthalpy and pressure at the diffuser section exit of ejector can be found by

$$h_3 = h_{3m} + \frac{V_{3m}^2}{2}, \quad (11)$$

$$p_3 = p[h_{3m} + \eta_d(h_3 - h_{3m}), s_{3m}]. \quad (12)$$

Assuming thermal equilibrium, steady state and perfect separation (no liquid with saturated vapor stream and no vapor with saturated liquid stream)

and applying mass balance in separator, the entrainment ratio for iteration should satisfy the following equation:

$$\mu = \frac{\dot{m}_{sn}}{\dot{m}_{mn}} = \frac{1 - x_3}{x_3}. \quad (13)$$

Due to negligible pressure drop in the suction nozzle, the process is much less irreversible [18] and hence the isentropic efficiency of suction nozzle has been taken as constant value of 85% [12]. Whereas flows in the motive nozzle, mixing section and diffuser are highly irreversible as discussed earlier [18] and the efficiencies are highly dependent on the fluid properties and ejector geometric parameters. Hence, the fluid pressure ratio and ejector area ratio dependent correlations, developed based on experimental data of R600a [18], have been used, which are given by

$$\eta_{mn} = -0.01615 \left( \frac{p_1}{p_2} \right)^2 + 0.06925 \left( \frac{p_1}{p_2} \right) - \frac{1.32811}{\phi} + \frac{1.40543}{\sqrt{\phi}} + 0.29577, \quad (14)$$

$$\eta_m = -0.50685 \left( \frac{p_1}{p_2} \right)^4 + 5.91466 \left( \frac{p_1}{p_2} \right)^3 - 25.43486 \left( \frac{p_1}{p_2} \right)^2 + 47.90428 \frac{p_1}{p_2} + \frac{12.50076}{\phi^2} - \frac{17.06804}{\phi^{1.5}} + \frac{7.52924}{\phi} - \frac{1.29759}{\sqrt{\phi}} - 32.60447, \quad (15)$$

$$\eta_d = 0.00482 \left( \frac{p_1}{p_2} \right)^2 - 0.06947 \frac{p_1}{p_2} + \frac{0.08833}{\phi} - \frac{0.04263}{\sqrt{\phi}} + 0.85588. \quad (16)$$

Now, compressor exit enthalpy can be found by

$$h_5 = h_4 + \frac{h(p_c, s_4) - h_4}{\eta_{co}}, \quad (17)$$

where the compressor isentropic efficiency has been calculated by the following empirical relation, valid for twin screw compressors with pressure ratio up to 20 [19]

$$\eta_{co} = 0.874 - 0.0134 \frac{p_c}{p_e}. \quad (18)$$

Now, the pressure lift ratio can be calculated by the following equation

$$PLR = \frac{p_3}{p_2}. \quad (19)$$

Volumetric capacity of refrigerant (to decide about the size of compressor) is given by

$$C = (h_2 - h_7) \frac{\mu}{v_4}. \quad (20)$$

Compressor work and refrigeration effects are given by, respectively,

$$w_{co} = \frac{(h_5 - h_4)}{1 + \mu}, \quad (21)$$

and

$$q_e = (h_2 - h_7) \frac{\mu}{1 + \mu}. \quad (22)$$

Coefficient of performance with ejector expansion technology is given by:

$$COP = \frac{q_e}{w_{co}}. \quad (23)$$

Simulation was done on the commercial Engineering Equation Solver (EES) software [20] based on the theoretical model of the ejector expansion vapor compression cycle presented above. Build-in property functions have been used for thermophysical properties of all refrigerants. For given evaporator and condenser temperatures, and secondary nozzle pressure drop, the similar algorithm presented by Sarkar [12] has been used, except the mixing section, where, proper iteration is used to solve mass, momentum, and energy relations simultaneously. Experimental data based correlations have been used for component efficiencies. Total mass flow rate of working fluid has been taken as 1 kg/s. It can be noted that the area ratio can be varied monotonically by changing the suction nozzle pressure drop. Coefficient of performance improvement with respect to basic cycle has been also calculated for all refrigerants.

### 3 Results and discussion

Previous studies (e.g. Sarkar [12]) showed that the COP of ejector expansion system increases initially and then decreases with the increase in ejector area ratio (decrease in secondary nozzle pressure drop) and gives some maximum value, which is due to the fact that the pressure lift ratio is maximum and yields minimum pressure ratio as well as minimum work done through the compressor. Hence, there exists an optimum area ratio yielding maximum cooling COP as well as COP improvement. The knowledge of optimum parameter will be useful to proper adjustment of primary and

secondary nozzle areas in system operation, to get maximum performance. Hence, the performances of R134a and its alternatives in ejector-expansion refrigeration cycle are compared in this study based on the optimum ejector area ratio corresponding to the maximum cooling COP. Optimization has been done in EES [20]. For given component efficiencies, the performance parameters of ejector-expansion cycle at optimum condition are mainly dependent on evaporator and condenser temperatures.

The present numerical simulation code has been validated with previous results by Sarkar [12] available on open literature. However, the constant pressure mixing was assumed by Sarkar [12], which can be easily attained by assuming 100% mixing efficiency. For 40 °C condenser temperature and 5 °C evaporator temperature, the comparisons of various performance parameters (area ratio, entrainment ratio, pressure lift ratio, COP and COP improvement) using R290 and R600a are tabulated in Tab. 2 for mixing efficiency of 100%. As shown, the values are well matched with literature data with the maximum deviation of 5%. Another comparison for R1234yf

Table 2: Validation of present simulation code with Sarkar [12] results.

Refrigerant	Properties	Previous study	Present study	Deviation (%)
R290	$\phi$	6.84	7.118	4
	$\mu$	0.766	0.766	0
	$PLR$	1.0934	1.09	0.3
	COP	6.097	6.035	1
	$\Delta COP$ (%)	12.48	11.81	5.3
R600a	$\phi$	7.53	7.142	5.1
	$\mu$	0.779	0.778	0.12
	$PLR$	1.0887	1.087	0.17
	COP	6.207	6.133	1.19
	$\Delta COP$ (%)	10.19	9.843	3.4

with Li *et al.* [14] shows that for component efficiency  $\eta_m = 95\%$  (others are same), the deviation maximum COP (5.979 in present study and 5.94 in previous study [14]) is about 1%. The code has been also validated with experimental data for R134a [21]. For the condenser temperature at 53.28 °C, and evaporator temperature at 8.67 °C with 12 °C superheat, and 79% compressor isentropic efficiency (calculated based on test data), the entrainment ratio (0.64 experimental and 0.671 predicted) and area ratio

(5.35 experimental and 5.93 predicted) are deviated by 4.7% and 9.8%, respectively. Hence, the validity of the presented mathematical model is confirmed.

To investigate the characteristic of ejector expansion refrigeration technology with selected nine refrigerants (R134a and its alternatives: R152a, R1234yf, R600a, R600, R290, R161, R32, and propylene), the evaporation and condensation temperatures have been taken as 5 °C and 40 °C, respectively, typically used for air-conditioning application. Various performance parameters corresponding to the optimum condition of individual refrigerants have been compared and effects of normal boiling point and critical temperatures were studied to illustrate the various behavioral trends.

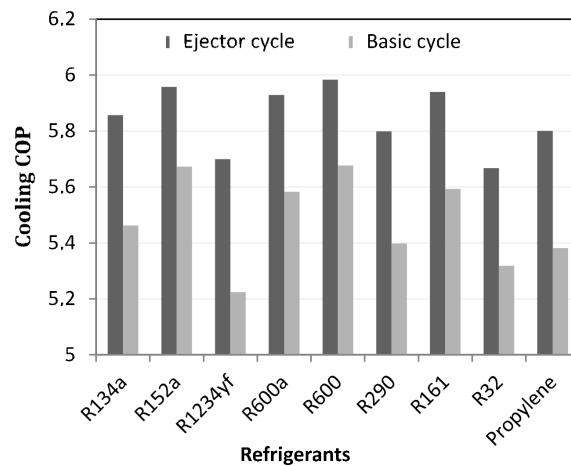


Figure 3: Comparison of maximum cooling COP with and without ejector.

Maximum cooling COP with and without ejector expansion technology with all nine refrigerants is shown in Fig. 3. Coefficient of performance is maximum with R600 followed by R152a and R161, but problem associated with these refrigerants is that, they are flammable in nature. The R1234yf could be good replacement of R134a however its COP is 4.3% lower in simple cycle. But difference in COP reduces after modification, and after modification COP of R1234yf is only 2.6% lower than R134a. Hence, the present study shows that R600 may be a best alternative to R134a (R600 yields about 2% higher COP than R134a) in air conditioning application for low charge system (flammability effect is less dangerous for low charge).

In Fig 4, it is clear that optimum area ratio is different for all differ-

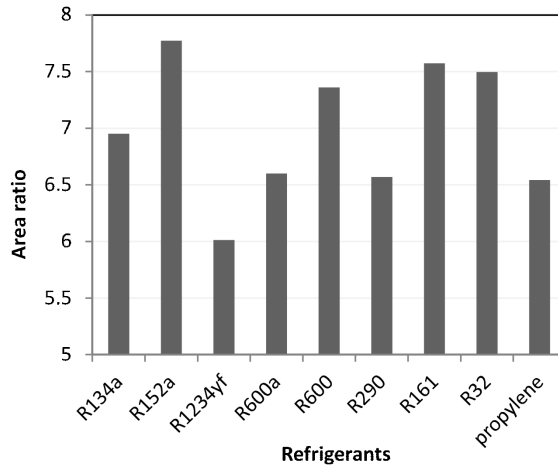


Figure 4: Comparison of optimum ejector area ratio.

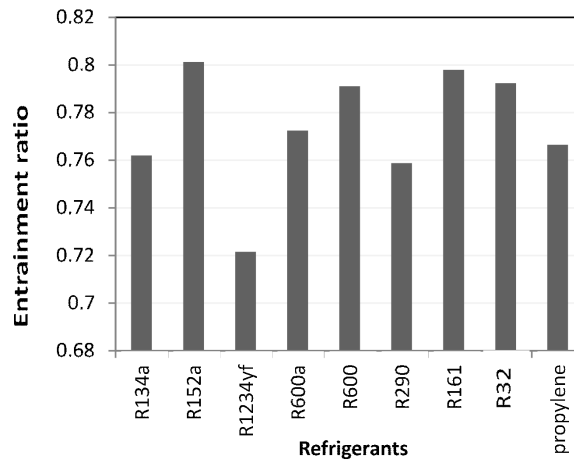


Figure 5: Comparison of optimum entrainment ratio of ejector.

ent refrigerants. It is due to unequal nozzle exit fluid velocity and other properties. Optimum area ratio is found maximum for R152a followed by R161 and R32 (7.773 for R152a, 7.573 for R161, and 7.497 for R32) whereas minimum is obtained for R1234yf (for R1234yf, it is 6.013). Figure 5 shows values of optimum entrainment ratio for all nine refrigerants. Entrainment ratio is the amount of refrigerant which is entrained and flows inside the

evaporator by 1 kg of motive refrigerant flow. For each refrigerant for given operating condition and ejector efficiency optimum entrainment ratio occurs for which COP reaches maximum. Here it is important to note that if the entrainment ratio is less than optimum value, due to high vapor content most of the refrigerant from separator flows through compressor and only a small amount of refrigerant flows through evaporator. Hence COP decreases and compressor size increases. If entrainment ratio is more than an optimum value vapor content reduce and hence pressure lift ratio reduces. This increases compressor work and as a result COP reduces. It is clear from Fig. 5, that R152a has a maximum optimum entrainment ratio (entrainment ratio of R152a is 0.8013). Therefore compressor work is reduced in significant amount in comparison to R152a in ejector expansion technology. Refrigerant R1234yf has lowest optimum entrainment ratio (entrainment ratio of R1234yf is (0.7216) which leads to increase of the compressor size and work.

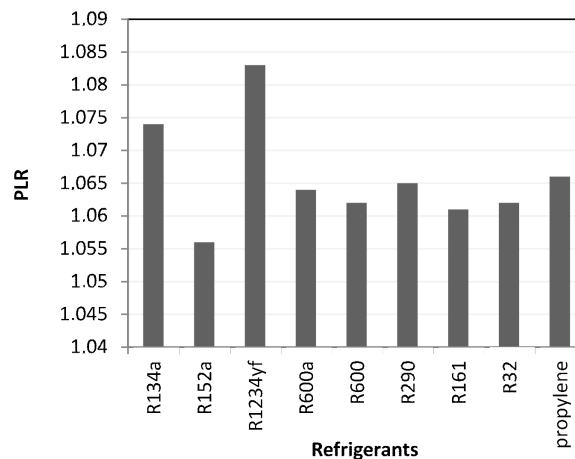


Figure 6: Comparison of pressure lift ratio of ejector.

Figure 6 shows the optimum value for pressure lift ratio (PLR). If pressure lift ratio is high then it increases the suction pressure of compressor and reduces the compressor work done. Hence selection of refrigerant should be done in such a way that its value of optimum pressure lift ratio is as high as possible. The maximum value of pressure lift ratio is noted in R1234yf followed by R134a (PLR for R1234yf is 1.083 and for R134a 1.074). R152a has a minimum pressure lift ratio followed by R161 (PLR for R152a is 1.056

and for R161 is 1.061). COP improvement with all nine refrigerants is shown in Fig. 7. As discussed, higher pressure lift ratio reduces compressor work and increases COP; hence, maximum COP improvement is noted in R1234yf (10.1%) followed by propylene (8.745%) and R290 (8.417%).

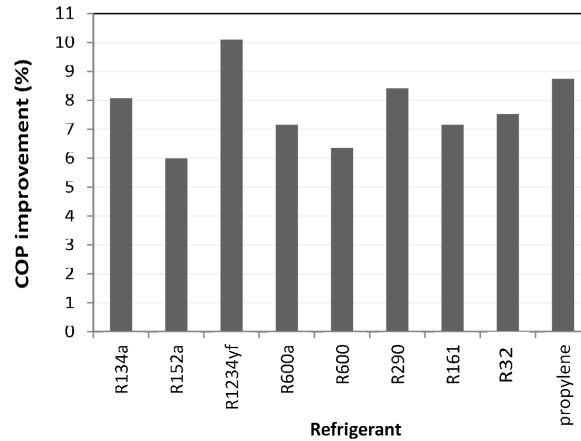


Figure 7: Comparison of COP improvement by using ejector expansion .

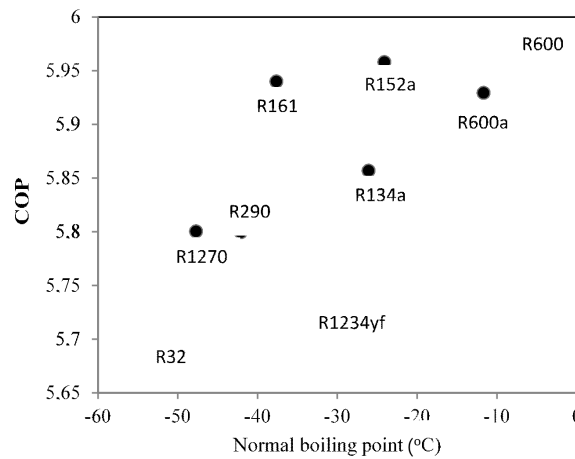


Figure 8: Variation of cooling COP with normal boiling point.

Figure 8 shows variation in COP with respect to normal boiling point of selected refrigerants. It is clear from the figure that there is no direct relation between normal boiling point and COP, but it affects the COP.

If normal boiling point increases the latent heat of vaporization also increases and as a result the refrigerating effect increases with the increasing pressure ratio which subsequently increases the compressor work done. So depending upon dominant factor COP may increase or decrease. Figure 9 shows variation in volumetric refrigeration capacity with the normal boiling point. As the normal boiling point increases the volumetric capacity decreases which is quite obvious especially because high boiling point refrigerant has a low suction pressure and high specific volume at the inlet to the compressor.

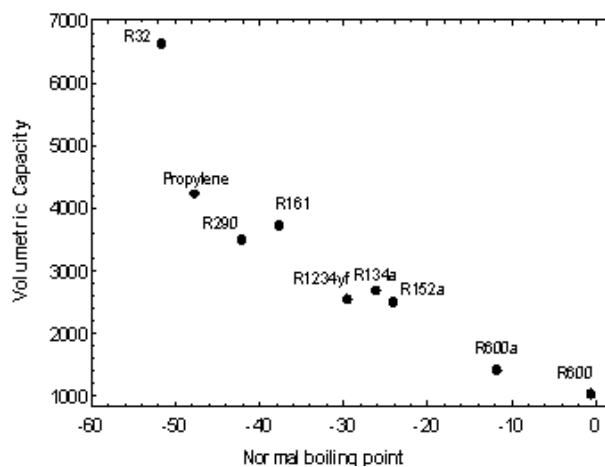


Figure 9: Variation of volumetric capacity with normal boiling point.

From Fig. 10 it is clear that critical temperature of the refrigerant should be high or reduced evaporation temperature should be low for high coefficient of performance. That is due to the fact that the refrigerant with higher critical temperature has a higher latent heat of evaporation and hence higher refrigerating effect. Figure 11 shows variation of volumetric refrigeration capacity with reduced evaporation temperature, which does not give any clear trend. However, as critical temperature increases, the volumetric capacity decreases. From Figs. 8 to 11, it is clear that R600 has a maximum COP but minimum volumetric capacity and R32 has a maximum volumetric capacity but minimum COP; both these conditions are undesirable. Selection of refrigerant based on normal boiling point and critical point requires a trade-off between COP and volumetric capacity.

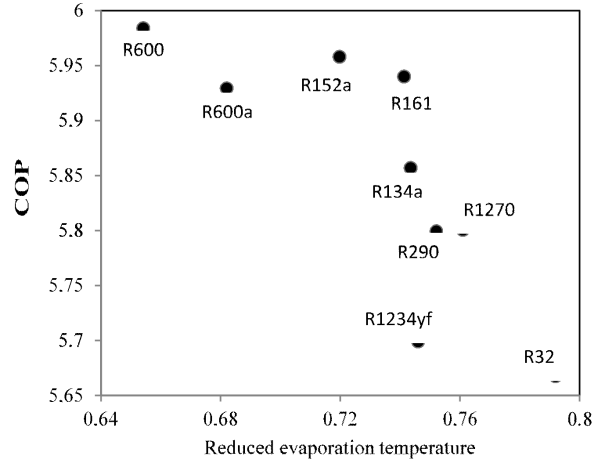


Figure 10: Variation of cooling COP with reduced evaporator temperature.

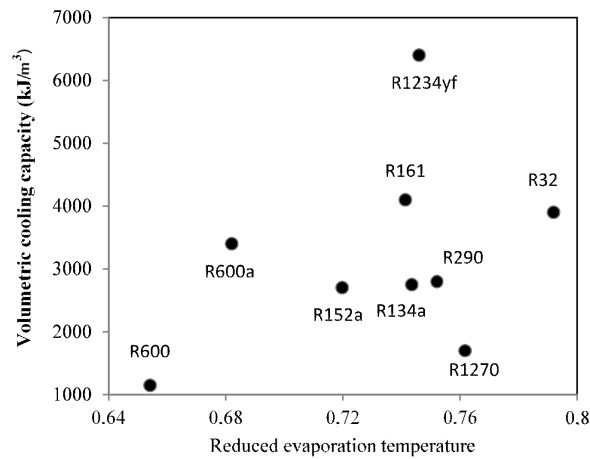


Figure 11: Variation of volumetric capacity with reduced evaporator temperature.

## 4 Conclusions

For air conditioning purpose (40 °C condensing temperature and 5 °C evaporating temperature), assessment of R134a and its possible alternatives (R152a, R1234yf, R600a, R600, R290, R161, R32, and propylene) in ejector expansion vapor compression system is presented in terms of COP, improvement in COP, volumetric refrigeration capacity, area ratio, entrain-

ment ratio and pressure lift ratio. Variations of COP and volumetric capacity with normal boiling point and critical temperature are also presented in the study. Results show that R600 has a maximum COP followed by R152a; however, these refrigerants have low volumetric capacity compared to other refrigerants and another disadvantage with these refrigerants is they are flammable in nature. Refrigerant R32 has maximum volumetric capacity, but its COP is low compared to other refrigerants. R32 is also a high global warming potential refrigerant (GWP of R32 is 650) which is not suitable from the environmental point of view. R1234yf has noted maximum improvement in coefficient of performance among all other refrigerants with ejector expansion technology. Normal boiling point and critical temperature of R1234yf are very close to R134a. R1234yf has a very low GWP (GWP of R1234yf is 4 and for R134a, it is 1300) compared to R134a. Hence R1234yf could be the best replacement of R134a from environmental point of view with only a small performance compromise. Another advantage with R1234yf is that it is mildly flammable, which means it is safer to use compared to other alternative refrigerants. Performances of R290 and propylene are also comparable with R134a but they can be used only by taking a lot of safety measures because they are highly flammable (A3 category (Tab. 1)) in nature. R161 is superior to R134a in terms of both COP and volumetric cooling capacity although it is more flammable and hence can be recommended for a low charge system.

*Received 29 October 2016*

## References

- [1] SARKAR J.: *Ejector enhanced vapor compression refrigeration and heat pump systems – a review*. *Renew. Sust. Energ. Rev.* **16**(2012), 9, 6647–6659.
- [2] ELBEL S., LAWRENCE N.: *Review of recent developments in advanced ejector technology*. *Int. J. Refrig.* **62**(2016), 1–18.
- [3] KORNHAUSER A.A.: *The use of an ejector as a refrigerant expander*. In: *Proc. USNC/IIR-Purdue Refrigeration Conf.* 1990, 10–19.
- [4] LIU J.P., CHEN J.P., CHEN Z.J.: *Thermodynamic analysis on trans-critical R744 vapor compression/ejection hybrid refrigeration cycle*. In: *Proc. 5th IIR G. Lorentzen Conf. on Natural Working Fluids, Guangzhou 2002*, 184–188.
- [5] PARK K.-J., SEO T., JUNG D.: *Performance of alternative refrigerants for residential air-conditioning applications*. *Appl. Energ.* **84**(2007), 10, 985–991.

- [6] GAURAV, KUMAR R.: *Alternatives to R134a (CF<sub>3</sub>CH<sub>2</sub>F) Refrigerant – A Review*. National Conf. on Trends and Advances in Mechanical Engineering, YMCA University of Science & Technology, Faridabad, Haryana 2012.
- [7] BOLAJI B.O.: *Theoretical analysis of the energy performance of three low global warming potential hydro-fluorocarbon refrigerants as R134a alternatives in refrigeration systems*. IMechE, Part A: J. Power Energy **228**(2014), 1, 56–63.
- [8] WANG C.-C.: *System performance of R-1234yf refrigerant in air-conditioning and heat pump system – An overview of current status*. Appl. Thermal Eng. **73**(2014), 2, 1412–1420.
- [9] NEHDI E., KAIROUANI L., BOUZAINA M.: *Performance analysis of the vapour compression cycle using ejector as an expander*. Int. J. Energ. Res. **31**(2007), 4, 364–375.
- [10] YARI M.: *Exegetic analysis of the vapor compression refrigeration cycle using ejector as an expander*. Int. J. Exerg. **5**(2008), 3, 326–340.
- [11] CHAIWONGSA P., WONGWISES S.: *Experimental study on R-134a refrigeration system using a two-phase ejector as an expansion device*. Appl. Thermal Eng. **28**(2008), 5-6, 467–477.
- [12] SARKAR J.: *Performance characteristics of natural refrigerants based ejector expansion refrigeration cycles*. IMechE, Part A: J. Power Energy **223**(2009), 5, 543–550.
- [13] DUDAR A., BUTRYMOWICZ D., ŚMIERCIEW K., KARWACKI J.: *Exergy analysis of operation of two-phase ejector in compression refrigeration systems*. Arch. Thermodyn. **34**(2013), 4, 107–122.
- [14] LI H., CAO F., BU X., WANG L., WANG X.: *Performance characteristics of R1234yf ejector-expansion refrigeration cycle*. Appl. Energ. **121**(2014), 96–103.
- [15] CHEN J., HAVTUN H., PALM B.: *Screening of working fluids for the ejector refrigeration system*. Int. J. Refrig. **47**(2014), 1–14.
- [16] SARKAR J.: *Optimization of ejector-expansion transcritical CO<sub>2</sub> heat pump cycle*. Energ. **33**(2008), 9, 1399–1406.
- [17] ZHAO L., YANG X., DENG S., LI H., YU X.: *Performance analysis of the ejector-expansion refrigeration cycle using zeotropic mixtures*. Int. J. Refrig. **57**(2015), 197–207.
- [18] WANG X., YU J.: *An investigation on the component efficiencies of a small two-phase ejector*. Int. J. Refrig. **71**(2016), 26–38.
- [19] BRUNIN O., FEIDT M., HIVET B.: *Comparison of the working domains of some compression heat pumps and a compression-absorption heat pump*. Int. J. Refrig. **20**(1997), 5, 308–318.
- [20] KLEIN S.A.: *Engineering Equation Solver Professional*. Version V10.042-3D, 2016.
- [21] ERSOY H.K., SAG N.B.: *Preliminary experimental results on the R134a refrigeration system using a two-phase ejector as an expander*. Int. J. Refrig. **43**(2014), 97–110.

archives  
of thermodynamics

Vol. **37**(2016), No. 4, 73–88

DOI: 10.1515/aoter-2016-0028

## Solution of inverse heat conduction equation with the use of Chebyshev polynomials

MAGDA JOACHIMIAK\*  
ANDRZEJ FRĄCKOWIAK  
MICHAŁ CIAŁKOWSKI

Poznan University of Technology, Chair of Thermal Engineering, Piotrowo 3,  
60-965 Poznań, Poland

**Abstract** A direct problem and an inverse problem for the Laplace's equation was solved in this paper. Solution to the direct problem in a rectangle was sought in a form of finite linear combinations of Chebyshev polynomials. Calculations were made for a grid consisting of Chebyshev nodes, what allows us to use orthogonal properties of Chebyshev polynomials. Temperature distributions on the boundary for the inverse problem were determined using minimization of the functional being the measure of the difference between the measured and calculated values of temperature (boundary inverse problem). For the quasi-Cauchy problem, the distance between set values of temperature and heat flux on the boundary was minimized using the least square method. Influence of the value of random disturbance to the temperature measurement, of measurement points (distance from the boundary, where the temperature is not known) arrangement as well as of the thermocouple installation error on the stability of the inverse problem was analyzed.

**Keywords:** Laplace's equation; Boundary inverse problem; Quasi-Cauchy problem; Stability of the inverse problem

### Nomenclature

- $a$  – multinomial coefficient of the function of distribution of temperature  $\tilde{T}(w)$   
 $c$  – multinomial coefficient of the function of distribution of temperature  $T(x, y)$

---

\*Corresponding Author. E-mail: magda.joachimiak@put.poznan.pl

$G$	– element of a vector $\{G\}$
$F$	– element of a vector $\{F\}$
$J$	– functional, the sum of squares of the differences between the temperature calculated at the measurement point and the measured one
$k$	– summing index, Chebyshev nodes
$M$	– number of measuring points
$m$	– number of Chebyshev nodes on the $y$ -axis
$N_1 - 1$	– degree of the polynomial describing unknown distribution of temperature on the $\Gamma_1$ boundary
$n$	– number of Chebyshev nodes on the $x$ -axis
$p$	– summing index, pertains to the temperature measurement points
$T$	– temperature, K
$W_i$	– Chebyshev polynomial of the first kind of $i$ th degree
$w$	– Chebyshev node
$[x]_n$	– integer part of the division of number $x$ by $n$
$x \bmod n$	– remainder of the division of number $x$ by $n$
$x, y$	– Cartesian coordinates
$\ \delta T\ $	– Euclidean norm from the difference between the temperature assumed in a direct problem and that calculated with the inverse problem at points on edge $\Gamma_1$

### Greek symbols

$\Gamma$	– edge of the area
$\gamma$	– multinomial coefficient, pertains to the sought temperature distribution on edge $\Gamma_1$
$\delta$	– absolute error
$\varepsilon$	– distance of the temperature measurement points from edge $\Gamma_1$

### Subscripts

$c$	– calculated value
$dp$	– assumed values in the direct problem
$ip$	– values calculated with the use of the inverse problem
$h, i, j, k$	– summing index
$p$	– summing index
$q$	– number of rows of the Chebyshev nodes on axis $x$ , in which the temperature measurement is performed
<i>random</i>	– values calculated with random disturbance to the temperature measurement

### Superscripts

*	– measured value
$\tilde{T}$	– temperature, function dependent on the Chebyshev node
$\tilde{A}$	– matrix $A^{-1}$ element
$\tilde{F}$	– element of a vector $\{\tilde{F}\}$
$\tilde{G}$	– element of a vector $\{\tilde{G}\}$
"	– second derivative
T	– transpose

## 1 Introduction

In many technological cases, it is impossible to measure temperature on the edge of considered domain or such measurements show significant uncertainties. It is due to the surface high temperature and heat flow by radiation. This problem occurs, for instance, in combustion chambers or in heat-turbine housings. Determination of temperature distribution on the region's boundary is possible through solving the inverse problem. In this paper the boundary-value inverse heat conduction problem with steady boundary was solved with the use of the Laplace and Fourier transforms [1]. A new approach to solving the inverse boundary problem with the use of the Laplace transform consisting in solving the first-order Volterra equation was proposed in [2]. On the other hand the Cauchy problem in the multilayer region for the one-dimensional heat conduction equation was analyzed in [3]. To solve the ill-posed problem, the Fourier transform and the modified Tikhonov regularization technique were used. The Cauchy problem for the Laplace equation was also solved by replacing it by the solution of the Poisson equation based on polyharmonic functions [4]. Paper [5] presents the solution of the mixed inverse problem consisting in the Cauchy problem, the backward heat conduction problem and the heat source recovery problem. To do so, a differential quadrature method and the Lie-group adaptive method were applied. Two new methods of regularization for ill-posed Cauchy problem were considered in [6]. In paper [7] Chebyshev polynomials and the least-squares method were applied to solve the inverse heat conduction problem. Sensitivity of solutions to inverse problems was analyzed in papers [5,8–11]. Coefficient inverse problem was a subject of study in [12], where the thermal conductivity function of a solid was approximated by a polynomial. Inverse problems are applied in technical problems, such as analysis of boilers operation [13], heat exchangers operation [14], processes related to changes of phase of solidifying metal [15].

In this paper, the direct problem and the inverse problem for the Laplace's equation were solved using the Chebyshev polynomials. Sensitivity of the obtained solution to errors in measurement and thermocouple installation were also considered.

## 2 Direct problem

Given is the Laplace's equation

$$\frac{\partial^2 T}{\partial x^2} + \frac{\partial^2 T}{\partial y^2} = 0 \quad (1)$$

with the boundary conditions (Fig. 1):

$$\Gamma_1 : T(x = 1, y) = T_{\Gamma_1}(y) , \quad (2)$$

$$\Gamma_2 : T(x, y = 1) = T_{\Gamma_2}(x) , \quad (3)$$

$$\Gamma_3 : T(x = -1, y) = T_{\Gamma_3}(y) , \quad (4)$$

$$\Gamma_4 : T(x, y = -1) = T_{\Gamma_4}(x) . \quad (5)$$

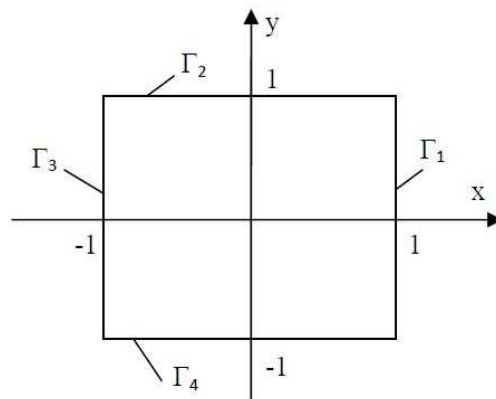


Figure 1: Considered domain.

Temperature assumed on the boundary  $\Gamma = \Gamma_1 \cup \Gamma_2 \cup \Gamma_3 \cup \Gamma_4$  is a continuous function. Temperature distribution in the considered region can be written using Chebyshev polynomials [16]

$$T(x_i, y_j) = \sum_{p=0}^{n-1} \sum_{q=0}^{m-1} c_{pq} W_p(x_i) W_q(y_j) . \quad (6)$$

On the  $x$  and  $y$  axes there are  $n$  and  $m$  nodes, respectively. Inner nodes are the Chebyshev nodes [16]. Equation (1) is required to be satisfied

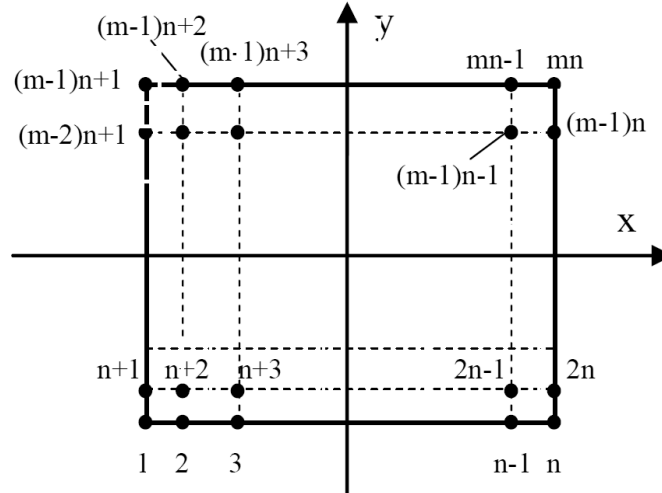


Figure 2: Node enumeration.

in these nodes. After reenumerating nodes (Fig. 2), point  $(x_i, y_j)$  of the table is denoted as the node  $w_l$ , where  $l = (j-1)n + i$ . Dependences  $i = (l-1) \bmod n + 1$  and  $j = \lfloor l-1 \rfloor_n + 1$  occur there. After new numeration of nodes is introduced, temperature distribution can be written as

$$\tilde{T}(w_l) = \sum_{k=1}^{mn} a_k W_{[k-1]_m} \left( x_{(l-1) \bmod n + 1} \right) W_{(k-1) \bmod m} \left( y_{\lfloor l-1 \rfloor_n + 1} \right). \quad (7)$$

Inserting temperature function in the form (8) into Eq. (1) in Chebyshev nodes, we have

$$\sum_{k=1}^{mn} a_k W''_{[k-1]_m} \left( x_{(l-1) \bmod n + 1} \right) W_{(k-1) \bmod m} \left( y_{\lfloor l-1 \rfloor_n + 1} \right) + \sum_{k=1}^{mn} a_k W_{[k-1]_m} \left( x_{(l-1) \bmod n + 1} \right) W''_{(k-1) \bmod m} \left( y_{\lfloor l-1 \rfloor_n + 1} \right) = 0. \quad (8)$$

Moreover, if boundary conditions (2) – (6) are taken into account, the algebraic system of linear equations is obtained

$$\mathbf{A}x = b, \quad (9)$$

where

$$x = \{a_1, a_2, \dots, a_{mn}\}^T, \quad (10)$$

where superscript  $\top$  denotes transpose operation, and

$$b = \left\{ \tilde{T}(w_1), \tilde{T}(w_2), \dots, \tilde{T}(w_n), \tilde{T}(w_{n+1}), 0, \dots, \right. \\ \left. 0, \tilde{T}(w_{2n}), \tilde{T}(w_{2n+1}), 0, \dots, 0, \tilde{T}(w_{3n}), \tilde{T}(w_{3n+1}), 0, \dots \right. \\ \left. \dots, 0, \tilde{T}(w_{(m-1)n}), \tilde{T}(w_{(m-1)n+1}), \tilde{T}(w_{(m-1)n+2}), \dots, \tilde{T}(w_{mn}) \right\}^\top, \quad (11)$$

$$[A_{ij}] \begin{matrix} i = 1, \dots, mn \\ j = 1, \dots, mn \end{matrix} \cdot \quad (12)$$

Elements of matrix  $\mathbf{A}$  corresponding to nodes on the boundary assume the following form:

$$A_{lk} = W_{[k-1]_m} \left( x_{(l-1) \bmod n+1} \right) W_{(k-1) \bmod m} \left( y_{[l-1]_n+1} \right), \quad (13)$$

and for inner nodes we have

$$A_{lk} = W''_{[k-1]_m} \left( x_{(l-1) \bmod n+1} \right) W_{(k-1) \bmod m} \left( y_{[l-1]_n+1} \right) \\ + W_{[k-1]_m} \left( x_{(l-1) \bmod n+1} \right) W''_{(k-1) \bmod m} \left( y_{[l-1]_n+1} \right). \quad (14)$$

If there is an inverse matrix to  $\mathbf{A}$  then the solution is of the following form

$$x = \mathbf{A}^{-1}b. \quad (15)$$

### 3 Inverse problem

It is difficult to perform temperature measurements on the edges of many machines' components. Temperature may be therefore determined by solving boundary inverse problem based on temperature measurements at inner points of the body (Fig. 3) or by solving an inverse Cauchy-type problem based on the known value of the heat flux density and the temperature on the edge  $\Gamma_3$  (Fig. 4).

The inverse problem was solved taking into account conditions (3)–(6) and temperature measurements in Chebyshev nodes. Measuring points were situated in one row (the first type of problem – the inverse boundary problem) or in two rows being close to each other (the second type of problem – the quasi-Cauchy problem). For the first-type problem, calculations included temperature measurements at points  $(x_q, y_i)$ , where  $i = 2, 3, \dots, M + 1$  (Fig. 5). In the second-type problem, points of temperature measurement

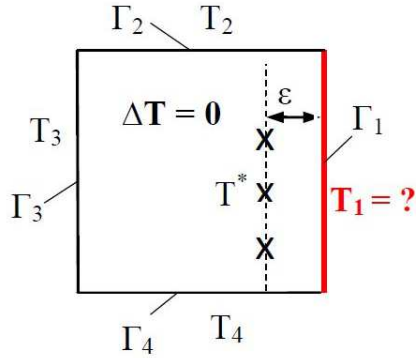


Figure 3: Boundary inverse problem.

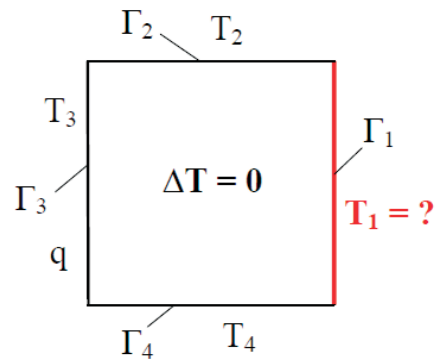


Figure 4: Cauchy-type inverse problem.

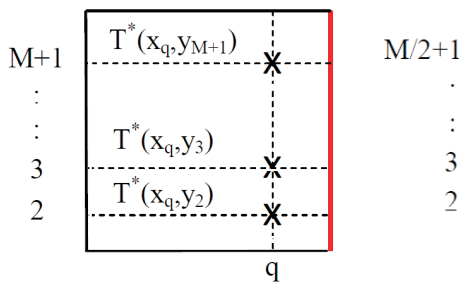


Figure 5: Points of temperature measurement for the inverse boundary problem.

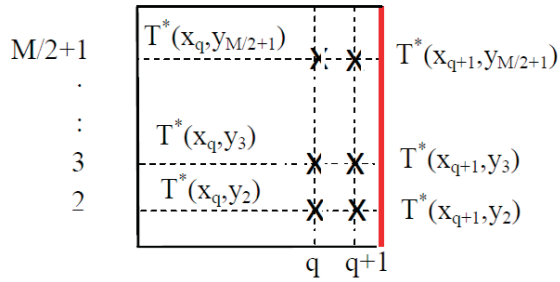


Figure 6: Points of temperature measurement for the quasi-Cauchy problem.

were situated in Chebyshev nodes of coordinates  $(x_q, y_i)$  and  $(x_{q+1}, y_i)$  for  $i = 2, 3, \dots, M/2 + 1$ , where  $M$  is the even number (Fig. 6).

Based on temperature measurement inside the region, unknown temperature distribution on the  $\Gamma_1$  boundary was determined. Unknown course of the boundary condition was approximated by Chebyshev polynomials

$$T_{\Gamma_1}(y) = \sum_{i=1}^{N_1} \gamma_i W_{i-1}(y) , \tag{16}$$

where the values of coefficients  $\gamma_i$  for  $i = 1, 2, \dots, N_1$  are unknown. On the basis of the direct problem, temperature distribution was described by

the formula (8). Unknown values of coefficients  $a_k$  for  $k = 1, 2, \dots, mn$  were determined from the system of linear equations (16), including elements of matrix  $A$  and of vector  $b$  described by formulae (12)–(15). Unknown temperature distribution on the  $\Gamma_1$  boundary corresponds to nodes  $2n, 3n, \dots, (m-1)n$ . Based on (18), the following equalities occur at points on the  $\Gamma_1$  boundary

$$\tilde{T}(w_{jn}) = \sum_{i=1}^{N_1} \gamma_i W_{i-1}(y_j) \quad (17)$$

for  $j = 2, 3, \dots, (m-1)$ . Therefore, Eq. (16) can be written in the form of

$$\{x\} = \mathbf{A}^{-1} \{\tilde{F}\} + \mathbf{A}^{-1} \{\tilde{G}\}, \quad (18)$$

where  $\{\tilde{G}\} = \{0, \dots, 0, \tilde{T}(w_{2n}), 0, \dots, 0, \tilde{T}(w_{3n}), 0, \dots, 0, \tilde{T}(w_{(m-1)n}), 0, \dots, 0\}^T$  and  $\tilde{F}_i = b_i - \tilde{G}_i$  for each  $i = 1, 2, \dots, mn$ . Assuming that  $\{F\} = \mathbf{A}^{-1} \{\tilde{F}\}$  and  $\{G\} = \mathbf{A}^{-1} \{\tilde{G}\}$ , we obtain the solution of the form of

$$\{x\} = \{F\} + \{G\}, \quad (19)$$

where the values of the vector  $\{F\}$  are known, while values of the vector  $\{G\}$  are unknown and can be described by the following relation:

$$G_k = \sum_{j=2}^{m-1} \tilde{A}_{k,jn} \sum_{i=1}^{N_1} \gamma_i W_{i-1}(y_j). \quad (20)$$

Elements of the inverse of the matrix  $\mathbf{A}$  are written as  $\tilde{A}_{k,jn}$ . Hence,

$$a_k = F_k + G_k = F_k + \sum_{j=2}^{m-1} \tilde{A}_{k,jn} \sum_{i=1}^{N_1} \gamma_i W_{i-1}(y_j). \quad (21)$$

Values  $\gamma_i$  for  $i = 1, 2, \dots, N_1$  should be determined from the minimum of functional

$$J = \sum_{p=2}^{M+1} \left[ T_c(x_{q+f(p)}, y_{g(p)}) - T^*(x_{q+f(p)}, y_{g(p)}) \right]^2, \quad (22)$$

where  $f(p) = 0$  for the first-type problem (inverse boundary problem), and  $f(p) = [p-1]_{M/2+1}$  for the second-type problem (quasi-Cauchy problem);

and  $g(p) = p$  for the first-type problem and  $g(p) = 1 + (p - 1) \bmod (M/2 + 1) + [p - 1]_{M/2+1}$  for the second-type problem; the asterisk denotes the measured value. On the basis of the formula (8) we have

$$J = \sum_{p=2}^{M+1} \left[ \sum_{k=1}^{mn} a_k W_{[k-1]_m} (x_{q+f(p)}) W_{(k-1) \bmod m} (y_{g(p)}) - T^* (x_{q+f(p)}, y_{g(p)}) \right]^2. \quad (23)$$

Substituting the dependence (23) into Eq. (25) we have obtained

$$J = \sum_{p=2}^{M+1} \left[ \sum_{k=1}^{mn} \left( F_k + \sum_{j=2}^{m-1} \tilde{A}_{k,jn} \sum_{h=1}^{N_1} \gamma_h W_{h-1} (y_j) \right) \times W_{[k-1]_m} (x_{q+f(p)}) W_{(k-1) \bmod m} (y_{g(p)}) - T^* (x_{q+f(p)}, y_{g(p)}) \right]^2. \quad (24)$$

Functional has its minimum (necessary condition), if for each  $i = 1, 2, \dots, N_1$  the following equality occurs:

$$\frac{\partial J}{\partial \gamma_i} = 0. \quad (25)$$

Hence,

$$\begin{aligned} \frac{\partial J}{\partial \gamma_i} &= 2 \sum_{p=2}^{M+1} \left[ \sum_{k=1}^{mn} \left( F_k + \sum_{j=2}^{m-1} \tilde{A}_{k,jn} \sum_{h=1}^{N_1} \gamma_h W_{h-1} (y_j) \right) \right. \\ &\quad \times W_{[k-1]_m} (x_{q+f(p)}) W_{(k-1) \bmod m} (y_{g(p)}) - T^* (x_{q+f(p)}, y_{g(p)}) \left. \right] \\ &\quad \times \sum_{k=1}^{mn} W_{[k-1]_m} (x_{q+f(p)}) W_{(k-1) \bmod m} (y_{g(p)}) \sum_{j=2}^{m-1} \tilde{A}_{k,jn} W_{i-1} (y_j) \end{aligned} \quad (26)$$

Applying substitutions  $C_1(i, p) = \sum_{k=1}^{mn} W_{[k-1]_m} (x_{q+f(p)}) W_{(k-1) \bmod m} (y_{g(p)}) \sum_{j=2}^{m-1} \tilde{A}_{k,jn} W_{i-1} (y_j)$  and  $C_2(k, p) = W_{[k-1]_m} (x_{q+f(p)}) W_{(k-1) \bmod m} (y_{g(p)})$  we have obtained

$$\begin{aligned} \frac{\partial J}{\partial \gamma_i} &= 2 \sum_{p=2}^{M+1} C_1(i, p) \left[ \sum_{k=1}^{mn} \left( F_k + \sum_{j=2}^{m-1} \tilde{A}_{k,jn} \sum_{h=1}^{N_1} \gamma_h W_{h-1} (y_j) \right) \right. \\ &\quad \times C_2(k, p) - T^* (x_{q+f(p)}, y_{g(p)}) \left. \right]. \end{aligned} \quad (27)$$

Therefore, taking into account the equality

$$C_3(i) = \sum_{p=2}^{M+1} T^*(x_{q+f(p)}, y_{g(p)}) C_1(i, p)$$

we have

$$\frac{1}{2} \frac{\partial J}{\partial \gamma_i} = -C_3(i) + \sum_{p=2}^{M+1} C_1(i, p) \sum_{k=1}^{mn} C_2(k, p) \left( F_k + \sum_{j=2}^{m-1} \tilde{A}_{k,jn} \sum_{h=1}^{N_1} \gamma_h W_{h-1}(y_j) \right). \quad (28)$$

Suppose that  $C_4(p) = \sum_{k=1}^{mn} C_2(k, p) F_k$ , then

$$\frac{1}{2} \frac{\partial J}{\partial \gamma_i} = -C_3(i) + \sum_{p=2}^{M+1} C_1(i, p) \left[ C_4(p) + \sum_{k=1}^{mn} C_2(k, p) \sum_{j=2}^{m-1} \tilde{A}_{k,jn} \sum_{h=1}^{N_1} \gamma_h W_{h-1}(y_j) \right]. \quad (29)$$

Substituting  $C_5(i) = \sum_{p=2}^{M+1} C_1(i, p) C_4(p)$  we have obtained

$$\frac{1}{2} \frac{\partial J}{\partial \gamma_i} = -C_3(i) + C_5(i) + \sum_{p=2}^{M+1} C_1(i, p) \sum_{k=1}^{mn} C_2(k, p) \sum_{j=2}^{m-1} \tilde{A}_{k,jn} \sum_{h=1}^{N_1} \gamma_h W_{h-1}(y_j). \quad (30)$$

For  $C_6(i) = -C_3(i) + C_5(i)$  we have

$$\frac{1}{2} \frac{\partial J}{\partial \gamma_i} = C_6(i) + \sum_{p=2}^{M+1} C_1(i, p) \sum_{k=1}^{mn} C_2(k, p) \sum_{j=2}^{m-1} \tilde{A}_{k,jn} \sum_{h=1}^{N_1} \gamma_h W_{h-1}(y_j). \quad (31)$$

After permuting summation, we have obtained

$$\frac{1}{2} \frac{\partial J}{\partial \gamma_i} = C_6(i) + \sum_{h=1}^{N_1} \gamma_h \sum_{p=2}^{M+1} C_1(i, p) \sum_{k=1}^{mn} C_2(k, p) \sum_{j=2}^{m-1} \tilde{A}_{k,jn} W_{h-1}(y_j). \quad (32)$$

We have applied the substitution  $C_7(i, h) = \sum_{p=2}^{M+1} C_1(i, p) \sum_{k=1}^{mn} C_2(k, p) \sum_{j=2}^{m-1} \tilde{A}_{k,jn} W_{h-1}(y_j)$ . Therefore,

$$0 = \frac{1}{2} \frac{\partial J}{\partial \gamma_i} = C_6(i) + \sum_{h=1}^{N_1} \gamma_h C_7(i, h). \quad (33)$$

Hence, for each  $i = 1, 2, \dots, N_1$

$$-C_6(i) = \sum_{h=1}^{N_1} \gamma_h C_7(i, h). \quad (34)$$

Matrix equation with unknown vector  $\{\gamma\}$  can be written in the form:

$$\{-C_6\} = [C_7] \{\gamma\} . \quad (35)$$

If there is an inverse matrix to the matrix  $[C_7]$ , then

$$\{\gamma\} = [C_7]^{-1} \{-C_6\} . \quad (36)$$

## 4 Numerical example

It was assumed that temperature distribution in the whole region can be described by the following function

$$T(x, y) = \sinh x \sin y . \quad (37)$$

Calculations were made for  $n = m = 10$  nodes along  $x$  and  $y$  axes. By means of solving the direct problem, values of temperature for selected inner nodes were determined; these values were assumed as measured values to test the program. Measured values were disturbed by values  $\delta_{random}$  ranging from 0 to 0.05 of the temperature maximum value. The mean square deviation of set values in the direct problem from the values calculated with the use of inverse problem method in nodes on the  $\Gamma_1$  boundary was described by the relation

$$\|\delta T\| = \sqrt{\sum_{i=1}^m [T_{dp}(x=1, y_i) - T_{ip}(x=1, y_i)]^2} . \quad (38)$$

Two types of solution were considered. The first one was the boundary inverse problem, where one row of measuring points was included (Fig. 7a). For the quasi-Cauchy problem, temperature measurement was performed in two rows (Fig. 7b). Measuring points for both problems coincided with Chebyshev nodes.

An influence of changes in measuring points arrangement on the accuracy of temperature distribution on the  $\Gamma_1$  boundary was studied. The measure of accuracy are values  $\|\delta T\|$  described by the formula (38).

For the first type of inverse problem, it was assumed that  $M = 8$  and  $N_1 = 8$ . Values  $\|\delta T\|$  were calculated; they grow with relocating temperature measuring points from the  $\Gamma_1$  boundary to the  $\Gamma_3$  boundary (Fig. 8). They reach their maximum for the second row of Chebyshev nodes. Decreasing value  $\|\delta T\|$  for  $q$  amounting to 3, 5 or 7 results from nonuniform

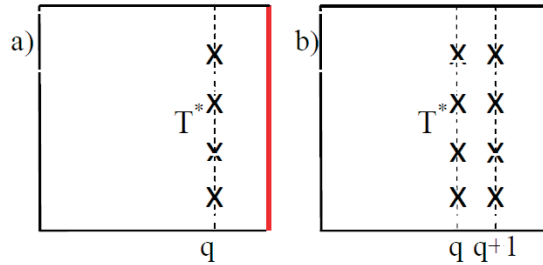


Figure 7: a) Boundary inverse problem, b) Quasi-Cauchy problem.

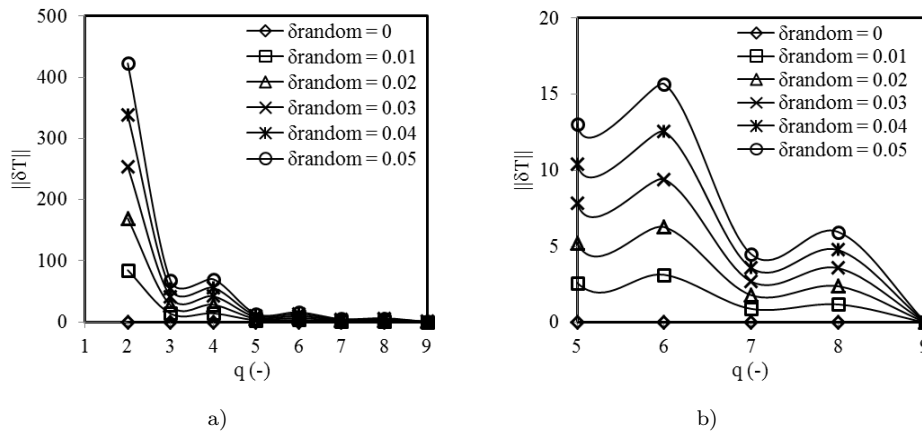


Figure 8: Values  $\|\delta T\|$  for the boundary problem with temperature measurements in the Chebyshev nodes  $x_q$  for  $q$ : a) from 2 to 9; b) from 5 to 9, including a random disturbance to the temperature measurement  $\delta_{random}$ .

arrangement of Chebyshev nodes enabling for fine meshing of collocation points close to the boundary of the region. Increase of the random disturbance to the temperature measurement  $\delta_{random}$  from the value of 0 to 0.05 results in linear increase of the value  $\|\delta T\|$  (Fig. 9). Values  $\|\delta T\|$  amounted from  $3.45 \times 10^{-16}$  for temperature measurement in nodes closest to the  $\Gamma_1$  boundary and  $\delta_{random} = 0$  to 422.76 for measuring points situated in the second row of nodes and  $\delta_{random} = 0.05$  (Tab. 1).

In calculations for the inverse problem of the second type, it was assumed that  $M = 16$  and  $N_1 = 8$ . Calculations were made for two rows of measuring points of coordinates  $x$  coinciding with Chebyshev  $x_q$  and  $x_{q+1}$  nodes. For  $q = 3$ , the value  $\|\delta T\|$  is maximal, what is presented in Fig. 10 and in Tab. 2. Increase of the random disturbance to the temperature mea-

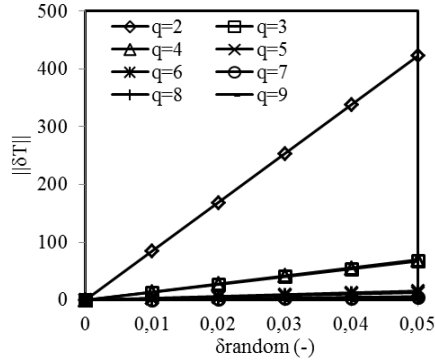


Figure 9: Values  $\|\delta T\|$  for the boundary inverse problem depending on the random disturbance to the temperature measurement  $\delta_{random}$ .

Table 1: Values  $\|\delta T\|$  for the inverse boundary problem.

$q$	$\delta_{random} = 0$	$\delta_{random} = 0.01$	$\delta_{random} = 0.02$
2	$1.72 \times 10^{-9}$	84.55	169.10
3	$7.89 \times 10^{-12}$	13.48	26.96
4	$1.04 \times 10^{-11}$	13.96	27.92
5	$2.92 \times 10^{-12}$	2.60	5.21
6	$7.21 \times 10^{-11}$	3.14	6.27
7	$3.63 \times 10^{-13}$	0.90	1.80
8	$6.97 \times 10^{-13}$	1.19	2.38
9	$3.45 \times 10^{-16}$	$0.90 \times 10^{-2}$	$1.80 \times 10^{-2}$
$q$	$\delta_{random} = 0.03$	$\delta_{random} = 0.04$	$\delta_{random} = 0.05$
2	253.66	338.21	422.76
3	40.44	53.92	67.40
4	41.88	55.84	69.79
5	7.81	10.41	13.02
6	9.41	12.54	15.68
7	2.70	3.60	4.49
8	3.57	4.76	5.96
9	$2.70 \times 10^{-2}$	$3.60 \times 10^{-2}$	$4.50 \times 10^{-2}$

surement  $\delta_{random}$  causes linear increase of mean square deviation of the set values from the values calculated on the  $\Gamma_1$  boundary (Fig. 11).

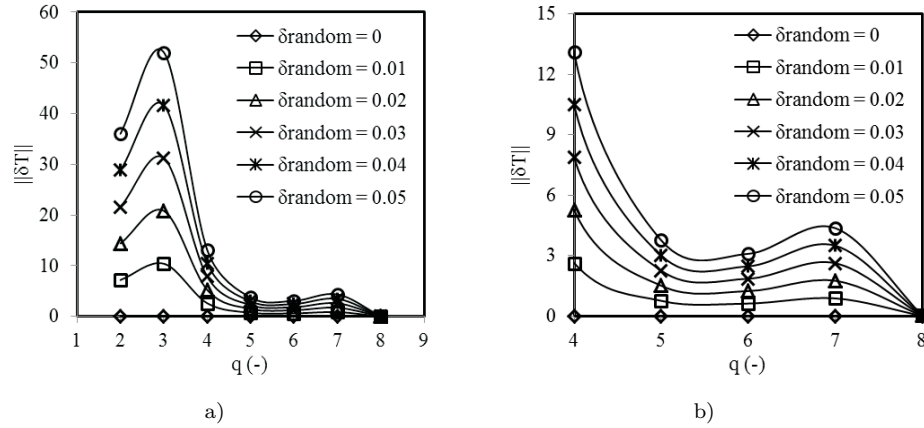


Figure 10: Values  $\|\delta T\|$  for quasi-Cauchy problem with temperature measurement in Chebyshev  $x_q$  and  $x_{q+1}$  nodes for  $q$ : a) from 2 and 3 to 8 and 9; b) from 4 and 5 to 8 and 9, including the random disturbance to the temperature measurement  $\delta_{random}$ .

Table 2: Values  $\|\delta T\|$  for quasi-Cauchy problem.

$q$	$\delta_{random} = 0$	$\delta_{random} = 0.01$	$\delta_{random} = 0.02$
2	$8.14 \times 10^{-12}$	7.21	14.41
3	$8.93 \times 10^{-12}$	10.42	20.84
4	$3.28 \times 10^{-12}$	2.62	5.24
5	$1.22 \times 10^{-12}$	0.75	1.50
6	$7.73 \times 10^{-13}$	0.62	1.23
7	$3.29 \times 10^{-13}$	0.87	1.75
8	$3.42 \times 10^{-16}$	$6.85 \times 10^{-3}$	$1.37 \times 10^{-2}$
$q$	$\delta_{random} = 0.03$	$\delta_{random} = 0.04$	$\delta_{random} = 0.05$
2	21.62	28.82	36.03
3	31.25	41.67	52.09
4	7.87	10.49	13.11
5	2.25	3.01	3.76
6	1.85	2.47	3.09
7	2.62	3.49	4.37
8	$2.06 \times 10^{-2}$	$2.74 \times 10^{-2}$	$3.4 \times 10^{-2}$

## 5 Conclusions

In this paper two types of inverse problem for the Laplace's equation in the rectangular domain were solved. The form of the solution was written as

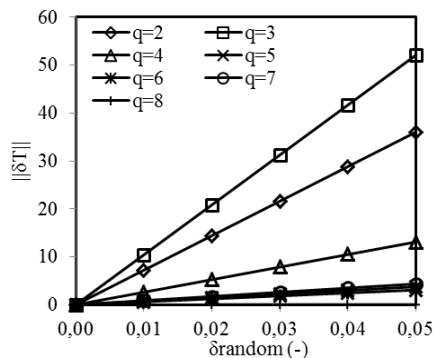


Figure 11: Values  $\|\delta T\|$  for quasi-Cauchy problem depending on the random disturbance to the temperature measurement  $\delta_{random}$ .

the linear combination of Chebyshev polynomials. Influence of changes in measuring points arrangement and random disturbance to the temperature measurement on the mean square deviation of the set values from the values calculated on the  $\Gamma_1$  boundary was considered. Furthermore, the temperature distribution was sought on the  $\Gamma_1$  boundary. Values  $\|\delta T\|$  reach their maximum for  $q = 2$  and  $q = 3$ , what results from the arrangement of collocation nodes. Calculation model brings positive results for measuring points situated in Chebyshev nodes closest to the  $\Gamma_1$  boundary, even for the disturbance to the temperature measurement  $\delta_{random} = 0.05$ . Relocation of measuring points into the  $\Gamma_3$  boundary worsens significantly results of calculations. For calculations without disturbance to the measurement data ( $\delta_{random} = 0$ ), the model returns positive results, irrespective of measuring points arrangement.

Received 18 May 2016

## References

- [1] YAPAROVA N.: *Numerical methods for solving a boundary-value inverse heat conduction problem*. Inverse Probl. Sci. En. **22**(2014), 5, 832–847.
- [2] SOLODUSHA S.V., YAPAROVA N.M.: *Numerical solving an inverse boundary value problem of heat conduction using Volterra equations of the first kind*. Num. Anal. Appl. **8**(2015), 3, 267–274.
- [3] XIONG X.T., HON Y.C.: *Regularization error analysis on a one-dimensional inverse heat conduction problem in multilayer domain*. Inverse Probl. Sci. En. **21**(2013), 5, 865–887.

- [4] FRĄCKOWIAK A., BOTKIN N.D., CIAŁKOWSKI M., HOFFMANN K.H.: *Iterative algorithm for solving the inverse heat conduction problems with the unknown source function*. Inverse Probl. Sci. En. **23**(2015), 6, 1056–1071.
- [5] LIU C.S.: *An iterative algorithm for identifying heat source by using a DQ and a Lie-group method*. Inverse Probl. Sci. En. **23**(2015), 1, 67–92.
- [6] NGUYEN H.T., LUU V.C.H.: *Two new regularization methods for solving sideways heat equation*. J. Inequal. Appl. **65**(2015), 1–17.
- [7] SHIDFAR A., KARAMALI G.R., DAMIRCHI J.: *An inverse heat conduction problem with a nonlinear source term*. Nonlinear Analysis **65**(2006), 615–621.
- [8] WANG F., CHEN W., QU W., GU Y.: *A BEM formulation in conjunction with parametric equation approach for three-dimensional Cauchy problems of steady heat conduction*. Eng. Anal. Bound. Elem. **63**(2016), 1–14.
- [9] LIU C.S., KUO C.L., CHANG J.R.: *Recovering a heat source and initial value by a Lie-group differential algebraic equations method*. Numer. Heat Tr. B-Fund. **67**(2015), 231–254.
- [10] CIAŁKOWSKI M., GRYSA K.: *A sequential and global method of solving an inverse problem of heat conduction equation*. J. Theor. App. Mech.-Pol. **48**(2010), 1, 111–134.
- [11] JOACHIMIAK M., CIAŁKOWSKI M.: *Optimal choice of integral parameter in a process of solving the inverse problem for heat equation*. Arch. Thermodyn. **35**(2014), 3, 265–280.
- [12] MIERZWICZAK M., KOŁODZIEJ J.A.: *The determination temperature-dependent thermal conductivity as inverse steady heat conduction problem*. Int. J. Heat . Mass Tran. **54**(2011), 790–796.
- [13] TALER J., TALER D., LUDOWSKI P.: *Measurements of local heat flux to membrane water walls of combustion chambers*. Fuel **115**(2014), 70–83.
- [14] TALER D., SURY A.: *Inverse heat transfer problem in digital temperature control in plate fin and tube heat exchangers*. Arch. Thermodyn. **32**(2011), 4, 17–31.
- [15] MAROIS M.A., M. DÉSILETS M., LACROIX M.: *What is the most suitable fixed grid solidification method for handling time-varying inverse Stefan problems in high temperature industrial furnaces?*. Int. J. Heat Mass Tran. **55**(2012), 5471–5478.
- [16] PASZKOWSKI S.: *Numerical application of multinomials and Chebyshev series*. PWN, Warsaw 1975 (in Polish).

# Thermodynamic study on complex parts of the sphere and ellipsoid of a nuclear explosive device

GOU ZHENZHI<sup>a,b\*</sup>  
HE BIN<sup>a</sup>  
YANG GUILIN<sup>a</sup>

<sup>a</sup> Xiñan High Technology Institute , Xiñan, 710025, China

<sup>b</sup> Troops number 96421, Baoji, 721012, China

**Abstract** Because the heat release of plutonium material, the composite structure is heated and the stress and strain of the composite structure will increase, which will affect the thermodynamic properties of the structure. The thermodynamic analysis of complex structures, which are composed of concentric structures of plutonium, beryllium, tungsten, explosives, and steel, was carried out. The results showed that when the structure is spherical, the temperature is higher than that of the ellipsoid structure. Stress of the elliptical structure is greater than the spherical structure. This study showed that the more flat the shell is, the greater the stress concentration point occurs at the long axis, and the maximum stress occurs at the beryllium layer. These conclusions provide theoretical support for the plutonium composite component testing.

**Keywords:** Plutonium component; Thermodynamic analysis; Numerical simulation; Temperature field; Stress field

## 1 Introduction

The plutonium element in nuclear explosive device is a radioactive element, which emits a large amount of energy in the radioactive decay and fission process. Nuclear explosive devices, as the most important part of nuclear

---

\*Corresponding Author. E-mail: zhenzhi3644@163.com

weapon, must be guaranteed by good mechanical performance index, which is the basis of the deterrent force. Therefore, it is necessary to analyze thermal effect of nuclear explosive device, and to determine its thermodynamic properties. In order to study the effect of thermal stress on the mechanical properties of the whole device, the nuclear explosive device, which is commonly used in academic research, in many papers and webs [1,3] has been considered.

In 1995, Zhao Ru calculated nitrogen temperature is 77 K under the condition of safe removal of nuclear warheads [5]. In 2005 Xiao Gang simulated thermal coupling calculation of the open model of nuclear device, and conclusions show the highest temperature of the primary structure can reach 390 K in the ideal state [4]. Gao Zhengming considered that the Steven model can not exist in engineering field because the heat stress is too high [2]. There is no research on the complex ellipsoid structure with plutonium layer.

The schematic diagram of nuclear explosive device is shown in Figs. 1 and 2, and structure layout is obtained and simplified according to the inner data. The device parts from inside to outside in turn are plutonium, beryllium, tungsten, explosives, and steel. In order to analyze the effect of thermal stress on the device of different shapes, the three kinds of devices have been analysed, which are: spherical shell the same thickness but elliptical shell, and the different thickness of elliptical shell.

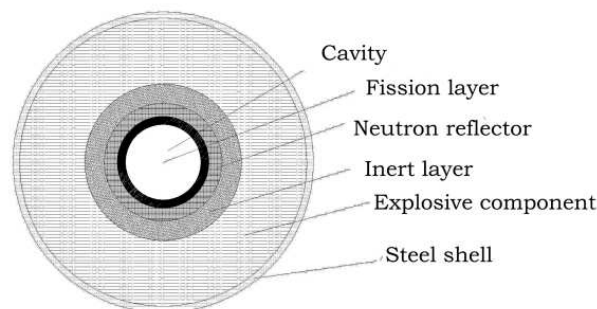


Figure 1: Schematic diagram of complicated multiplelayer components.



Figure 2: Schematic diagram of W88 nuclear explosive device.

## 2 Thermodynamic analysis of a spherical model

For arbitrary time and material, the heat conduction partial differential equation is

$$\frac{\partial}{\partial x} \left( \lambda_{xx} \frac{\partial T}{\partial x} \right) + \frac{\partial}{\partial y} \left( \lambda_{yy} \frac{\partial T}{\partial y} \right) + \frac{\partial}{\partial z} \left( \lambda_{zz} \frac{\partial T}{\partial z} \right) + q_v = \rho c \frac{\partial T}{\partial t}, \quad (1)$$

where  $q_v$  is the thermal strength of solution,  $T$  – temperature field distribution function,  $t$  – time,  $\lambda_{xx}, \lambda_{yy}, \lambda_{zz}$  – coefficients of thermal conductivity along  $X, Y,$  and  $Z$  direction,  $\rho$  and  $c$  – density and thermal conductivity of material respectively, and  $x, y, z$  are the Cartesian coordinates.

When  $\rho, c,$  and  $\lambda$  are constant, the formula can be simplified as [6]

$$a \left( \frac{\partial^2 T}{\partial x^2} + \frac{\partial^2 T}{\partial y^2} + \frac{\partial^2 T}{\partial z^2} \right) + \frac{q_v}{\rho c} = \frac{\partial T}{\partial t}. \quad (2)$$

where  $a = \frac{\lambda}{\rho c}$  is the temperature or diffusion coefficient.

The boundary conditions of the first kind are embodied in the heat exchange from the external temperature field to internal one. Knowing boundary temperature value can obtain the solution of internal heat equation [8]

$$\lambda \frac{\partial T}{\partial x} n_x + \lambda \frac{\partial T}{\partial y} n_y + \lambda \frac{\partial T}{\partial z} n_z = T_s(x, y, z, t),$$

where  $n_x$ ,  $n_y$  and  $n_z$  are the cosine functions in the direction of boundary, and  $T_s$  denotes temperature on the surface of the object.

Thermodynamic properties of the component material and spherical structure size are given in Tabs. 1 and 2, respectively. Spherical structure model and its computational grid division is shown in Fig. 4 and in Tab. 2. The steel shell is in contact with air, and heat convection coefficient is  $5 \text{ W/m}^2$ . The decay power of the plutonium material with time is shown in Fig. 3, whereas decay heat power is about  $0.001857\text{--}0.001863 \text{ W/kg}$ . Therefore, decay power can be approximately taken as  $4.0 \times 10^5 \text{ W/mm}^3$ . The outer surface of steel shell is fixed. Elliptical shell is thickness uniform and thickness ratio along the long and short axis direction is 2:1.

The simulation of the nuclear explosive device using a computational thermodynamic model enable high-quality analysis of main parameters that effect on device features, providing realistic estimation of the decisive factors. Temperature distribution for the spherical structure is shown in Fig. 5.

Table 1: Thermodynamic parameters of complex parts.

Material	Thermal conductivity	Density ( $\text{kg/m}^3$ )	Specific heat ( $\text{J/kg K}$ )	Modulus of elasticity (GPa)	Poisson's ratio	Expansion coefficient ( $10^6/\text{K}$ )
Plutonium [4]	27.6	18950	113	100	0.22	12.55
Beryllium [5]	188.3	1848	1883	411	0.07	1.3
Wolfram [5]	145	19260	134	5800	0.28	4.45
Explosive [5]	0.64	1670	690	5.8	0.34	7
Steel [5]	16.3	7850	502.4	210	0.30	17

Table 2: Spherical component size parameter.

Spherical shell size	Layer				
	Plutonium	Beryllium	Tungsten	Explosive	Steel
Inner radius	57.7	70	90	120	220
Outer radius	70	90	120	220	230
Thickness	12.3	20	30	100	10

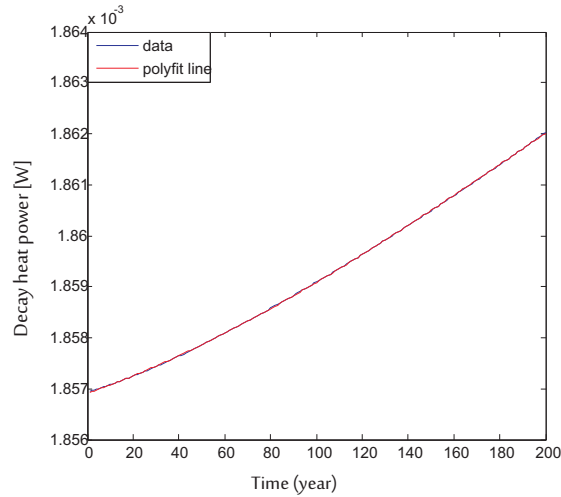


Figure 3: Plutonium decay power.

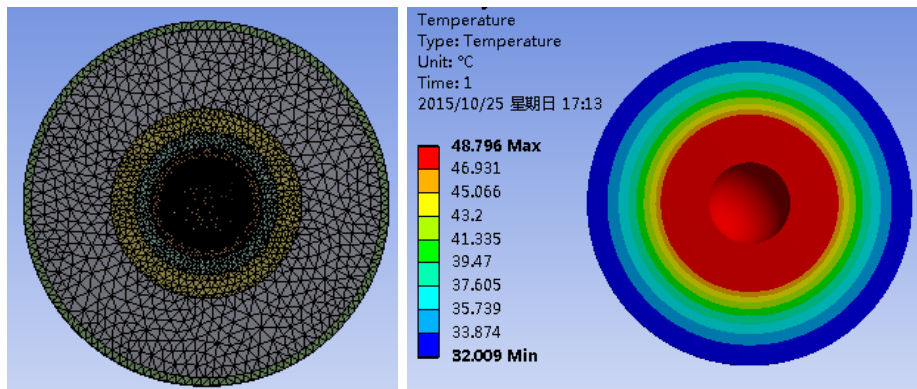


Figure 4: Grid division.

Figure 5: Temperature contour.

As can be seen from Figs. 6 and 7, the maximum heat flux is at the junction of plutonium and beryllium, and the maximum heat flux reached is  $441.89 \text{ W/m}^2$ . According to Fig. 6, it can be seen that the thermal conductivity of beryllium is  $441.89 \text{ W/m}^2$ , so the temperature difference of two surfaces is the largest, as well as the heat flux of plutonium and beryllium.

It can be seen in Figs. 8 and 9 that the equivalent elastic strain occurs on inner surface of the explosive and the tungsten, while the elastic strain of the tungsten material is the smallest. From Figs. 10 and 11, we can see

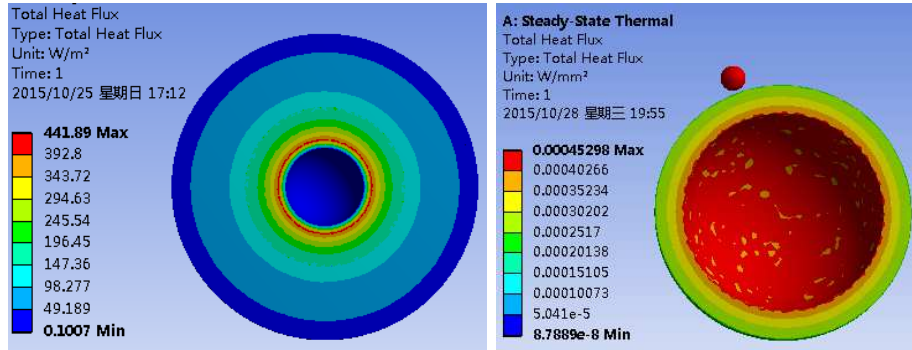


Figure 6: Heat flow density contour. Figure 7: Heat flow density contour of beryllium.

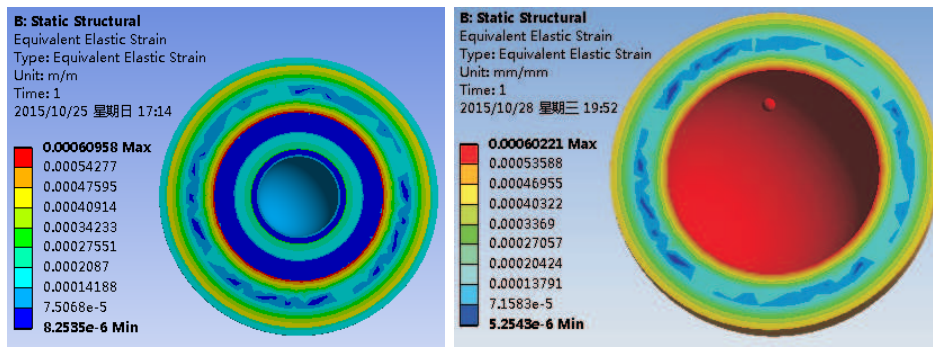


Figure 8: Equivalent elastic strain. Figure 9: Equivalent strain contour of explosive.

that the stress of the inner surface of beryllium component and the outside surface of plutonium component reaches the maximum of 89 MPa. As can be seen from Fig. 12, the total maximum deformation locates at explosive part, while it shows that the total deformation of the steel shell is zero, because it is set into a steel shell as a fixed structure.

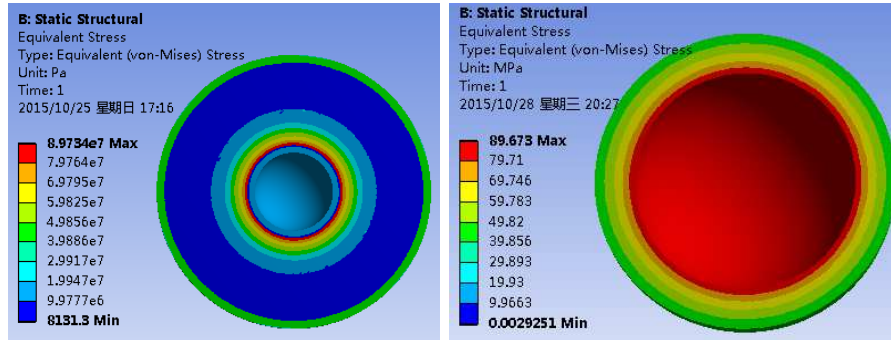


Figure 10: Equivalent stress contour. Figure 11: Equivalent stress contour of beryllium.

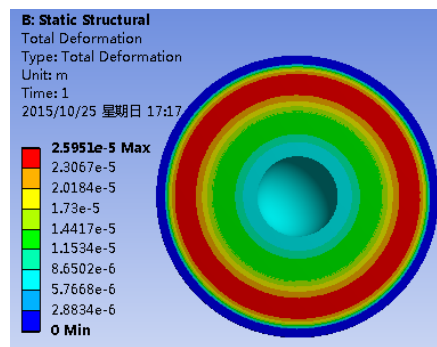


Figure 12: Total deformation contour of sphere structure.

### 3 Thermodynamic analysis of the five ellipsoidal shells of the same thickness

Two hypotheses were proposed. The first that is the volume of each elliptical layer equal to the volume of the corresponding spherical shell. The second assumption is about the length ratios of the long and short axis of the plutonium shell equal to 2:1.

The volume of the ellipsoid layer is equal to the volume of the responding sphere,

$$V = 4\pi [abc - (a - r)(b - r)(c - r)] / 3 = 4\pi(70^3 - 57.7^3) / 3 ,$$

where  $a$  is  $x$ -axis length of outer surface of plutonium part,  $b$  is  $y$ -axis length of outer surface of plutonium part, and  $c$  is  $z$ -axis length of outer surface of plutonium part. According to the actual situation, make  $b = c$  and  $a/b = 2$ , the following values were obtained:  $a = 108.787$ ,  $b = 54.394$ ,  $c = 54.394$ , and  $r = 12.3$ . The inner ellipse parameter of the plutonium shell material could be also obtained, which were 96.487, 42.094, 42.094, respectively. The structure of computational grid for elliptical case is shown in Fig. 13.

Table 3: The parameters of ellipsoid.

Spherical shell size, mm	Layer				
	Plutonium	Beryllium	Tungsten	Explosive	Steel
Inner short radius	42.094	54.394	74.1952	103.8556	203.1369
Inner long radius	96.487	108.787	128.5882	158.2486	257.5299
Outer short radius	54.394	74.1952	103.8556	203.1369	213.0911
Outer long radius	108.787	128.5882	158.2486	257.5299	267.4841
Thickness	12.3	19.8012	29.6604	99.2813	9.9542

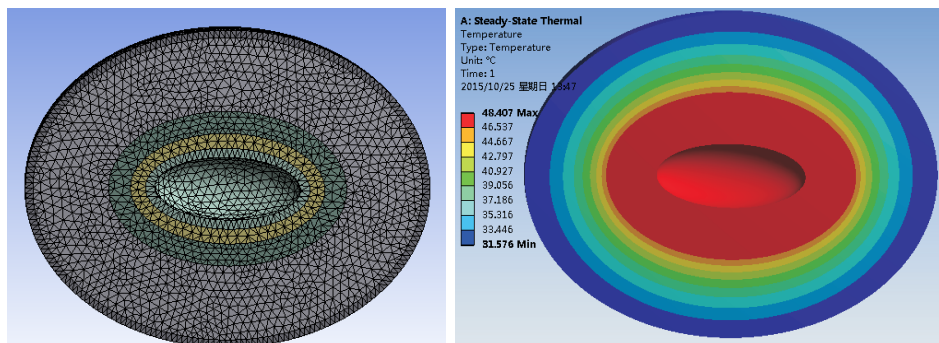


Figure 13: Grid division and temperature stress contour of ellipsoid.

We can see (Fig. 13) that the maximum temperature of the elliptical component is  $48.4107^{\circ}\text{C}$ , thus the highest temperature is lower than that of the spherical component, and is concentrated on the inner surface of the plutonium component.

It can be seen from Figs. 14 and 15 that the heat flux density of the beryllium component is the largest, and the heat flux is  $480.9 \text{ W/m}^2$ . The lowest heat flux density is on the inner surface of the steel component.

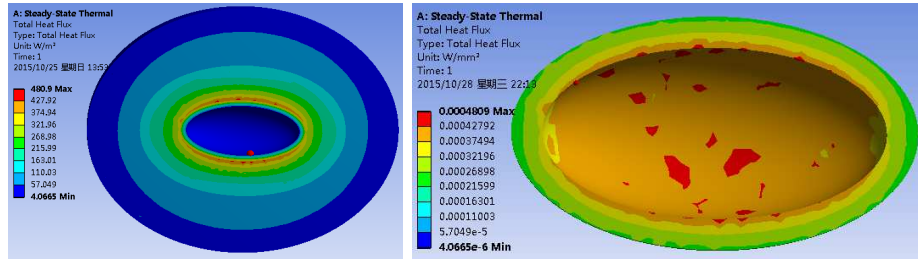


Figure 14: Heat flow density contour. Figure 15: Heat flow density contour of beryllium.

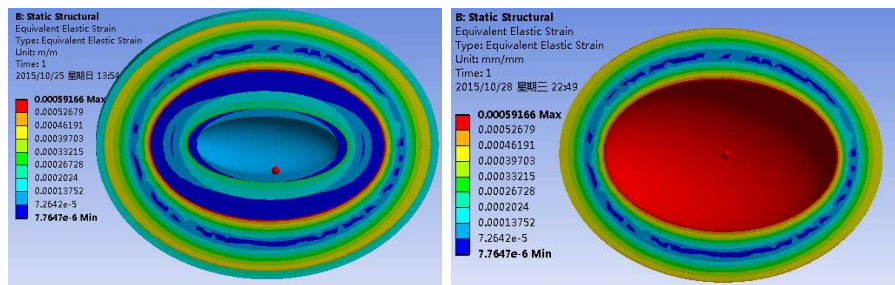


Figure 16: Equivalent elastic strain. Figure 17: Equivalent strain contour of explosive.

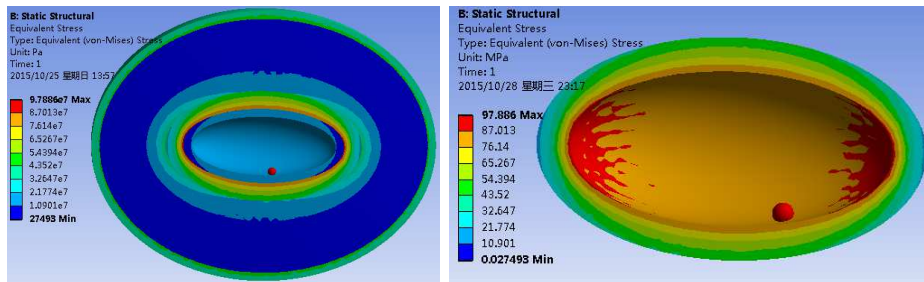


Figure 18: Equivalent stress contour. Figure 19: Stress contour of beryllium component.

From Fig. 16 the elastic strain is on the outer surface of the tungsten component. The largest equivalent strain (see Fig. 17) is on the explosive parts, reaching the  $5.9166 \times 10^{-4}$  mm/mm. The maximum and minimum

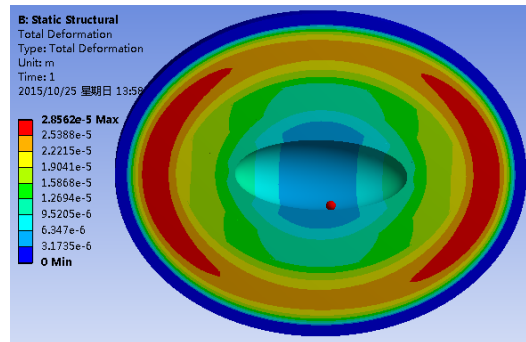


Figure 20: The total deformation contour of ellipsoid.

strain can easily occur at the junction surface of the two part. From the strain of the plutonium component, it can be seen that the lateral strain in the long axis bending part surface is small. From the total strain contour of elliptical part, the strain contour of the ellipse is not uniform along the radial direction. In the curvature surface, the strain changes have been occurred. Figures 18 and 19 show that maximum stress is on the inner surface of beryllium element and the maximum stress is on the inner surface near the long axis. As can be seen from the total deformation contour (Fig. 20), the displacement deformation of the long axis of the explosive part is the largest, and the distribution is symmetric.

From previous research results, the internal temperature of the circular structure is  $48^{\circ}\text{C}$ , and the maximum temperature is  $32^{\circ}\text{C}$ , so the elliptical structure design can effectively reduce the internal temperature. According to the stress and strain contour, the maximum equivalent stress of spherical structure is  $89.65\text{ MPa}$ , while the maximum stress of ellipsoidal structure is  $94.3\text{ MPa}$ . When component section diameter size is infinite, elliptical structure tends to be a spherical structure. therefore, this design is not reasonable.

#### 4 Ratio of long to short axial ellipsoidal shell equal to 2:1

We assume four hypotheses: first, the volume of each layer is equal to the previous two models; second, the ratio of long axis to the short axis is 2:1; third, the ratio of the long axis of the shell thickness to the short axis of

the shell thickness is 2:1; fourth, the length in  $Z$  direction is equal to that of  $Y$  direction. Thus, the ellipsoidal volume can be expressed as:

$$V = 4\pi(a_1b_1^2 - a_2b_2^2)/3 = 4\pi(R_1^3 - R_2^3)/3 ,$$

and  $a_1/b_1 = 2$ ,  $a_2/b_2 = 2$ , where  $R_1$  and  $R_2$  are the long and short axis length, respectively.

Table 4: The calculation results.

Spherical shell size, mm	Layer				
	Plutonium	Beryllium	Tungsten	Explosive	Steel
Inner short radius	45.7965	55.5590	71.4330	95.2441	174.6141
Inner long radius	91.5930	111.1181	142.8661	190.4881	349.2282
Outer short radius	55.5590	71.4330	95.2441	174.6141	182.5511
Outer long radius	111.1181	142.8661	190.4881	349.2282	365.1022
Long diameter thickness	19.5250	31.748	47.622	158.7401	15.874
Short diameter thickness	9.7625	15.874	23.8111	79.37	7.937

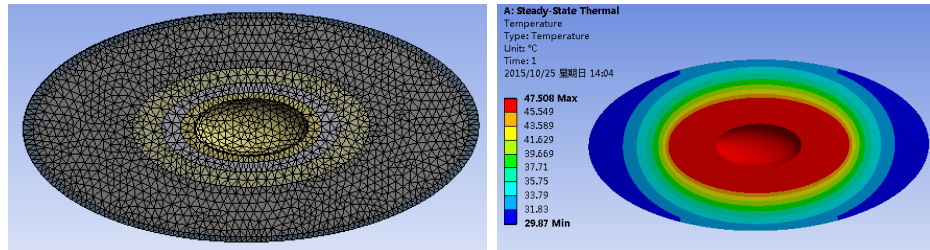


Figure 21: Grid division and temperature stress contour of ellipsoid.

As can be seen from Fig. 21, the maximum temperature occurs in the plutonium, beryllium, tungsten components. The temperature of the explosive components is not uniform, and the temperature gradient near the long axis part is higher than other part, meanwhile the distribution is symmetric. The temperature is lower than the maximum temperature of the previous two models. It shows this model has good cooling performance.

As previous two models, the maximum heat flux density occurs in the internal part of beryllium. It can be seen the maximum heat flux density is in the vicinity of the long axis of beryllium, which is not the same as the thickness of the uniform. In addition, the maximum heat flux is increased up to  $532.5 \text{ W/m}^2$ .

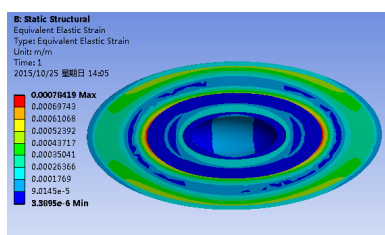


Figure 22: Equivalent elastic strain diagram.

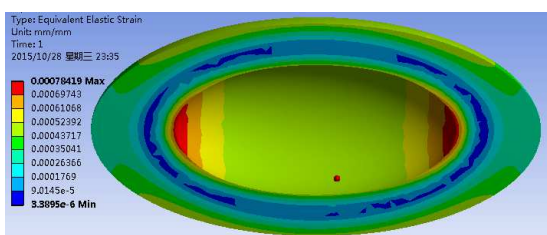


Figure 23: Elastic strain diagram of explosive parts.

The maximum strain can be seen from the strain diagrams (Figs. 22 and 23), which occurs on the inside surface of the long axis direction of the explosive component. This is because the elastic modulus of the explosive component is the smallest, but the Poisson's ratio is the largest. The strain on the outer side of the explosive element is smaller because the steel shell is set to a fixed model, which inhibits the development of the strain of the explosive component.

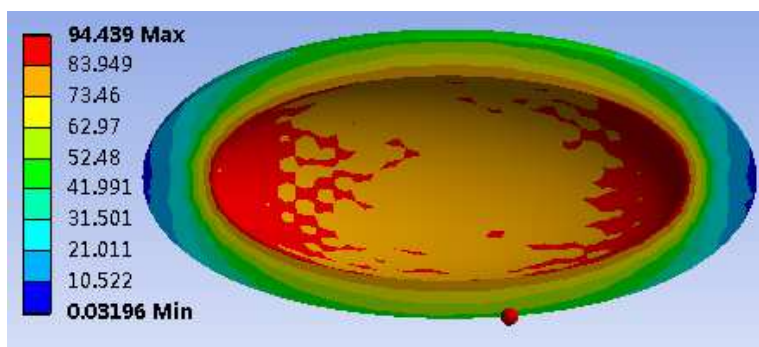


Figure 24: Stress contour of beryllium part.

The maximum stress appears on the inner part of the beryllium element, where its value is equal to  $94.439 \text{ MPa}$ . The maximum stress is lower than

the stress of the spherical shell, which shows that the shape of structure can effectively reduce the maximum stress value.

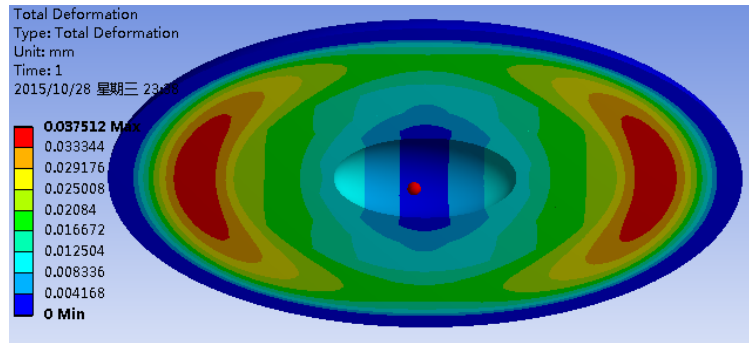


Figure 25: Total deformation of components

From Fig. 25, it can be seen that the maximum deformation of the element is near the long axis of explosive component, because the strain is the largest near the long axis of the explosive, and the thickness of the explosive is the largest. So the maximum deformation occurs on the long axis of the explosive part.

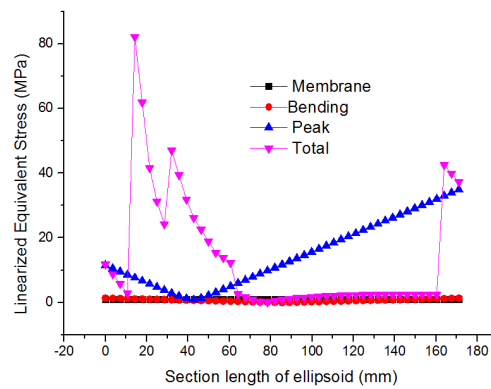


Figure 26: Four kinds of radial linear stress.

As can be seen from Fig. 22, the total equivalent stress occurs at the 13 mm from 1 to 2 point. while from 65 mm to 160 mm, the total equivalent stress is small, but at 170 mm position, the total stress value will suddenly increase. From Fig. 27, the total stress value is very small in the vicinity of explosive components.

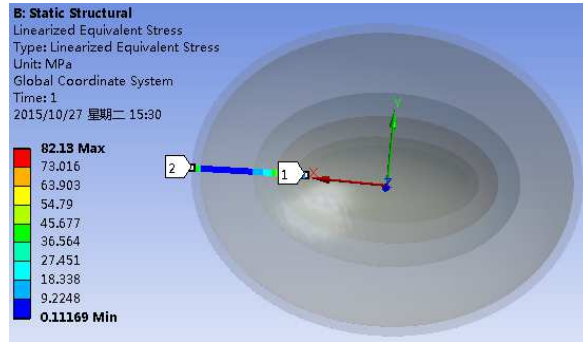


Figure 27: Radial linear stress.

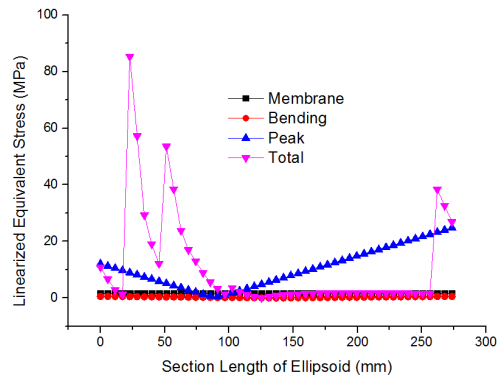


Figure 28: Four kinds of radial linear stress.

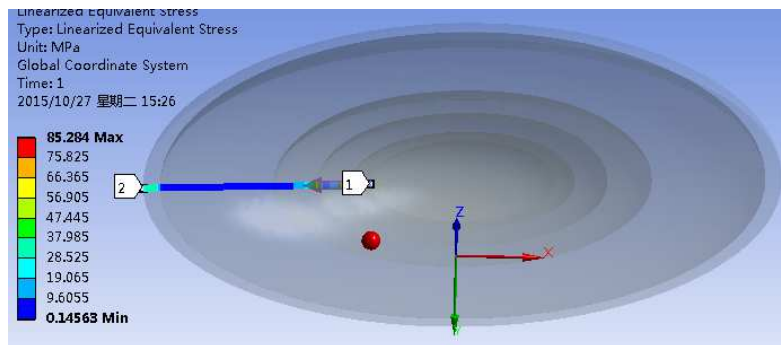


Figure 29: Radial linear stress.

It can be seen in Fig. 28 that curve trend of the radial thickness stress, bending stress, peak and total stress value is very similar to the, linear maximum stress occurs at the 100 mm position. The total stress value at 260 mm is decreased to minimum of 12 mm, which means that the stress of explosive parts is relatively small.

## 5 Conclusion

Through the analysis of three different shapes of complex structure, it can be seen that under the same volume size, the cooling effect of the ellipsoid structure is better than that of the sphere structure. Equivalent stress appears more complex: The equivalent strain of the sphere is higher than that of the equal effect of same thickness of ellipsoid, but the equivalent strain of the sphere is lower than that of ellipsoid of constant value of the long diameter and short diameter ratio. The equivalent stress of the spherical part is lower than that of same thickness of ellipsoid and ellipsoid of constant value of the long diameter and short diameter ratio. The maximum stress and strain of the ellipsoid are located near the long diameter. From linear equivalent strain, the maximum stress strain is near the surface of beryllium parts and the stress of explosive parts is relatively low.

*Received 15 July 2016*

## References

- [1] FETTER S., FROLOV A., MILLER M.: *Detecting nuclear warheads*. J. Sci. Global Security **1**(1990), 3-4, 225–302.
- [2] GAO Z., HE B., ZHAO J.: *Thermal dynamics study of nuclear explosive device*. J. Atomic Energ. Sci. Technol. **44**(2010), 3.
- [3] W88 Nuclear War-head [EB/OL]. (access 4 Dec. 2008)  
<http://wapbaike.baidu.com/view/153510.htm?ref=wise>
- [4] SIEGFRIED S. HECKER: *Plutonium and Its Alloys: From atoms to microstructure*. Los Alamos Science (2000), 290–335.
- [5] ZHAO RU: *Study on temperature field of safe removal of nuclear warhead*. J. Guizhou University(Nature Science) **12**(1995), 1, 51–53.
- [6] BARTOSZEWICZ J., BOGUSZEWSKI L.: *Numerical analysis of the steam flow field in shell and tube heat exchanger*. Arch. Thermodyn. **37**(2016), 2, 107–120.
- [7] HANUSZKIEWICZ-DRAPAŁA M., BURY T., WIDZIEWICZ K.: *Analysis of radiative heat transfer impact in cross-flow tube and fin heat exchangers*. Arch. Thermodyn. **37**(2016), 1, 99–112.



## Influence of thermodynamic mechanism of interfacial adsorption on purifying air-conditioning engineering under intensification of electric field

YUN-YU CHEN\*

First Affiliated Hospital of Wenzhou Medical College, Wenzhou, Zhejiang, 325000, China

**Abstract** As a kind of mass transfer process as well as the basis of separating and purifying mixtures, interfacial adsorption has been widely applied to fields like chemical industry, medical industry and purification engineering in recent years. Influencing factors of interfacial adsorption, in addition to the traditional temperature, intensity of pressure, amount of substance and concentration, also include external fields, such as magnetic field, electric field and electromagnetic field, etc. Starting from the point of thermodynamics and taking the Gibbs adsorption as the model, the combination of energy axiom and the first law of thermodynamics was applied to boundary phase, and thus the theoretical expression for the volume of interface absorption under electric field as well as the mathematical relationship between surface tension and electric field intensity was obtained. In addition, according to the obtained theoretical expression, the volume of interface absorption of ethanol solution under different electric field intensities and concentrations was calculated. Moreover, the mechanism of interfacial adsorption was described from the perspective of thermodynamics and the influence of electric field on interfacial adsorption was explained reasonably, aiming to further discuss the influence of thermodynamic mechanism of interfacial adsorption on purifying air-conditioning engineering under intensification of electric field.

**Keywords:** Interfacial adsorption; Thermodynamics; Gibbs; Purifying air-conditioning engineering; Electric field

---

\*E-mail: chyunyu23@163.com

## 1 Introduction

Purifying air-conditioning engineering is an important issue which guarantees that all parameters in clean operating department are under control. It requires the controlling of air temperature, humidity, dust, bacteria and concentration of hazardous gases, air flow distribution and pressure distribution in different regions of operating rooms and subsidiary rooms, thus to finally create a sterile environment in these rooms and reduce infection probability as well as improve the achievement ratio of operation. Generally, a purifying air-conditioning engineering is composed of air filter, circulating fan, surface air cooler, heating and humidifying units and other basic equipment. It filters the air through low efficient, medium efficient and highly efficient filter units to achieve required cleanness. However, such kind of filter unit has a short service life and high costs; moreover, its filtering effect needs further improvement. With the development of science and technology, interfacial adsorption has been extensively applied in environment and chemical industry production, such as purification of sewage, removal of toxic substances in air and separation or purification of mixtures, etc. [1–3]. Common methods of changing interfacial adsorption include changing temperature, intensity of pressure and types of adsorbent, increasing surface active agent, performing surface modification or applying physical field (such as electric field, magnetic field, etc.). Through these methods, adsorption efficiency can be enhanced or weakened, which can further satisfy the industrial demands [4–6]. However, during the operational process of these methods, such as using active carbon or silica gel to adsorb nitrogen or hydrogen, the adsorption temperature should be controlled at the boiling temperature of nitrogen or hydrogen, so that obvious adsorption effect can be realized because it is difficult for the adsorbents to absorb nitrogen or hydrogen at normal temperature. Moreover, the addition of surface active agent at the interface can affect the purity of products. By comparison, applying electric field can control the amount of adsorbed substances without introducing impurities; moreover, adsorbents can be reused which can save resources as well as costs, thus it is the optimal method which can be applied in chemical industry production [7–9].

Therefore, starting from the point of thermodynamics, this study analyzed the functional mechanism of electric field on interfacial adsorption. Main thermodynamic models used to describe interfacial adsorption at present are Gibbs adsorption model [10–11] and Guggenheim adsorption model [12]. In 1873–1878, American physicist and chemist Gibbs con-

cluded the classical thermodynamics and put forward the Gibbs adsorption isotherm as well as relevant models. In 1920's, a Chinese scientist Fu Ying studied adsorption phenomena and discovered the multilayer adsorption theory of aqueous adsorption; he also put forward methods of using the slope of the initial segment of adsorption isotherms to calculate adsorption standard free energy changes. Both models regard the system as a composition of two bulk phases and one interface. However, in Gibbs adsorption model the interface is regarded as a two-dimensional surface which has area but no volume; while in Guggenheim adsorption model, the interface is regarded as a boundary phase which has area as well as volume. Although the Guggenheim adsorption model is more similar to the actual system, it has a complex computational process and for that reason is not widely applied in engineering. On the contrary, Gibbs adsorption model reflects the relationship among interfacial tension, concentration and adsorbing capacity from the aspect of thermodynamics; it is the most basic formula used to analyze interfacial adsorption and the operation is simple; moreover, its results are close to the reality. Therefore, the Gibbs adsorption model was selected to study the influence of thermodynamic mechanism of interfacial adsorption on purifying air-conditioning engineering under intensification of electric field.

## 2 Definition of interfacial tension

Interfacial tension [13], also known as the surface tension of liquid, is the interfacial tension between liquid and air. Strictly speaking, the surface refers to the interface between liquid or solid and its saturated vapor; but customarily, the interface between liquid (solid) and air is called the surface of liquid (solid). Common interfaces include gas-liquid interface, gas-solid interface, liquid-liquid interface, liquid-solid interface, and solid-solid interface. The interfacial force between a kind of liquid and another kind of immiscible liquid is called the interfacial tension between two liquid phases. The interfacial force between a kind of liquid and a solid is called the interfacial tension between liquid and solid phases. The surface tension of liquid is also called the free energy of the liquid surface [14]. Taking the gas-liquid interface as an example, the attractive force from internal molecules of liquid is greater than that from the internal molecules of gas phase, thus the stress on interface is unbalanced and net attractive force is produced and interfacial tension is formed. The stress on molecules of interface is verti-

cal to the interface and points to the inside of liquid phase. The surface of liquid seems to have an elastic membrane which can allow liquid to be contractive. Interfacial tension is defined as the contraction force per unit length of straight line. Figure 1 shows a metal frame with a movable end where the tip is dipped with soap water. Suppose a force is applied to the end and the tip is pulled slowly rightwards; because the air bubble film on the end has two surfaces, the force applied on the liquid can be described as  $F = 2\gamma l$ , where  $\gamma$  refers to the interfacial tension. The work consumed during the process of liquid molecules moving to the interface is

$$dW_s = Fdx = \gamma dA . \quad (1)$$

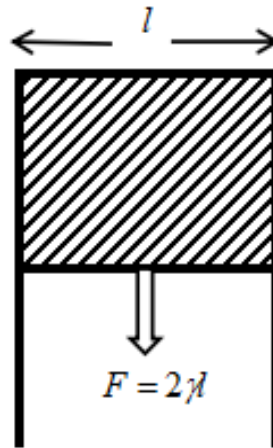


Figure 1: Interfacial tension and surface work.

Equation (1) indicates that, if the interfacial tension is big, then more energy should be consumed to increase the area of interface. From the law of thermodynamics we can know that, at constant temperature and under isopiestic pressure, the interfacial tension is equal to the surface energy of unit area,  $\gamma = \partial G / \partial A_{T,p,n}$ . In the equation,  $G$  refers to the Gibbs free energy and  $A$  is interfacial area, whereas the equation is the thermodynamic definition of interfacial tension. Moreover, all spontaneous thermodynamic states in nature are accompanied by changes of Gibbs free energy. Therefore, the solution interface can turn into a spherical shape automatically. Surface tension varies with temperature. Generally speaking, with the increase of temperature, surface tension decreases, and when the temperature

approaches the critical temperature, the surface tension decreases to zero. Surface tension of binary system is also related to components. Different pure substances have different interfacial tension. If a pure substance is added with a substance which can reduce the interfacial tension of pure solution, adsorption can occur on the interface of solution. The decrease of interfacial tension is the primary cause of interfacial adsorption.

### 3 Gibbs interface

Thickness of the interface layer of two contacted phases only equals to several molecular diameters, and only few molecules are in this region. When the specific value between superficial area and volume is high, the influence of surface effect on system property is significant. The property of interface layer changes from typical  $\alpha$  phase to typical  $\beta$  phase (Fig. 2), which is uneven. The interfacial behavior analysis of this study on a single molecule tends to develop to general analysis reflecting the interface. Due to changes of the interaction between molecules, the average energy of molecules in interface zone is different from that of the molecules in a phase. The  $\sigma dA$  refers to the work needed for the increase of interfacial area and  $\sigma$  refers to interfacial tension. Residual force fields are formed due to the asymmetric stress of molecules in superficial layer, and these unbalanced force fields can have absorption on surrounding mediums, thus the surface can adsorb substances that can reduce the surface energy. The adsorption which can make the surface concentration be bigger than the internal concentration of liquid is called the positive adsorption which can be generated by molecules migrating from the main phase to the interface to reduce interfacial energy or surface tension. In order to quantitatively describe the surface adsorption of liquid, the adsorbing capacity is introduced to represent the adsorption degree [15].

Concentration of substances on the adsorption surface changes continuously without a clear interface. In Gibbs thermodynamic model of adsorption, the interface is considered as a two-dimensional surface phase without thickness and the volume is negligible while other thermodynamic quantities are not zero. As shown in Fig. 2, the region above line A refers to the pure  $\alpha$  phase and the region below line B refers to pure  $\beta$  phase. The area between A and B is the interface region where components and properties change instantaneously. According to the concept of surface phase of Gibbs, a two-dimensional geometric surface S with no thickness between

A and B is selected, which is called the surface phase  $\sigma$ . The symbol A refers to the area of surface phase and components of surface phase are described by surface excess amount  $n_i^\sigma$  ( $i = 1, 2$ ). The  $n_i^\sigma$  is obtained by the actual mole number of  $i$  component in AB region subtracting the mole number of  $i$  component in phase boundary region AB when imaginary  $\alpha$  and  $\beta$  phases evenly extend to the surface phase S according to bulk phase. Surface excess amount can be positive, negative or zero, which is related to the position of imaginary interface S.

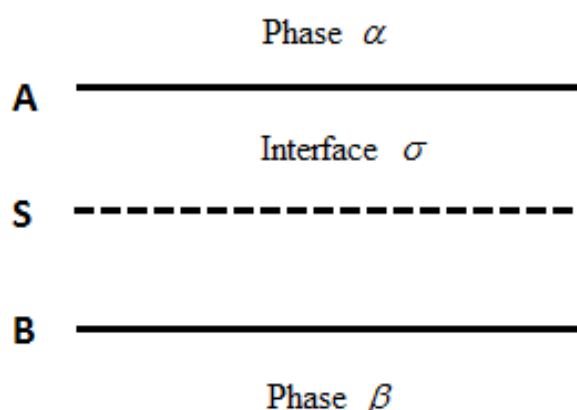


Figure 2: Illustration of the interface between two phases of Gibbs model.

#### 4 Effect of electric fields on thermodynamics mechanism of adsorption

The adsorption thermodynamic model mainly refers to adsorption isothermal equation, which is used to describe the adsorption isotherm. The so called adsorption isotherm refers to the relation curve between equilibrium absorption capacity,  $\Gamma_e$ , of adsorbate on adsorbent and the equilibrium concentration,  $C_e$ , of adsorbate in liquid phase. The widely applied adsorption isothermal equations are Freundlich and Langmuir equations, in which the Freundlich equation is an empirical equation while the Langmuir equation is established on the basis of thermodynamic equilibrium theory.

Different factors can cause different changes of interface compositions in the interface layer. For example, substances transfer from the bulk phase to the interface or substances in the interface phase enter inside the bulk

phase. Therefore, the concentration in interface can increase as well as decrease. As shown in Fig. 3, the movement of these molecules explains the interfacial adsorption. Generally speaking, adsorption is the increase of substances in the interface phase; the amount of substances adsorbed on interface is described by surface excessive amount,  $\Gamma$ , i.e., the amount of adsorbed substances in unit area. When the temperature stays the same, the functional relationship between the surface excessive amount and intensity of pressure  $\Gamma = pT$  or the functional relationship between surface excessive amount and concentration  $\Gamma = cT$  is called adsorption isotherm (where  $p$  – pressure,  $c$  – condensation,  $T$  – temperature). Adsorption isothermal equations contribute to a better understanding of interfacial adsorption as well as the prediction of interfacial adsorption amount. Besides, the application of adsorption isotherms is extensive. For example, properties of interface and pores can be studied according to adsorption isotherms and specific surface area and pore size distribution can be calculated, etc. The adsorption caused by physical interaction is called the physical adsorption; a large number of adsorption isotherms are obtained through experiments according to physical conditions.

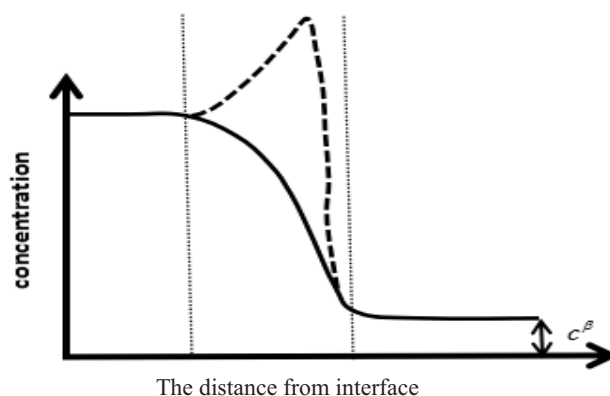


Figure 3: Change of concentration at the interface.

In general, the existence of interface can affect the thermodynamic parameters and properties of the whole system. To consider the thermodynamic properties of a system which contains an interface, the system is divided into three parts: two bulk phases whose volume is  $V^\alpha$  and  $V^\beta$ , respectively, and an interface  $\sigma$ . In Gibbs adsorption model, two bulk phases are separated by a two-dimensional surface without thickness, i.e., Gibbs interface.

In Gibbs adsorption model, except volume, all other extensive quantities, such as internal energy,  $U$ , entropy,  $S$ , and the amount of substance,  $n$ , can be described as three parts, which form two bulk phases and one interface;

$$V = V^\alpha + V^\beta, \quad (2)$$

$$U = U^\alpha + U^\beta + U^\sigma, \quad (3)$$

$$S = S^\alpha + S^\beta + S^\sigma, \quad (4)$$

$$n_i = n_i^\alpha + n_i^\beta + n_i^\sigma. \quad (5)$$

Assume  $u^\alpha$ , and  $u^\beta$  are internal energies of the unit volume of two bulk phases, respectively, and  $c_i^\alpha$ , and  $c_i^\beta$  are concentrations of component,  $i$ , in two bulk phases, respectively, then the total amount of internal energies and substances of interface phase can be expressed as  $U^\sigma = U - u^\alpha V^\alpha - u^\beta V^\beta$  and  $n_i^\sigma = n_i - c_i^\alpha V^\alpha - c_i^\beta V^\beta$ . Surface excessive amount is defined as

$$\Gamma = \frac{n_i^\sigma}{A}. \quad (6)$$

#### 4.1 Traditional Gibbs adsorption isothermal equation

Under equilibrium state, the fundamental equation of thermodynamics when the system has a surface energy is expressed as  $dU = TdS - pdV + \sum_i \mu_i dn_i + \gamma dA$ , where all amounts in the equation are the total amount in the actual system. In Gibbs model, the internal energy of  $\alpha$  phase and  $\beta$  phase is  $dU^\alpha = TdS^\alpha - pdV^\alpha + \sum_i \mu_i dn_i^\alpha$  and  $dU^\beta = TdS^\beta - pdV^\beta + \sum_i \mu_i dn_i^\beta$ , respectively, and on the basis of Eqs. (2), (4) and (5), can be deduced

$$dU^\alpha = TdS^\alpha + \sum_i \mu_i dn_i^\alpha + \gamma dA. \quad (7)$$

The Gibbs function in imaginary surface phase of Gibbs model is defined as  $G^\sigma = U^\sigma - TS^\sigma - \sigma A$  and the combination of its perfect differential and can obtain the differential equation  $dG^\sigma = -S^\sigma dT + \sum_i \mu_i dn_i^\sigma - Ad\sigma$ . On the basis of  $G = \sum_i \mu_i n_i$ , the Gibbs-Duhem function in  $\sigma$  phase is

$$S^\sigma dT + Ad\sigma + \sum_i n_i^\sigma d\mu_i = 0. \quad (8)$$

Under the same temperature and pressure, the following equation can be obtained

$$d\sigma = - \sum_i \left( \frac{n_i^\sigma}{A} \right) d\mu_i^\sigma = - \sum_i \Gamma_i d\mu_i^\sigma, \quad (9)$$

where  $\frac{n_i^s}{A}$  refers to the surface excessive amount  $\Gamma_i$ , and the equation is the fundamental form of Gibbs adsorption equation.

The value of surface excessive amount is related to the position selection of interface S, and for any appointed component (such as solvent), there is one and only one position obeying  $n_1^s = 0$ . Taking two components as an example and selecting S to make  $\Gamma_1 = 0$ , then the above equation can be written as

$$d\sigma = -\Gamma_2 d\mu_2 \quad \text{or} \quad \Gamma_2 = - \left( \frac{\partial \sigma}{\partial \mu_2} \right)_T . \quad (10)$$

This is the expression of Gibbs adsorption equation in two components. According to the above analyses we discover that, the Gibbs adsorption isothermal equation can be obtained by the combination of Gibbs-Duhem function and the analysis methods of Gibbs surface phase, and the Gibbs adsorption isothermal equation under the effect of external field can be obtained by the combination of Gibbs-Duhem function and analysis methods of Gibbs surface phase under the external field effect.

## 4.2 Gibbs adsorption isothermal equation under the effect of electric field

On the basis of ideal Gibbs adsorption model theory and according to the energy axiom, the differential of any kind of energy can be expressed as the product of a basic intensive quantity,  $X$ , and a conjugated basic extensive quantity,  $x$ , differential, i.e.,  $dW = Xdx$ , where,  $X$ , represents a kind of field quantity. The expression can also be expressed by work because the latter can transmit or change the internal energy of the whole system. For example, the analogy of surface work,  $dW = \gamma dA$ , can be the surface energy. Under the effect of electric field, substances can be polarized and the polarization degree can be represented by polarization energy. For the substance with even phases, the expression of its polarization energy under the effect of electric field can be expressed as

$$dW_c = EdP' , \quad (11)$$

where  $E$  refers to the applied electric field intensity and  $P'$  is the total electric dipole moment of substances.

According to the first law of thermodynamics, changes of internal energy of the system are simply caused by working or thermal transmission. Therefore, except thermal transmission, volume work, particle changes, and

surface energy – when the applied electric field acts on a three-phase system, the total internal energy of the system can be generalized as following according to the first law of thermodynamics and energy axiom [16]:

$$dU = TdS - p^\alpha dV^\alpha - p^\beta dV^\beta + \sum \mu_i dn_i + \gamma dA + EdP' . \quad (12)$$

For plane interface,  $p^\alpha = p^\beta$ , thus the above equation can be transformed as

$$dU = TdS - pdV + \sum \mu_i dn_i + \gamma dA + EdP' . \quad (13)$$

As for the intensive quantity, the chemical potential and electric field intensity of, such as temperature and one component, are uniform under the equilibrium state. Applying electric field in two-phase system, their internal energy can be expressed as

$$dU^\alpha = TdS^\alpha - pdV^\alpha + \sum \mu_i dn_i^\alpha + EdP'^\alpha , \quad (14)$$

$$dU^\beta = TdS^\beta - pdV^\beta + \sum \mu_i dn_i^\beta + EdP'^\beta . \quad (15)$$

Combining with the function  $P' = P'^\alpha + P'^\beta + P'^\sigma$ ,  $V = V^\alpha + V^\beta$ ,  $U = U^\alpha + U^\beta + U^\sigma$ ,  $S = S^\alpha + S^\beta + S^\sigma$  and  $n_i = n_i^\alpha + n_i^\beta + n_i^\sigma$ , the expression of internal energy of interface phase is

$$dU^\sigma = TdS^\sigma + \sum \mu_i dn_i + \gamma dA + EdP'^\sigma . \quad (16)$$

The above equation indicates that, the interface phase can be taken as a normal system and described directly using fundamental thermodynamic relation, except that the volume is neglected in Gibbs adsorption model. The Gibbs adsorption function describes the relationship between concentration changes and interfacial tension changes of a component in the interface phase. Initially, Gibbs deduces the change relation of interfacial tension and concentration of component through thermodynamic method, and on the basis of this Guggenheim and Adam [17] improved the method and put forward a simpler and more reliable method. Gibbs adsorption equation is the third basic equation of interfacial chemistry. For a multicomponent system, if its temperature, chemical potential, interfacial tension, and electric field intensity remain the same and its internal energy, entropy, superficial area and intensity of polarization increase from zero to a certain value, then the expression of total internal energy of interface phase is

$$U^\sigma = TS^\sigma + \sum \mu_i n_i^\sigma + \gamma A + EP'^\sigma . \quad (17)$$

The above equation is a generalized equation and through differential of the equation, the following function can be obtained:

$$dU^\sigma = TdS^\sigma + S^\sigma dT + \sum \mu_i dn_i^\sigma + \sum n_i d\mu_i^\sigma + \gamma dA + Ad\gamma + EdP'^\sigma + P'^\sigma dE. \quad (18)$$

Combining function (16) and (18), the Gibbs-Duhem function which has the interface phase under the influence of electric field can be:

$$S^\sigma dT + \sum n_i^\sigma d\mu_i + Ad\gamma + P'^\sigma dE = 0. \quad (19)$$

For a multicomponent system, the total electric dipole moment can be expressed as  $P' = \sum n_i^\sigma V_{m,i} P_i$ , where  $V_{m,i}$  refers to the partial molar volume, and  $P_i$  is the dipole moment of unit volume of  $i$  substance, which is also called the intensity of polarization, and its relation with electric field intensity is  $P_i = \varepsilon_0(\varepsilon_{r,i} - 1)E$ . Therefore, the polarization energy of dielectric medium in the system under the effect of electric field can be expressed as  $P' dE = \sum n_i^\sigma d \left[ \frac{1}{2} \varepsilon_0(\varepsilon_{r,i} - 1)E^2 V_{m,i} \right]$ , where  $\varepsilon_0$  and  $\varepsilon_{r,i}$  are dielectric constant and relative dielectric constant in vacuum respectively. The equation is then substituted into Eq. (19) and under the condition of steady temperature the generalized Gibbs-Duhem under the effect of electric field can be simplified to:

$$\sum n_i^\sigma d\mu_i + Ad\gamma + \sum n_i^\sigma d \left[ \frac{1}{2} \varepsilon_0(\varepsilon_{r,i} - 1)E^2 V_{m,i} \right] = 0. \quad (20)$$

The above equation indicates that the interfacial adsorption not only includes the adsorption caused by changes of interfacial area, but also includes the effect of external electric field on adsorption. Combining Eq. (21) and definition of surface adsorption capacity, the Gibbs adsorption equation under the effect of electric field can be obtained:

$$d\gamma = - \sum \Gamma_i d \left[ \mu_i + \frac{1}{2} \varepsilon_0(\varepsilon_{r,i} - 1)E^2 V_{m,i} \right]. \quad (21)$$

The above equation is the expression of Gibbs adsorption isothermal equation under the effect of electric field, which indicates the relationship between interfacial tension and adsorption capacity and electric field intensity [18]. When there is no extra electric field, the equation can be simplified as  $d\gamma = -\Gamma_i d\mu_i$ , which is the traditional Gibbs adsorption isothermal equation.

## 5 Application of Gibbs adsorption isothermal equation in two-component solution under the effect of electric field

In order to better understand the Gibbs adsorption isothermal equation under the effect of electric field, the simplest two components are taken as an example, which are solvent 1 and solute 2, respectively. Because the definition of surface adsorption capacity is related to the position of Gibbs interface, generally speaking, the position where the adsorption capacity of solvent 1 is zero [19], i.e.,  $\Gamma_1 = 0$  is defined as the Gibbs interface, then the Gibbs adsorption function of two components is

$$d\gamma = -\Gamma_2^1 d\left[\mu_2 + \frac{1}{2}\varepsilon_0(\varepsilon_{r,2} - 1)E^2 V_{m,2}\right]. \quad (22)$$

According to the equation, the interfacial excessive amount of component 2 at Gibbs interface is

$$\Gamma_2^1 = -\left[\left(\frac{d\gamma}{d\mu^2}\right)^{-1} + \left(\frac{1}{1/2\varepsilon_0(\varepsilon_{r,2} - 1)V_{m,2}} \frac{d\gamma}{dE^2}\right)^{-1}\right]^{-1}. \quad (23)$$

The chemical potential expression of ideal solution is  $\mu_2 = \mu_2^0 + RT \ln(c_2/c_0)$ , where  $c_0$  refers to the concentration of ideal solution and  $R, T$  are the gas constant and absolute temperature, respectively. At constant temperature, the chemical potential is substituted into the above equation and the following equation can be obtained:

$$\Gamma_2^1 = -\left[\left(\frac{1}{RT} \frac{d\gamma}{d \ln c_2}\right)^{-1} + \left(\frac{1}{1/2\varepsilon_0(\varepsilon_{r,2} - 1)V_{m,2}} \frac{d\gamma}{dE^2}\right)^{-1}\right]^{-1}. \quad (24)$$

If there is no extra electric field, then the second item of Eq. (24) is zero and the adsorption equation turns into the classic Gibbs adsorption equation  $\Gamma_2^1 = -\frac{1}{RT} \frac{d\gamma}{d \ln c_2}$ . If solvent is increased and the surface energy is decreased, then the surface tension decreases with the increase of concentration, i.e.,  $d\gamma/dc_2 < 0$ ; and the adsorption capacity is positive,  $\Gamma_2^1 < 0$ , i.e., positive adsorption and substances gather at interface. Otherwise, if the surface tension increases with the increase of concentration,  $d\gamma/dc_2 < 0$ , then the adsorption capacity is negative,  $\Gamma_2^1 < 0$ , i.e., negative adsorption and the

adsorption capacity of substances at the interface is negative. If the external field is applied, then the second item of Eq. (22) is not zero, thus the electric field can have an effect on the adsorption capacity of interface. Under certain concentration, according to former conclusions, the interfacial tension decreases with the increase of electric field intensity,  $d\gamma/dc_2 < 0$ , then  $\Gamma_2^{1E} < \Gamma_2^1$ , indicating that the application of electric field has an effect on interfacial adsorption, i.e., the interfacial adsorption capacity of solution decreases.

The purifying air-conditioning engineering discussed in this study can be applied to sterile laboratories, food clean workshops and hospital operating rooms. Electric field application has an impact on interfacial adsorption, i.e., the volume of interface absorption of solution decreases. Such conclusion can be applied to the purifying air-conditioning engineering, indicating that the thermodynamic mechanism of interfacial adsorption has an important effect on purifying air-conditioning engineering under intensification of electric field.

## 6 Conclusion

Gibbs model is the most classic model using thermodynamic methods for simplified treatment of interfacial phenomenon and the position selection of Gibbs interface determines the complexity of adsorption processing.

Therefore, firstly, this study introduces the selection of Gibbs interface, Gibbs adsorption model and traditional Gibbs adsorption equation. Then using the fundamental thermodynamic relation and energy axiom, the Gibbs adsorption isothermal equation under the effect of electric field is deduced, i.e., from the aspect of thermodynamics, the relationships between interfacial adsorption capacity and interfacial tension, concentration and electric field intensity are deduced. The obtained conclusions lay a theoretical foundation for the interfacial adsorption under the effect of electric field as well as a good understanding of the relationship among these four properties.

This study takes the simplest two components as an example to analyze the relationships among interfacial adsorption capacity and interfacial tension, concentration and electric field intensity at the same temperature and under the same pressure, and qualitatively analyzes the effect of interfacial tension and electric field intensity on interfacial adsorption respectively. In addition, it comes to a conclusion that, after the application of electric field,

the interfacial adsorption capacity of solution decreases.

Received 30 March 2016

## References

- [1] XU H., PERUMAL S. X., DU N. *et al.*: *Interfacial adsorption of antifreeze proteins: a neutron reflection study*. *Biophysical J.* **94**(2008), 1, 4405–4413.
- [2] DAN A., WÜSTNECK R., KRÄGEL J. *et al.*: *Interfacial adsorption and rheological behavior of  $\beta$ -casein at the water/hexane interface at different pH*. *Food Hydrocolloid.* **34**(2014), 193–201.
- [3] KOBYLECKI R.: *Carbonization of biomass – an efficient tool to decrease the emission of CO<sub>2</sub>*. *Microsc. Res. Techniq.* **34**(2013), 3, 185–195.
- [4] SARAF S., NEAL C. J., DAS S. *et al.*: *Understanding the adsorption interface of polyelectrolyte coating on redox active nanoparticles using soft particle electrokinetics and its biological activity*. *ACS Appl. Mater. Interfaces*, **6**(2014), 8, 5472–5482.
- [5] LIPING W., RIEMSDIJK W.H.V., TIJISSE H.: *Humic nanoparticles at the oxide-water interface: interactions with phosphate ion adsorption*. *Environ. Sci. Technol.* **42**(2008), 23, 8747–52.
- [6] ONORATO R.M., OTTEN D.E., SAYKALLY R.J.: *Adsorption of thiocyanate ions to the dodecanol/water interface characterized by UV second harmonic generation*. In: *Proc. Nat. Aca. Sci. USA PNAS* **106**(2009), 36, 15176–15180.
- [7] LI H., LI R., ZHU H.L. *et al.*: *Influence of electrostatic field from soil particle surfaces on ion adsorption-diffusion*. *Soil Sci. Soc. Am. J.* **74**(2010), 4, 1129–1138.
- [8] EFTEKHARIBAFROOEI A., BORGUET E.: *Effect of electric fields on the ultrafast vibrational relaxation of water at a charged solid-liquid interface as probed by vibrational sum frequency generation*. *J. Phys. Chem. Lett.* **2**(2011), 12, 1353–1358.
- [9] ENGELHARDT K., RUMPEL A., WALTER J. *et al.*: *Protein adsorption at the electrified air-water interface: Implications on foam stability*. *Langmuir* **28**(2012), 20, 7780–7.
- [10] OSAMU S., HIROMICHI N., YOSHIKIYO M.: *New adsorption model – theory, phenomena and new concept*. *J. Oleo Sci.* **64**(2015), 1, 1–8.
- [11] PERRIER L, PIJAUDIER-CABOT G, GRÉGOIRE D.: *Poromechanics of adsorption-induced swelling in microporous materials: a new poromechanical model taking into account strain effects on adsorption*. *Continuum Mech. Therm.* **27**(2014), 1–2, 195–209.
- [12] ALTZIBAR J.M., TAMAYO RIA I., CASTRO V.D. *et al.*: *Extension of the asymptotically-correct approximation to Fowler-Guggenheim adsorption*. *Clin. Exp. Allergy* **45**(2014), 6, 1099–1108.
- [13] SCHOOT P.V.D.: *Remarks on the interfacial tension in colloidal systems*. *Russ. Geol.d Geophys.* **56**(2015), 3, 446–465.

- 
- [14] BROWN P. S., BHUSHAN B.: *Determination of the interfacial tension between oil–steam and oil–air at elevated temperatures*. *Apl Mater.* **30**(2016), 1, 15568–15573.
- [15] HODGE I.M.: *Application of the thermorheologically complex nonlinear Adam-Gibbs model for the glass transition to molecular motion in hydrated proteins*. *Biophys. J.* **91**(2006), 3, 993–5.
- [16] TERPIŁOWSKI J., PIOTROWSKA-WORONIAK J., ROMANOWSKA J.: *A study of thermal diffusivity of carbon-epoxy and glass-epoxy composites using the modified pulse method*. *Arch. Thermodyn.* **35**(2014), 3, 117–128.
- [17] RADKE C.J.: *Gibbs adsorption equation for planar fluid–fluid interfaces: Invariant formalism*. *Adv Colloid Interfac.* **222**(2015), 600–614.
- [18] ZHANG J, DING T, ZHANG Z. *et al.*: *Enhanced adsorption of trivalent arsenic from water by functionalized diatom silica shells*. *Plos One* **10**(2015), 4.
- [19] LIU F., TANG C.H.: *Improvement of emulsification and interfacial adsorption by electrostatic screening*. *Food Hydrocolloid.* **60**(2016), 620–630.



## Study on transport packages used for food freshness preservation based on thermal analysis

YING YU\*

Hunan Vocational College of Railway Technology, 171, Jianshe Middle Road,  
Zhuzhou, Hunan, 412000, China

**Abstract** In recent time, as the Chinese consumption level increases, the consumption quantity of high-value fruits, vegetables and seafood products have been increasing year by year. As a consequence, the traffic volume of refrigerated products also increases yearly and the popularization degree of the cold-chain transportation enhances. A low-temperature environment should be guaranteed during transportation, thus there is about 40% of diesel oil should be consumed by the refrigerating system and the cold-chain transportation becomes very costly. This study aimed to explore methods that could reduce the cost of transport packages of refrigerated products. On the basis of the heat transfer theory and the fluid mechanics theory, the heat exchanging process of corrugated cases during the operation of refrigerating system was analyzed, the heat transfer process of corrugated cases and refrigerator van was theoretically analyzed and the heat balance equation of corrugated cases was constructed.

**Keywords:** Heat transfer theory; Logistics transportation; Ansys Flotran; Temperature distribution

### 1 Introduction

China is a country with a large production of agricultural products, where the trade volume of agricultural products in China is increasing gradually year by year. Fresh food takes a great proportion of demand in market; however, due to the neglect of transport caused by excessive emphasis on

---

\*E-mail: yingyu23y@sina.com

production, the development of fresh food transport is limited severely [1–3]. Continually increasing consumption of high-value fruits, vegetables and seafood products has resulted in the increase of traffic volume of refrigerated products. The increase of cold-chain demand has been particularly outstanding in the fields of meat products, fruits and vegetables, dairy products and medicine [4–6]. Temperature control of products is the key parameter during the whole process of cold-chain transportation and any phenomenon of out-of-control temperature can lead to enormous losses [7–9]. Thus, the temperature should be controlled precisely to guarantee the quality of products during transportation. Therefore, changes and field distribution of temperatures of the interior carriage and packing cases of products during transportation should be analyzed. The final results have great guidance values to the design of transport packages of products.

Lots of research results of the temperature field of refrigerated products have been obtained in other countries. Initial researches were mostly performed by experiments. Researchers in country-region Italy once carried out experiments based on the railway, and various kinds of standardizing components were used to simulate product models, thus to analyze the temperature distribution of interior packages. As the computer technology develops rapidly at present, the temperature field has been studied using numerical simulation. Quarini and Foster studied the heat exchange between the cold air of freezer and the outside, and the obtained results were of great value to the design of energy-efficient refrigerators. In this study the commercial Ansys Flotran software was used to simulate temperature changes of products inside the refrigerator van, and the temperature field and temperature changes of the whole van were obtained. At last, obtained results were concluded, and improved cryogenic temperature and refrigerating method that could reduce energy consumption and save costs were planned, thus to obtain the optimal transportation program.

## 2 Model of phase change heat transfer

### 2.1 Basic theories of heat transfer theory

Fourier law is a fundamental law of heat transfer theory [10–12], which can be described as follow: in phenomena of heat conduction, suppose the heat quantity that passes through the interface in unit time is in direct proportion to the change rate of temperature in vertical direction of the interface as well as to the area of the interface, then the direction of heat transfer

is contrary to the direction of the temperature increase [13]. According to the Fourier law, the quantity of heat conduction,  $\Phi$ , that passes through one position in unit time should be in direct proportion to the change rate of temperature as well as the area of the position:

$$\Phi = -\lambda A \frac{dt}{dx} = \lambda A \frac{\Delta t}{\delta}, \quad (1)$$

hence the heat flux that transfers along the  $x$  direction is

$$q = \frac{\Phi}{A} = \lambda \frac{\Delta t}{\delta}. \quad (2)$$

In above equations  $\Phi$  refers to the rate of heat,  $\lambda$  refers to the thermal conductivity coefficient,  $t$  means temperature,  $x$  is the coordinate on heat conduction surface,  $A$  is heat conduction area,  $\Delta t$  is the temperature difference of surface, and  $dt/dx$  is the temperature gradient in the direction of  $x$ , i.e., the change rate of temperature (the negative sign in Eq.(1) means that, the heat transfer direction is contrary to the direction of the temperature gradient),  $\delta$  is the thickness of surface.

### 3 Thermal analysis

Using the finite element software for numerical thermal analysis is to apply the principle of conservation of energy to construct the heat balance equation and obtain the temperature of each node through finite element calculation; other thermal physics parameters of the material can be deduced according to temperatures of nodes. Steady-state analysis and transient analysis can be performed.

#### 3.1 Thermal analysis governing equation

The governing differential equation of heat conduction:

$$\frac{\partial}{\partial x} \left( k_{xx} \frac{\partial T}{\partial x} \right) + \frac{\partial}{\partial y} \left( k_{yy} \frac{\partial T}{\partial y} \right) + \frac{\partial}{\partial z} \left( k_{zz} \frac{\partial T}{\partial z} \right) + q = \rho c \frac{dT}{dt}, \quad (3)$$

$$\frac{dT}{dt} = \frac{\partial T}{\partial t} + V_x \frac{\partial T}{\partial x} + V_y \frac{\partial T}{\partial y} + V_z \frac{\partial T}{\partial z}, \quad (4)$$

where  $T$  is the temperature,  $q$  is the heat flux,  $\rho$  is the density,  $c$  is the specific heat,  $k_{xx}$ ,  $k_{yy}$ ,  $k_{zz}$  and,  $V_x$ ,  $V_y$ ,  $V_z$  refer to velocity components

in  $x, y, z$  directions respectively and conduction rates, respectively  $x, y, z$ , are the Cartesian coordinates, and  $t$  denotes time. Equation (3) can be transformed into equivalent integral form

$$\int_{vol} \left[ \rho c \delta_T \left( \frac{\partial T}{\partial t} + \{v\}^\top \{L\}^\top \right) + \{L\}^\top \delta_T \left( \{D\} \{L\}^\top \right) \right] d(vol) =$$

$$= \int_{S_2} \delta_T q^* d(S_2) + \int_{S_3} \delta_T h_f (T_B - T) d(S_3) + \int_{vol} \delta_T q d(vol), \quad (5)$$

where  $vol$  refers to the element volume,  $\{L\}^\top = \left[ \frac{\partial}{\partial x} \frac{\partial}{\partial y} \frac{\partial}{\partial z} \right]$ ,  $q$  is the heat generation of unit volume,  $h_f$  refers to convective heat transfer coefficient,  $T_B$  is the temperature of fluid,  $\delta_T$  is the dummy variable of temperature,  $S_2$  and  $S_3$  are the application areas of heat flux and convection, respectively, superscript  $\top$  denotes transpose operation.

Polynomial of unknown temperatures can be written as

$$T = \{N\}^\top \{T_e\}, \quad (6)$$

where  $\{T_e\}$  refers to temperature vectors of element nodes and  $\{N\}^\top$  is the shape function of element.

Heat flux and temperature gradient of each element can be calculated according to temperatures of element nodes

$$\{a\} = \{L\}^\top = [B] \{T_e\}, \quad (7)$$

where  $\{a\}$  refers to the thermal gradient vector and  $[B] = \{L\}^\top [N]$ .

Heat flux can be calculated according to equation

$$\{q\} = (D) \{L\}^\top = (D) [B] \{T_e\} = (D) \{a\}, \quad (8)$$

where  $(D)$  refers to the property matrix of heat conduction of the material.

$$\int_{vol} \rho c \{N\}^\top \{N\} d(vol) \{T_e\} + \int_{vol} \rho c \{N\}^\top \{v\}^\top [B] d(vol) \{T_e\}$$

$$+ \int_{vol} (B)^\top (D) (B) d(vol) \{T_e\} = \int_{S_2} \{N\} q^* d(S_2) + \int_{S_3} T_B h_f \{N\} d(S_3)$$

$$- \int_{S_2} h_j \{N\}^\top \{N\} \{T_e\} d(S_2) + \int_{vol} q d(vol). \quad (9)$$

Matrix form of the above equation is

$$(C)\{T\} + ((K^m) + (K^d) + (K^c))\{T\} = (Q^f) + (Q^c) + (Q^g), \quad (10)$$

where:

$$(K^m) = \int_{vol} \rho c \{N\}^T \{v\}^T [B] d(vol),$$

$$(K^d) = \int_{vol} (B)^T (D) (B) d(vol),$$

$$(K^c) = \int_{s_2} h_f \{N\}^T \{N\} d(S_3),$$

$$(Q^f) = \int_{s_2} \{N\} q^* d(S_2),$$

$$(Q^c) = \int_{S_2} T_B h_f \{N\} d(S_3),$$

$$(Q^g) = \int_{vol} q d(vol),$$

The general equation matrix can be expressed as

$$(C)\{T\} + (K)\{T\} = \{Q\}, \quad (11)$$

where:

$$(C) = \sum_{i=1}^n (C)_i,$$

$$(K) = \sum_{i=1}^n (K^{m,d,c})_i,$$

$$(Q) = \sum_{i=1}^n \{Q^{f,c,g}\}_i + \{Q_0\},$$

here  $n$  refers to the number of elements and  $\{Q_0\}$  refers to the rate of heat flow applied to nodes.

### 3.2 Processing of phase change problems using the finite element software

A kind of large scale and general finite element analysis software – that integrates electric field, magnetic field, sound field, structure, load, temperature field and fluid analysis – Ansys [14–16] has been used.

The used finite element analysis software considers the latent heat of phase-change materials through defining their enthalpy value, which changes along with the change of temperature. Changes of enthalpy value can be described by the function expression of density,  $\rho$ , specific heat  $C$  and temperature,  $T$ :

$$\Delta H = \int \rho C(T) dT . \quad (12)$$

Internal and external heat quantity of composite corrugated cases of fruits packaging system includes three parts:

external high-temperature air transfers heat to the inside of boxes through the box wall –  $q_1$ ,

heat brought by the gas exchange between side wall gaps of boxes inside the system –  $q_2$ ,

respiratory heat produced by fruits –  $q_3$ .

The total heat,  $Q_1$ , produced by above three methods after  $h$  hours is

$$Q_1 = h(q_1 + q_2 + q_3) = h \left[ KA(T_1 - T_2 + M(i_i - i_2) + 2.553 Gu) \right] , \quad (13)$$

where  $K$  refers to the heat transfer coefficient of the whole box,  $T_1$  and  $T_2$  are the internal and external temperatures of the box, respectively,  $A$  is the superficial area of the box,  $M$  is the quantity of heat exchange air every hour,  $G$  is the mass of fruits,  $i_1$  and  $i_2$  are specific enthalpy of the internal and external air of the box, respectively,  $u$  is the quantity of CO<sub>2</sub> produced by respiration of fruits in 1 h.

Suppose the freshness of fruits can be preserved for  $h$  hours at temperature  $T$  °C, meaning that the color, aroma, taste and edible value of fruit are not affected. The endothermic process of fruits in the box is also a constant-pressure process, thus the heat consumed by increase of 1 °C of fruits is constant-pressure specific heat,  $C_p$ . The symbol  $Q_2$  refers to the quantity of heat consumed by the increase of fruits temperature from  $T_1$  to  $T$ . Suppose other heat losses are ignored, then according to the law of

conservation of energy, the total heat,  $Q_1$ , input by external environment is equal to the heat,  $Q_2$ , absorbed by fruits

$$Q_1 = Q_2 = GC_p(T - T_1) . \quad (14)$$

Heat-shielding performance of composite corrugated cases was simulated in this study. Heated pure water (physical heat source) was used to replace the respiratory heat of fruits (biological heat source). Thus, according to Eqs. (13) and (14):

$$Q_1 = h[K A(T_1 - T_2) + M(i_1 - i_2)] = cM_1(T - T_1) , \quad (15)$$

where  $c$  refers to the specific heat of water and  $M_1$  is the mass of heated pure water. Specific enthalphy of internal air and external air of the box is  $i_1 - i_2 = (1.01 + 1.84d)(T_1 - T_2)$ , where  $d$  denotes the relative humidity of air. Thus the computational formula of heat conductivity coefficient,  $K$ , of the whole box can be obtained from Eq. (15)

$$K = \frac{cM_1(T - T_1)}{hA(T_1 - T_2)} - \frac{M(1.01 + 1.84d)}{A} . \quad (16)$$

## 4 Heat balance of refrigerator van

A mechanical refrigerated car used for short-distance refrigerated transport was taken as the research object in this study. The size of the car was, length×width×height, of 4.2 m × 2.2 m × 2.2 m. Polyurethane extruded sheet was used as the thermal insulation material of the car and its thickness was 0.1 m. The refrigerating system was inside the car, which could adjust the temperature.

### 4.1 Heat balance method

Heat balance method refers to considering all kinds of factors of dissipation of cooling capacity of the refrigerator car on the basis of the heat balance theory, and such method has accurate calculation, while it is also complicated in calculation of the thermal load of refrigerator. The total thermal load of the refrigerator car is the sum of load from outside and the load produced inside the car, which includes following four parts:

$$Q = Q_1 + Q_2 + Q_3 + Q_4 . \quad (17)$$

1. Heat,  $Q_1$ , introduced from the outside environment can be expressed as

$$Q_1 = 1.1(Q_b + Q_s + Q_l + Q_d), \quad (18)$$

where factor 1.1 refers to the loss coefficient.  $Q_b$  is the heat quantity introduced through the car (W),

$$Q_b = K F_m (t_e - t_i), \quad (19)$$

where  $K$  refers to the overall heat transfer coefficient of the car, and

$$F_m = \sqrt{F_e F_i}, \quad (20)$$

is the average heat transfer area of the car, where  $F_e$  and  $F_i$  are the exterior and interior superficial area of the car, respectively. In Eq. (19)  $t_e$  refers to the average temperature of environment and  $t_i$  is the average temperature inside the car).  $Q_s$  refers to the heat quantity transferred into the car from solar radiation,

$$Q_s = K F_s \Delta t_s \frac{\tau_s}{24}, \quad (21)$$

where  $F_s$  refers to the area affected by solar radiation,  $\Delta t_s$  is the increase of temperature under the effect of solar radiation, and  $\tau_s$  is the time of solar radiation.  $Q_l$  refers to heat quantity introduced by air permeation,

$$Q_l = \beta Q_b, \quad (22)$$

where  $\beta$  is the additional heat load coefficient of air permeation.  $Q_d$  refers to heat quantity introduced by the open of car door,

$$Q_d = f (Q_b + Q_s), \quad (23)$$

where  $f$  is the additional heat load coefficient of door opening (Tab. 1 shows the additional heat load coefficient of door opening during transportation).

2. Cooling capacity,  $Q_2$ , consumed by the thermal insulation material and the precooling of components is

$$Q_2 = \frac{1}{2} \sum (G C) \frac{\Delta t}{\Delta \tau}, \quad (24)$$

where  $G$  refers to the quality of thermal insulation materials or car components,  $C$  refers to corresponding specific heat,  $\Delta t$  is the temperature difference, and  $\Delta \tau$  is the time difference.

Table 1: Additional heat load coefficient of door opening.

Opening frequency (times)	Additional heat load coefficient $f$
0	0.25
1-5	0.5
6-10	0.75
11-15	1

3. The cooling capacity,  $Q_3$ , consumed by the precooling of products is

$$Q_3 = G_f C_f \frac{\Delta t}{\Delta \tau}, \quad (25)$$

where  $G_f$  refers to the quality of products, and  $C_f$  is the specific heat of products.

4. Heat quantity,  $Q_4$ , produced inside the car is

$$Q_4 = Q_f + Q_i. \quad (26)$$

Here

$$Q_f = G_f q_f \quad (27)$$

refers to the heat release of products (respiratory heat of vegetables, etc.), where  $q_f$  is the heat released by products per kilogram per hour, and

$$Q_i = P_i t_i \frac{1}{24} \quad (28)$$

refers to heat quantity produced by illumination inside the car, where  $P_i$  is the power of lighting, and  $t_i$  is the illuminating period.

During the transportation of the eutectic plate refrigerated car, the cooling consumption amount is balanced by melting of eutectic ice, thus to maintain the low temperature inside the car and guarantee the quality of fresh products.

#### 4.2 Stacking of refrigerated products inside the car

Spaces between products and products and the car wall should be guaranteed because good heat exchange and temperature require good ventilation.

Figure 1 shows a way of stacking products; A1 refers to the car body and A2, . . . , A9 refers to the stacking area. Each stacking area has a push plate. Each push plate is placed with three layers of products and each layer is placed with two packing boxes. The space between car roof and the top of third layer is 0.1 m, the distance between boxes and car wall is 0.15 m, the distance between A2 and A6 and the car tail is 0.2 m, the distance between A5 and A9 and front of car is 0.3 m, the line spacing and row spacing are 0.1 m and 0.2 m, respectively [17].

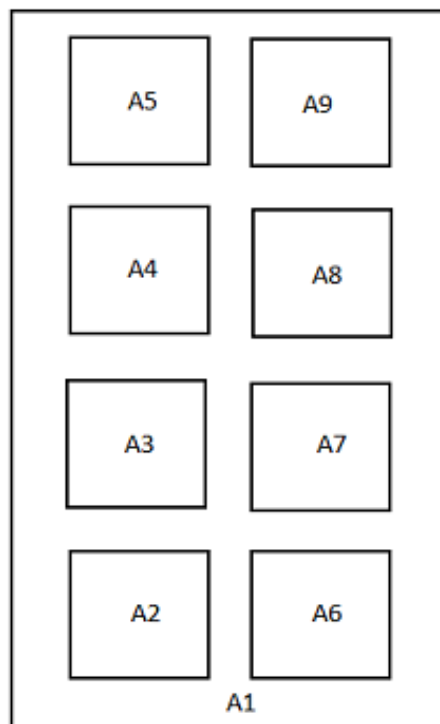


Figure 1: Stacking of products.

## 5 Heat produced by car during the process of transportation

Heat produced by the refrigerator car during transportation can be divided into two kinds: heat produced by quality degradation of thermal insulation

materials of car or door opening during transportation

$$Q_1 = \lambda_0 S \Delta T, \quad (29)$$

and heat caused by thermal radiation of the sun

$$Q_2 = 0.45 \lambda_0 S \Delta T' Z. \quad (30)$$

In above equations  $\lambda_0$  refers to the heat conductivity of the car, which is  $0.55 \text{ W/(m K)}$ ,  $S$  is the the heat exchange area of car,  $\Delta T$  and  $\Delta T'$  are the temperature difference inside and outside the car, and between car surface and the inside of car, respectively,  $Z$  is environmental coefficient.

## 6 Simulation of temperature field inside the refrigerator car

Using Ansys Flotran software, this study simulated and analyzed the temperature field inside the refrigerator car [18,19].

### 6.1 Modeling and grid generation

Construction of models is accomplished by the modeling module of Ansys software. The top view of car is drawn by using Solid 8node77 for grid generation. Stocking areas A2, A3, A4, A5, A6, A7, and A8 are spaces for corrugated boxes. Gas flow space of the car and the overall space of the car are given grid generation [20–22].

### 6.2 Definition of material parameters

**Parameters of products [23]** Bergamot pears were used as the research objects in this study, because they had regular shapes, thus spaces between pears could be left after pears were placed in boxes, which made the simulation results much closer to the reality. The shape of bergamot pears was taken as a sphere approximately in this study and the diameter was  $D = 0.6 \text{ m}$ ; the heat conductivity of the bergamot pear was  $\lambda = 0.14 \text{ W/(m K)}$ .

Suppose bergamot pears occupied 60% of the volume in each corrugated box, porosity  $\zeta = 0.4$ , density of bergamot pears is  $\rho = 700 \text{ kg/m}^3$  and the specific heat capacity of bergamot pears  $C = 2.45 \text{ KJ/(kg K)}$ . Appropriate temperature for transportation of bergamot pears is  $5^\circ\text{C}$ .

**Physical property parameters of the cold air in car** Power of the refrigeration equipment was 1050 W when the operating temperature was 0°C, when the operating temperature exceeded 3°C the power was 900 W. Air density  $\rho = 1.228 \text{ kg/m}^3$ ; heat conductivity of air was  $\lambda = 0.16 \text{ W/(m K)}$ ; coefficient of thermal expansion of air was  $\beta = 3.378 \times 10^{-3} \text{ 1/K}$ , dynamic coefficient of viscosity of air was  $\mu = 1.85 \times 10^{-5} \text{ N s/m}^2$ , specific heat capacity of air was  $C = 2.62 \text{ KJ/(kg K)}$ ; air speed of cold air outlet was  $v = 1 \text{ (m/s)}$ , temperature of cold air was  $t = 0.3 \text{ }^\circ\text{C}$ .

### 6.3 Results of simulation and analysis

Average temperatures of products in the car at different cryogenic temperatures are shown in Fig. 2.

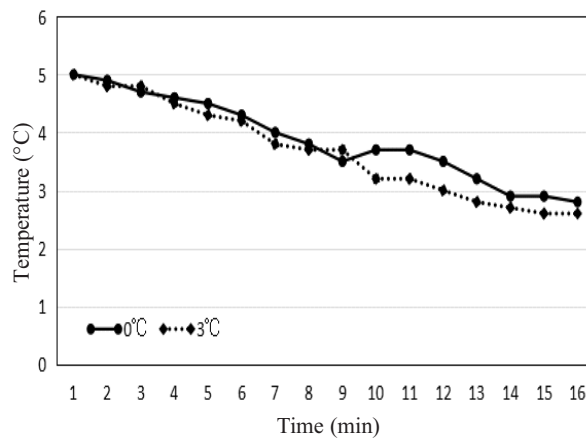


Figure 2: Average values of temperature changes of products.

Figure shows that, the temperature changes of products during transportation are nonlinear. The total distance covered by the refrigerator car was 120 km, which takes 3 h; during the transportation, different temperatures inside of car could lead to different consumption of energy. Specific data are shown in Tab. 2.

Data in table show that, in the first kind of refrigerating method, the refrigerating temperature was 0°C and the refrigerating time was 15 min for each time, 20 min of pause between each time, thus the overall operating time of the refrigerating system was 60 min and energy consumption was

Table 2: Energy consumption in different refrigerating methods.

Refrigerating temperature ( $^{\circ}\text{C}$ )	0	3
Number of refrigerations	4	5
Energy consumption (KJ)	$3.75 \times 10^3$	$2.74 \times 10^3$

$3.75 \times 10^3$  KJ. In the second kind of refrigerating method, the refrigerating temperature was  $3^{\circ}\text{C}$  and the refrigerating time was 10 min for each time, 15 min of pause between each time, thus the overall operating time of the refrigerating system was 50 min and the energy consumption was  $2.74 \times 10^3$  KJ. Obviously, the second method not only satisfied the low-temperature operation, but also saved  $1.01 \times 10^3$  KJ of energy consumption, which decreased by 26.9% and reduced transportation costs. Thus the second method was more appropriate for refrigeration.

## 7 Summary

This study analyzes heat balance of corrugated boxes based on elementary knowledge of heat transfer theory, and the heat balance equation of corrugated boxes is constructed on the basis of heat transfer process of corrugated boxes, heat exchange of ventilation hole, and respiratory heat of products. Some of the minor parameters are neglected in the thermal analysis of products, such as the self respiration heat of different fruits and vegetables, thus this study has certain limitations.

Received 28 May 2016

## References

- [1] ZHANG Z., GAO Z., MIN L.I. *et al.*: *Effect of food additives on postharvest pathogens and preservation of mango fruit*. Chinese J. Tropical Crops **34**(2013), 11, 2289–2294.
- [2] ZHANG B.N., ZHU X.Y., LAI J.: *Effect of ozone water treatment on preservation of chinese chestnut fruits during storage*. Food Sci. **32**(2011), 16, 361–364.
- [3] WANG F.C., JUN-GUO L.I., DONG Y.C. *et al.*: *Research progress of application of polysaccharides and modified polysaccharides in film coatings for food preservation*. Food Sci. **33**(2012), 5, 299–304.
- [4] TAN Y.B., ZHANG Q.Y.: *Food cold chain transportation management based on grid technology*. Appl. Mech. Mater. **543-547**(2014), 4540–4542.

- [5] JIA K.: *Design of wireless sensor node in cold chain transportation monitoring*. Trans. Chinese Soc. Agricultural Machinery **44**(2013), 2, 136–141.
- [6] NET M., TRIAS E., NAVARRO A. *et al.*: *Cold chain monitoring during cold transportation of human corneas for transplantation*. Transpl. P. **35**(2003), 5, 2036–2038.
- [7] YUE J., LIU L., LI Z. *et al.*: *Improved quality analytical models for aquatic products at the transportation in the cold chain*. Math. Comput. Model. **58**(2013), 3–4, 474–479.
- [8] LIU L., HU J.Y., ZHANG J.J. *et al.*: *Development of time-temperature data collection program for frozen fish in the cold chain*. Sensor Lett. **8**(2010), 1, 47–51.
- [9] JEDERMANN R., RUIZ-GARCIA L., LANG W.: *Spatial temperature profiling by semi-passive RFID loggers for perishable food transportation*. Comput. Electron. Agr. **65**(2009), 2, 145–154.
- [10] JAREMKIEWICZ M.: *Determination of transient fluid temperature using the inverse method*. Arch. Thermodyn. **35**(2014), 1, 61–76.
- [11] MIKIELEWICZ D., ANDRZEJCZYK R., JAKUBOWSKA B. *et al.*: *Comparative study of heat transfer and pressure drop during flow boiling and flow condensation in minichannels*. Arch. Thermodyn. **35**(2014), 3, 17–37.
- [12] VASILIEV L., VASILIEV L., ZHURAVLYOV A. *et al.*: *Vapordynamic thermosyphon - heat transfer two-phase device for wide applications*. Arch. Thermodyn. **36**(2015), 4, 65–76.
- [13] MIKIELEWICZ D., MUSZYŃSKI T., MIKIELEWICZ J.: *Model of heat transfer in the stagnation point of rapidly evaporating microjet*. Arch. Thermodyn. **33**(2012), 1, 139–152.
- [14] WANG J.L.: *Based on the finite element software ANSYS/LS-DYNA metal plate covering parts forming process simulation and optimization research*. Adv. Mater. Res. **912–914**(2014), 589–592.
- [15] OLUWOLE L., ODUNFA A.: *Investigating the effect of ocean waves on gravity based offshore platform using finite element analysis Software ANSYS*. Int. J. Sci. Eng. Res. **6**(2015), 8, 24–33.
- [16] DELELE M.A., NCOBO M.E.K., OPARA U.L. *et al.*: *Investigating the effects of table grape package components and stacking on airflow, heat and mass transfer using 3-D CFD modelling*. Food Bioprocess Tech. **6**(2013), 9, 2571–2585.
- [17] DEFRAEYE T., VERBOVEN P., OPARA U.L. *et al.*: *Feasibility of ambient loading of citrus fruit into refrigerated containers for cooling during marine transport*. Biosyst. Eng. **134**(2015), 20–30.
- [18] ZHOU Y.: *Effect of velocity of fluid field of 3-spacer nozzle in roll-casting models using coupled fluid-thermal finite element analysis*. Appl. Mech. Mater. **29–32**(2010), 1481–1487.
- [19] ELNAGGAR M.H.A., ABDULLAH M.Z., MUNUSAMY S.R.R.: *Experimental and numerical studies of finned L-shape heat pipe for notebook-PC cooling*. IEEE T. Comp. Pack. Man. **3**(2013), 6, 978–988.
- [20] MAMUN K.A., STOKES J.: *Development of a semi automated dual feed unit to produce FGM coatings using the HVOF thermal spray process*. South Pacific J. Natural Appl. Sci. **32**(2014), 1, 18–26.

- 
- [21] LUO Z.B.: *Effects of different vents location on flow characteristics of air conditioning*. Appl. Mech. Mater. **622** (2014), 179–182.
- [22] SPANO M., STARA V.: *Application of a 2D turbulence model for estimation of the discharge coefficient on round-shaped weirs*. AIP Conf. Proc. **1048**(2008), 1, 806–809.
- [23] XIAO Y., LIU D.: *Agricultural products refrigerated and insulated transport technology and equipment research*. J. Agr. Mech. Res. **33**(2011), 1, 57–60.



archives  
of thermodynamics

Vol. 37(2016), No. 4, 137–159

DOI: 10.1515/aoter-2016-0032

## Performance analyses of helical coil heat exchangers. The effect of external coil surface modification on heat exchanger effectiveness

RAFAŁ ANDRZEJCZYK  
TOMASZ MUSZYŃSKI\*

Gdańsk University of Technology, Narutowicza 11/12, 80-233 Gdańsk, Poland

**Abstract** The shell and coil heat exchangers are commonly used in heating, ventilation, nuclear industry, process plant, heat recovery and air conditioning systems. This type of recuperators benefits from simple construction, the low value of pressure drops and high heat transfer. In helical coil, centrifugal force is acting on the moving fluid due to the curvature of the tube results in the development. It has been long recognized that the heat transfer in the helical tube is much better than in the straight ones because of the occurrence of secondary flow in planes normal to the main flow inside the helical structure. Helical tubes show good performance in heat transfer enhancement, while the uniform curvature of spiral structure is inconvenient in pipe installation in heat exchangers. Authors have presented their own construction of shell and tube heat exchanger with intensified heat transfer. The purpose of this article is to assess the influence of the surface modification over the performance coefficient and effectiveness. The experiments have been performed for the steady-state heat transfer. Experimental data points were gathered for both laminar and turbulent flow, both for co current- and countercurrent flow arrangement. To find optimal heat transfer intensification on the shell-side authors applied the number of transfer units analysis.

**Keywords:** Effectiveness; Heat transfer intensification; Number of transfer unit; Helical coil

---

\*Corresponding Author. E-mail: tommuszy@pg.gda.pl

## Nomenclature

$A$	–	heat transfer surface area, $m^2$
$B$	–	outside diameter of inner cylinder, m
$C$	–	inner shell diameter, m
$C_{co}$	–	contraction coefficient
$C_D$	–	drag coefficient
$c_p$	–	specific heat, J/kgK
$D$	–	Dean number
$D_e$	–	shell side equivalent diameter, m
$D_H$	–	average diameter of helix, m
$D_0$	–	outside tube coil diameter, m
$d_0$	–	internal tube coil diameter, m
$E$	–	coefficient in Mishra and Gupta equation, m
$g$	–	gravitational acceleration, $m/s^2$
$G$	–	mass flow rate, $kg/m^2s$
HTC	–	heat transfer coefficient
HX	–	heat exchangers
$f$	–	friction factor
$F$	–	fluid correction factor
$H$	–	height of shell, m
$L$	–	length of coil, m
LMTD	–	logarithmic mean temperature difference
$m$	–	mass flow, kg/s
$N$	–	number of turns of helical coil
NTU	–	number of transfer units
Nu	–	Nusselt number
$p$	–	distance between consecutive coil turns, m
Pr	–	Prandtl number
$\Delta P$	–	pressure drop, Pa
$\dot{Q}$	–	heat flux, W
$q_w$	–	wall heat flux, $W/m^2$
Ra	–	Rayleigh number
$R$	–	fouling factor, $m^2K/W$
$r$	–	pipe radius, m
Re	–	Reynolds number
$T$	–	temperature, K
$U$	–	overall heat transfer coefficient, $W/m^2K$
$w$	–	velocity, m/s
$W$	–	fluid heat capacity rate, W/K
$\dot{V}$	–	volumetric flow, $m^3/s$

## Greek symbols

$\alpha$	–	heat transfer coefficient, $w/m^2K$
$\delta$	–	wall thickness, m
$\gamma$	–	area ratio
$\rho$	–	density, $kg/m^3$

$\zeta$	–	friction factor for components
$\varepsilon$	–	heat exchanger effectiveness
$\psi_s$	–	separated flow multiplier
$\lambda$	–	thermal conductivity, W/mK
$\mu$	–	dynamic viscosity, Pa s
$\nu$	–	kinematic viscosity, m <sup>2</sup> /s

### Subscripts

<i>av</i>	–	average
<i>c</i>	–	cold
<i>cor</i>	–	corrected
<i>c – a</i>	–	average at coil side
<i>c – s</i>	–	coil side
<i>con</i>	–	contraction
<i>CU</i>	–	copper
<i>exp</i>	–	expansion
<i>h</i>	–	hot
<i>i0</i>	–	internal
<i>min</i>	–	minimum
<i>max</i>	–	maximum
<i>s – a</i>	–	average at shell side
<i>s</i>	–	surface
<i>sh</i>	–	shell side
<i>t</i>	–	tube
<i>w</i>	–	wall

## 1 Introduction

Striving to ensure high performance of the heat exchangers, HX, nowadays is a source of universal trend both to the miniaturization of these devices for both industrial and domestic applications, while maintaining the highest possible size to thermal energy ratio. As is well known, in the case of recuperators the heat transfer coefficient has a decisive influence on their efficiency [1]. Overall heat transfer coefficient, depends mainly on the lower value of heat transfer value (HTC) from working media [2]. It is, therefore, most significant to improve the heat transfer with special attention on the side of the medium with lower heat transfer coefficient [3].

Helical coils are widely used in applications such as heat recovery systems, chemical processing, food processing, nuclear reactors, and high-temperature gas cooling reactors. Helical coils have been widely studied both experimentally [4] and numerically [5].

Helical coils are characterized by their compactness and high heat transfer coefficient. When fluid flows through a helically coiled tube, the cur-

vature of the coil induces centrifugal force, causing the development of the secondary flow. This secondary flow enhances fluid mixing and thus heat transfer. Fluid flow in a helical tube is characterized by the Dean number. The Dean number,  $D$ , is a measure of the geometric average of inertial and centrifugal forces to the viscous force ratio, and thus is a measure of a magnitude of the secondary flow. For laminar flow and small pipe to coil radius aspect ratio  $r/R$ , frictional loss in a curved tube may be represented as a function of the Dean number. One of the most frequent uses of helically coiled tubes is in the shell and coiled tube heat exchangers.

The majority of the studies related to helically coiled tubes and heat exchangers have dealt with two major boundary conditions, i.e., constant heat flux and constant wall temperature [6,7]. However, these boundary conditions are not encountered in most single-phase heat exchangers.

Naphon [8] has investigated thermal performance of helical coils with and without fins. Two different coil diameters with 9.5 mm diameter copper tube having thirteen turns were used. Hot and cold water were used as working fluid in the range from 0.10 to 0.22 kg/s and from 0.02 to 0.12 kg/s, respectively. They have shown that with increasing hot water mass flow rate the friction factor decreased.

Various helical coils made from a 12.5 mm ID (inside diameter) tube with various coil diameters ranging from 92 to 1282 mm have been investigated by Srinivasan *et al.* [9] to determine friction factors. Four different coil pitches of 2.5, 3.3, 6.6, and 13.2 tube diameters were tested and graphs of friction factors with respect to the Dean number were produced. All the graphs showed breakpoints which were interpreted as the critical Reynolds number value so that equation was found to describe this critical value for different tube diameter to shell diameter ratio.

Kumar *et al.* [10] studied a tube-in-tube helically coiled heat exchanger for turbulent flow regime. Numerical investigations were done to understand forced laminar fluid flow in rectangular coiled pipes with circular cross-section by Conte and Peng [11]. Their focus was addressed on exploring the flow pattern and temperature distribution through the pipe.

Patankar *et al.* [12] discussed the effects of the Dean number on friction factor and heat transfer in the developing and fully developed regions of helically coiled pipes. Comparisons between the proposed model and the experiment showed good agreement. However, the effects of the torsion and the Prandtl number were not taken into account in the aforementioned model.

Jamshidi *et al.* [13] experimentally considered the effects of the geometric parameters to enhance the heat transfer rate in the shell and coiled-tube heat exchangers. The results indicated that the higher coil diameter, coil pitch, and mass flow rate in the shell and tube can enhance the heat transfer rate in these types of heat exchangers. Xin *et al.* [14] studied single-phase flow in a helical double tube heat exchanger in horizontal and vertical arrangements. In their paper, the influence of coil geometry, the flow rate of air and water on the pressure drop of single phase flow was surveyed.

Petrakis and Karahalios [15,16] obtained the numerical solution of incompressible viscous fluid flow equation for water flowing in a curved double tube with circular cross section. In this investigation, it was indicated that in small core radius, the change of Dean number has a considerable effect on fluid properties whereas it was not observed in the large radius.

Di Liberto and Ciofalo [17] studied the heat transfer of turbulent flow in curved tubes by numerical simulation. They also used this method to survey a fully developed turbulent flow in curved tubes. Results of this study indicated that in the curved tubes, the temperature fluctuations in outer regions are more pronounced than in other regions.

Moawed [18] reported an experimental investigation of steady-state natural convection heat transfer from uniformly heated helicoidal pipes oriented vertically and horizontally. His experimental investigation was conducted on four helicoidal pipes having different ratios of coil diameter to pipe diameter, pitch to pipe diameter and length to pipe diameter with the range of Rayleigh number  $1.5 \times 10^3 < Ra < 1.1 \times 10^5$ . His results showed that the overall Nusselt number increases with the increase of coil to tube diameter ratio, dimensional pitch and length of coil to tube diameter for the vertical helicoidal pipes. For the horizontal helicoidal pipes, the overall Nusselt number increased with the increase of dimensional pitch and length of coil to tube diameter, but it decreased with the increase of coil to tube diameter ratio. He presented two different equations to correlate the Nusselt number for horizontal and vertical helicoidal pipes.

Literature review, reveals that there are a few investigations on the heat transfer coefficients of helical coil heat exchangers considering the geometrical effects and coil surface modifications. Also, this scarcity is more prominent for the shell-side heat transfer coefficients. Most of the researchers performed their work on the helically coiled heat exchanger with constant heat flux and constant wall temperature as major boundary conditions.

The paper presents labor that was carried out in several stages. The

first part of this paper presents the construction of the test facility and the design and construction of test exchangers. The second part presents experiments which were carried out on single-phase convection heat transfer with distilled water as a working medium.

## 2 Heat exchanger modeling

In order to conduct experimental research to verify the influence of the surface modification on the heat transfer coefficient of the coiled tube a reference heat exchanger model was proposed. Heat transfer coefficient outside the coil was calculated based on the works of methodology showed earlier in the literature [19,20]. Helically coiled tubes show some peculiar characteristics and phenomenological aspects of the thermohydraulics that are worthy of a brief description. First of all, coiled pipes are compact, can well accommodate the thermal expansions and have a high resistance to flow induced vibrations [21,22]. Furthermore, the fluid flowing in helical tubes develops secondary flows whose physical explanation is represented in Fig. 1. The curved shape of the inner tube of HX causes the fluid to experience a centrifugal force which depends on its local axial velocity of Fig. 1b. Due to the boundary layer, the fluid particles flowing close to the tube wall have a lower velocity with respect to the fluid flowing in the core of the tube thus they are subject to a lower centrifugal force [23,24]. As a consequence, fluid from the core region is pushed outwards forming a pair of recirculating counter-rotating vortices as presented in Fig. 1c.

In the Reynolds number range of  $50 < Re_{sh} < 10000$  the Nusselt number at shell side can be expressed as [25]

$$Nu_{sh} = 0.6 Re_{sh}^{0.5} Pr^{0.31}, \quad (1)$$

where  $Pr$  is the Prandtl number, and for  $Re_{sh} > 10000$

$$Nu_{sh} = 0.36 Re_{sh}^{0.55} Pr^{0.333} \left( \frac{\mu}{\mu_p} \right)^{0.14}, \quad (2)$$

where  $\mu$  and  $\mu_p$  are the dynamic viscosity of the wall and fluid, respectively. In shell side flow, Reynolds number is calculated as the mass flow rate,  $G_{sh}$ , through equivalent diameter,  $D_e$ ,

$$Re_{sh} = \frac{G_{sh} D_e}{\mu_l}. \quad (3)$$

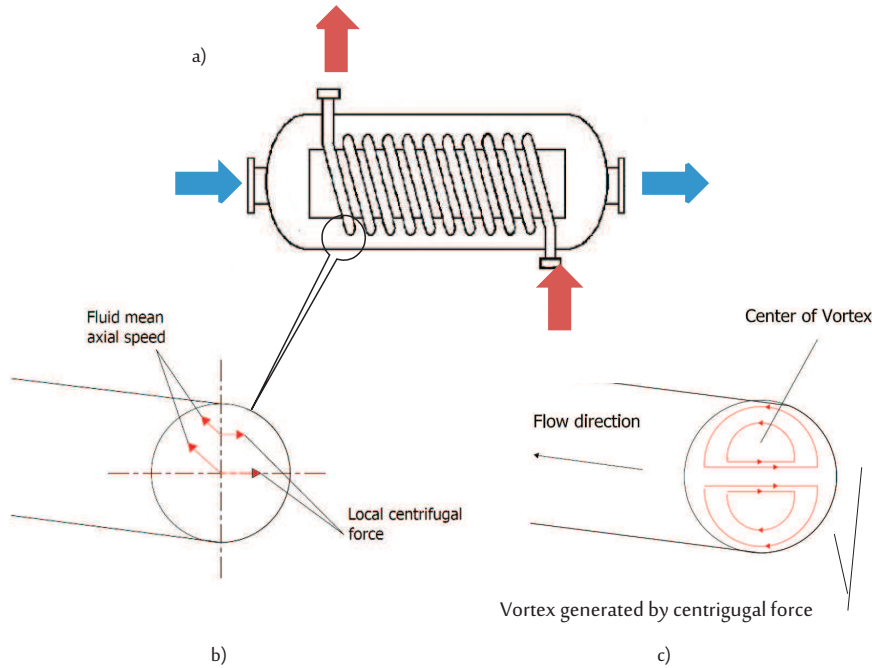


Figure 1: Shell coil heat exchanger view (a), centrifugal force acting on the flowing fluid and axial speed (b), resulting secondary flows (c).

Equivalent diameter depends on the volume of the annulus divided by heat exchanger length and the circumference

$$D_e = \frac{4V_{sh}}{\pi D_0 H} . \quad (4)$$

The volume available for the flow of fluid in the annulus,  $V_{sh}$ , can be calculated knowing geometrical dimensions of the heat exchanger (Fig. 2 and Tab. 1)

$$V_{sh} = \frac{\pi}{4} C^2 p N - \frac{\pi}{4} D_0^2 L . \quad (5)$$

Inside the coil, authors decided to use the Dittus-Boelter correlation for dimensionless heat transfer coefficient [26]

$$\text{Nu}_{DB} = 0.023 \text{Re}^{0.8} \text{Pr}^{0.4} . \quad (6)$$

Corrected for the coiled tube it becomes

$$\alpha_{io} = \alpha_{DB} \left\{ \left[ 1 + 3.6 \left( 1 - \frac{\delta}{0.5d_0} \right) \right] \left( \frac{\delta}{0.5d_0} \right)^{0.8} \right\} , \quad (7)$$

where  $\delta$  is the wall thickness, and  $\alpha_{DB}$  means the heat transfer coefficient calculated by Eq. (6), Re is based on inner pipe diameter,  $d_0$ , and fluid velocity inside the coil,  $w_{c-s}$

$$\text{Re} = \frac{w_{c-s}d_0}{\nu}, \quad (8)$$

where  $\nu$  is the kinematic viscosity of fluid.

Overall heat transfer coefficient can be calculated as

$$\frac{1}{U} = \frac{1}{\alpha_{sh}} + \frac{1}{\alpha_{i0}} + \frac{\ln\left(\frac{D_0}{d_0}\right)}{2\pi\lambda_{cu}L} + R_t + R_{sh}. \quad (9)$$

In present study required heat load was set as  $\dot{Q} = 1200$  W. Thus the contact area,  $A$ , can be calculated from

$$A = \frac{\dot{Q}}{U \text{LMTD}}. \quad (10)$$

The logarithmic mean temperature difference LMTD can be used as an average acting temperature gradient between two fluids. It can be written as

$$\text{LMTD} = \frac{(T'_h - T'_c) - (T''_h - T''_c)}{\ln\left(\frac{T'_h - T'_c}{T''_h - T''_c}\right)}, \quad (11)$$

where subscripts  $h$  and  $c$  indicate hot and cold fluids, and superscripts 'prim' and 'double prim' denote temperature at inlet and outlet, respectively.

LMTD is corrected with the fluid correction factor,  $F$

$$\text{LMTD}_{cor} = F \text{LMTD}. \quad (12)$$

The account for perpendicular flow, the correction factor of 0.99 [7].

The coil heat exchanger has been developed by using values of water properties for average temperature,  $T_{av}$ , of cold and hot media. The pressure drop of the heat exchanger for shell and coil side accordingly yields:

$$\Delta P_{sh} = C_D \frac{H}{D_e} \frac{\bar{w}_{s-a}^2 \rho}{2} + \sum \zeta \frac{\bar{w}_{s-a}^2 \rho}{2}, \quad (13)$$

$$\Delta P_{c-s} = f \frac{L}{d_0} \frac{\bar{w}_{a-c}^2 \rho}{2} + \sum \zeta \frac{\bar{w}_{a-c}^2 \rho}{2}, \quad (14)$$



where  $D_H$  is the average diameter of helix.

Drag coefficient on coil surface was calculated from the Brauer correlation [22]

$$C_D = \frac{0.3164}{\text{Re}^{0.25}} \left[ 1 + 0.095 \left( \frac{D_0}{D_H} \right)^{1/2} \text{Re}_{sh}^{0.25} \right]. \quad (17)$$

Local drag coefficients for Eqs. (13) and (14) were taken from Bell [23] and Achenbach [24].

### 3 Experimental setup

The main aim of surface modification was to increase turbulization at the outer surface of the coil. As well-known from literature, the heat transfer coefficient at shell side in case of typical helical heat exchangers is smaller than the one at coil side [13].



Figure 3: Obtained construction of helical coils: at the left side – coil made from smooth copper pipe, in the middle – coil with modified surface, at the right side – photo of modified surface.

Both coils have been made by using a small, smooth copper minichannel (see Fig. 3). The average length of channels is 1400 mm and average fin height was equal to 0.5 mm. Each one of built heat exchangers has the same shell construction.

The rig consists of two closed loops of test fluid. The facility was intended to work with any non-chemically aggressive working fluids. In both loops, circulation is forced by electrically powered pumps with a magnetic coupling, capable of providing the mass flow rate from 0.001 to 0.005 g/s and the overpressure up to 0.8 MPa. This type of pumps has been chosen

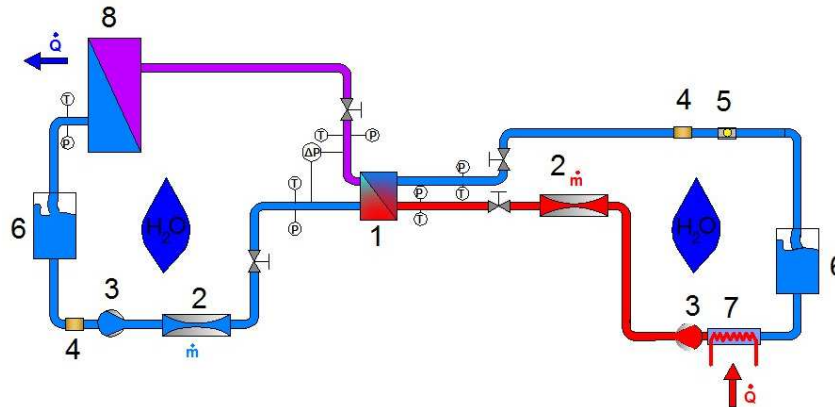


Figure 4: Schematic diagram of experimental rig: 1 – helical coil heat exchanger, 2 – Coriolis mass flow meter, 3 – nonpulsation gear pump, 4 – filter, 5 – inspection glass, 6 – fluid tank , 7 – heater, 8 – chiller.

to provide the circulation of fluid in the test sections and to avoid flow pulsations. Adjustment of the mass flow rate is realized by two independent inverters. Figure 4 presents a schematic diagram of the test facility.

The heat exchanger consists of a copper coiled tube and an insulated shell. The dimensions of the heat exchangers are depicted in Tab. 1. The hot fluid circuit is heated using a thermostatic bath. A pump circulates the hot water in the loop with a preset temperature. A set of valves is used to control the flow rate of cold and hot water, respectively. To measure the flow rates of the cold and hot fluids a Coriolis-type mass flow meters are installed upstream of the heat exchanger. The inlet and outlet temperatures of hot and cold water were recorded using four T-type thermocouples inserted at the inlet and outlet collectors. Also, all the pipes and connections between the temperature measuring stations and heat exchanger were duly insulated. In order to exclude heat capacity of heat exchanger casing from calculations, data points were gathered for steady state conditions. After obtaining constant parameters, temperatures were measured three times with an accuracy of 0.5 °C in the time steps of 20 min, and the average values were used for further analysis. Appropriate arrangements were provided to measure the pressure loss of both tube and shell side. All the tube- and shell-side fluid properties were assessed at the mean temperature of the fluid (average of inlet and outlet temperatures). The measured uncertainty parameters are shown in Tab. 3.

Table 3: Uncertainty of operating parameters.

Parameter	Operating range	Uncertainty
$d_0$ , mm	4	$\pm 0.003$
$D_0$ , mm	6	$\pm 0.003$
$m$ , kg/s	0.01–0.03	$\pm 0.3\%$
$T$ , °C	19–92	$\pm 0.5$
$\Delta p$ , kPa	0.2–2	$\pm 0.075\%$

## 4 Data reduction

The hot and cold heat flux are calculated as a product of water mass flux, water specific heat capacity and the inlet-outlet water temperature difference:

$$\dot{Q}_c = c_p m_c (T_{c,out} - T_{c,in}) , \quad (18)$$

$$\dot{Q}_h = c_p m_h (T_{h,in} - T_{h,out}) . \quad (19)$$

The measured pressure drop is the sum of friction pressure drop, and expansion and contraction losses due to the headers at both ends of the test section

$$\Delta P_{measured} = \Delta P_{frict} + \Delta P_{exp} + \Delta P_{con} . \quad (20)$$

The pressure drop due to contraction was estimated using a flow model recommended by Hewitt *et al.* [26] for single phase flow.

$$\Delta P_{con} = \frac{G^2}{2\rho} \left[ \left( \frac{1}{C_{con}} - 1 \right) + 1 - \gamma^2 \right] , \quad (21)$$

where  $\gamma$  is the area ratio ( $A_{test-section}/A_{header}$ ) and  $C_{con}$  is the coefficient of contraction, which is, in turn, a function of this area ratio,

$$C_{con} = \frac{1}{0.639(1 - \gamma)^{0.5} + 1} . \quad (22)$$

For the expansion into the header from the test section, the following flow model recommended by Hewitt *et al.* [27] was also used:

$$\Delta P_{exp} = \frac{G^2 \gamma (1 - \gamma) \psi_s}{\rho} , \quad (23)$$

where  $\psi$  is the separated flow multiplier, while is also a function of the phase densities and the quality. In single flow case, those multiplier and quality are equal to unity.

The number of transfer units, NTU, is calculated as

$$\text{NTU} = \frac{UA}{W_{min}} \quad (24)$$

where  $U$  is the overall heat transfer coefficient and  $A$  is the heat transfer surface area of the heat exchanger,

$$W_{min} = \min(W_c, W_h), \quad (25)$$

where  $W_c$  and  $W_h$  are the heat capacity rates of the cold and hot fluids, respectively. In heat exchanger analysis, it is also convenient to define another dimensionless quantity called the capacity ratio as

$$W = \frac{W_{min}}{W_{max}}, \quad (26)$$

where  $W_{max}$  is the higher of the two considered capacities.

The heat transfer effectiveness is defined as actual heat transfer rate to maximum possible heat transfer:

$$\varepsilon = \frac{\dot{Q}}{\dot{Q}_{max}}. \quad (27)$$

The actual heat transfer rate in a heat exchanger can be determined from an energy balance on the hot or cold fluids and can be expressed as

$$\dot{Q} = W_c(T_{c,out} - T_{c,in}) = W_h(T_{h,in} - T_{h,out}). \quad (28)$$

To determine the maximum possible heat transfer rate in a heat exchanger, we first recognize that the maximum temperature difference in a heat exchanger is the difference between the inlet temperatures of the hot and cold fluids

$$\Delta T_{max} = T_{h,in} - T_{c,in}. \quad (29)$$

Therefore, the maximum possible heat transfer rate in a heat exchanger is

$$\dot{Q}_{max} = W_{min}(T_{h,in} - T_{c,in}), \quad (30)$$

where  $W_{min}$  is the lower heat capacity of cold and hot fluid.

Experimental values of Nusselt number, Nu, at shell side and coil side were calculated as

$$\text{Nu}_{\text{exp}_{sh}} = \frac{\alpha_{\text{exp}_{sh}} D_e}{\lambda}, \quad (31)$$

$$\text{Nu}_{\text{exp}_{c-s}} = \frac{\alpha_{\text{exp}_{c-s}} d_0}{\lambda}. \quad (32)$$

The Dean number, D, is a dimensionless group in fluid mechanics, which occurs in the study of flow in curved pipes and channels (Fig. 2):

$$D = \frac{\rho w d_0}{\mu} \left( \frac{d_0}{2r} \right)^{\frac{1}{2}}, \quad (33)$$

$$U = \frac{1}{\frac{1}{\alpha_{\text{exp}_{sh}}} + \frac{1}{\alpha_{\text{exp}_{i0}}} + \frac{\ln \left( \frac{D_0}{d_0} \right)}{2\pi \lambda_{CU} L}}. \quad (34)$$

## 5 Experimental results

In order to estimate the influence of surface modifications on flow through the heat exchanger, as the first step of experimental validation hydraulic performance of heat exchanger was examined. Because only coil external surface was modified only shell side flow was investigated in detail for both reference and modified geometry.

As can be seen in Fig 5. there is no significant difference between the hydraulic characteristic of plain and modified helical coil heat exchanger. It should be noted also that the predicted value of pressure drop with Eq. (13) has good agreement with experimental results, but it tends to over predict  $\Delta P$  values for higher flow rates. As well as pressure drop in shell side the experimental data for pressure drop at coil side was compared with the prediction given by Eq. (14). Figure 6 clearly presents acceptable agreement between predictions and experimentally obtained results.

Figure 7 presents' linear regression values for experimental series grouped in constant shell side fluid velocities (cold). The resulting heat transfer coefficient of cold fluid from experimental data was calculated based on Wilsons plot method [3]. The heat transfer coefficient was calculated for the tube thickness of 1 mm. The tube material (copper) has the thermal conductivity,  $\lambda$ , equal to 389 W/mK. It has to be noted that overall heat transfer coefficient generally is larger for the modified construction of heat

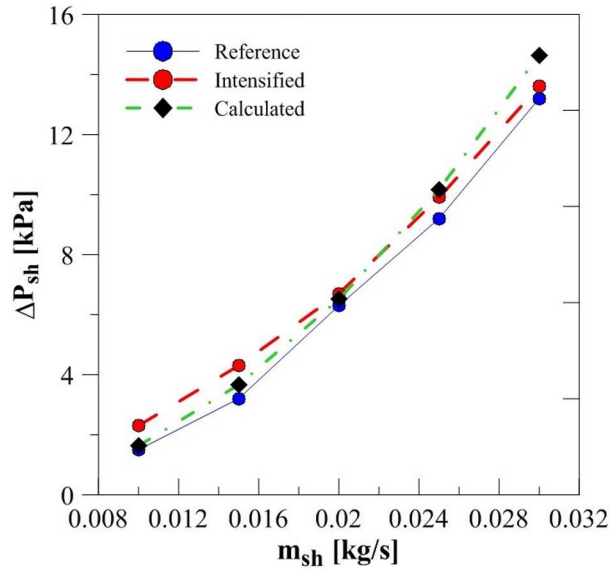


Figure 5: Pressure drops in shell side as a function of mass flow rate.

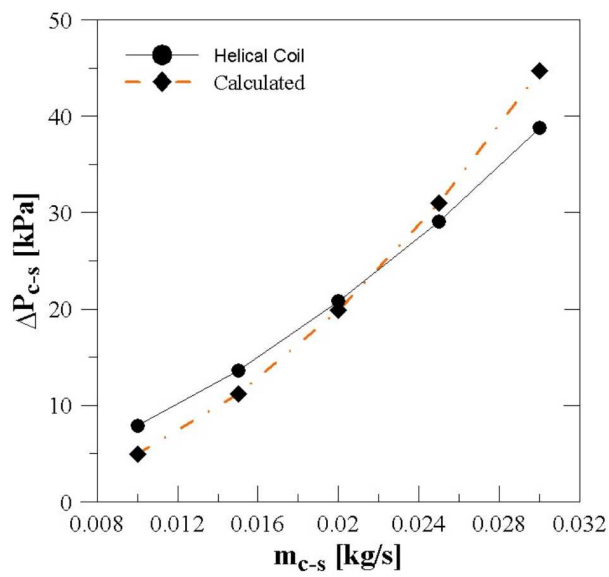


Figure 6: Pressure drops in coil side as a function of mass flow rate.

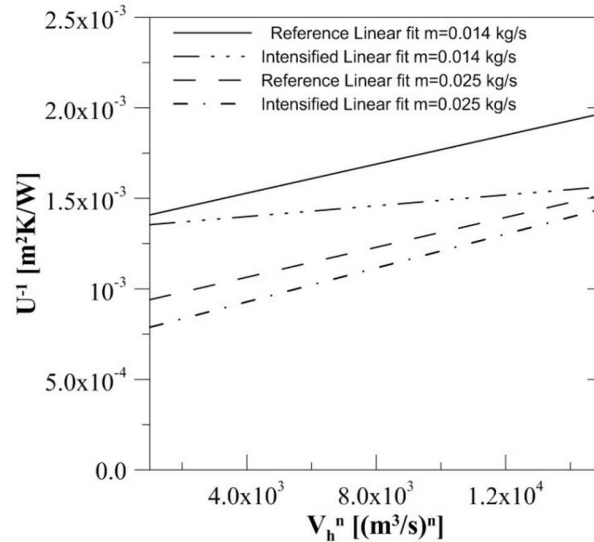


Figure 7: Linear regression of experimental data for calculating heat transfer coefficient by Wilsons plot method, for varying hot and constant cold fluid mass flow rate in case of countercurrent flow.

exchanger. But the difference is quite small. The low values for the small flow velocities could also be due to the nature of the Wilson plots. It was noted that small changes in the coefficients used in the Wilson plots had a small effect on the inner Nusselt numbers, but much larger effects on the annulus Nusselt numbers. So the Wilson plots may be part of the reason for the divergence between the experimental and predicted values.

Based on a comparison of theoretical values of Nusselt numbers and experimental results a good agreement of used correlations can be stated. The differences at shell side and coil side are not larger than 30%. Results were shown in Figs. 8 and 9. As was expected based on analytical modeling of coil heat exchanger the Nusselt number for coil side are clearly larger than the shell side. Considering pressure drop at shell side are also significantly smaller than at the coil side.

Figure 10 represents the variations of Nusselt number versus Dean number for three different water inlet temperatures at shell side and at coil side for reference heat exchanger construction. It is important to notice that increment of water temperature reduces obtained Nusselt numbers at shell side, especially in the low Dean number region. Unfortunately for coil side the difference is so small than even after zoom experimental points, it is

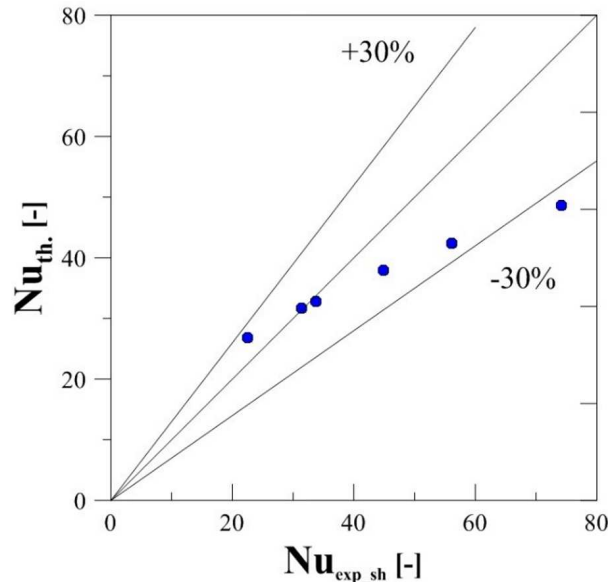


Figure 8: Comparison of experimental and theoretical Nusselt number for shell side in case of the unmodified surface.

negligible. It is also seen that at higher temperatures, the range of Dean number is greater as a result of lower water viscosity.

One of the most common methods to compare the various types of heat exchangers is to use  $\varepsilon$ -NTU methodology [28–30]. Collected experimental data for co- and countercurrent flow configuration in each of presented heat exchangers allow verifying the influence of temperature field on heat transfer coefficient. Figures 11 and 12 show the effectiveness of coil heat exchangers calculated using Eq. (27) as a function of a number of transfer units. In both cases, countercurrent flow configuration with hot water inside the coil is the most effective.

The heat exchanger with surface modification on average has the largest effectiveness from all of the considered operational conditions. Instead of that fact it should be noticed that generally the difference between the effectiveness of both heat exchangers wasn't significant.

Figure 13 indicates that the effectiveness of the heat exchanger decreases with the increase in Dean number inside tube in case of reference and intensified heat exchangers. From the plot, it is also evident that for higher water flow rates inside the tube, effectiveness is almost constant in all cases. The analysis also indicates that the effectiveness of the helical

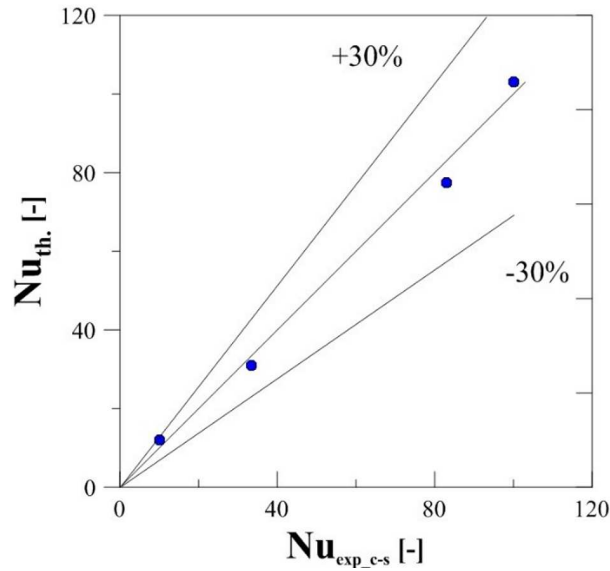


Figure 9: Comparison of experimental and theoretical Nusselt number for coil side in case of the unmodified surface.

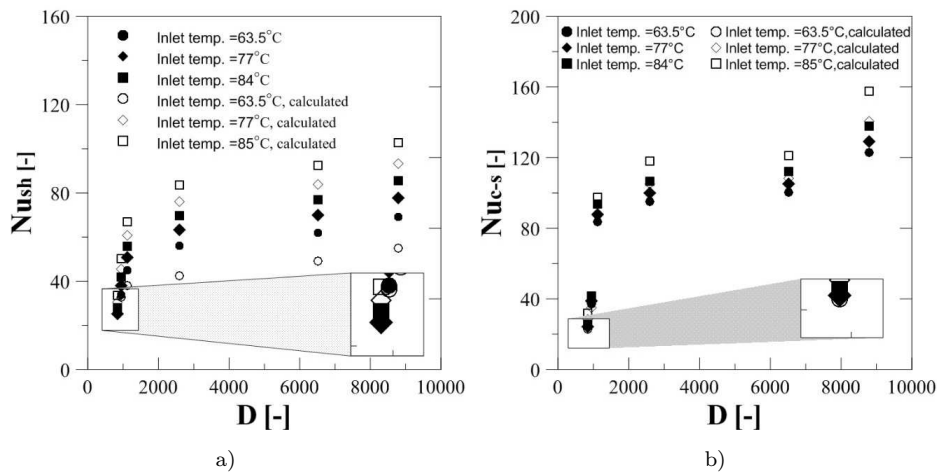


Figure 10: Variation of Nusselt number with Dean number for different fluid inlet temperature in case of unmodified surface: a) for shell side, b) for coil side.

coiled configuration is highest in case 'b)', for spiral coiled with external surface modification. Parallel flow configuration results with the effective-

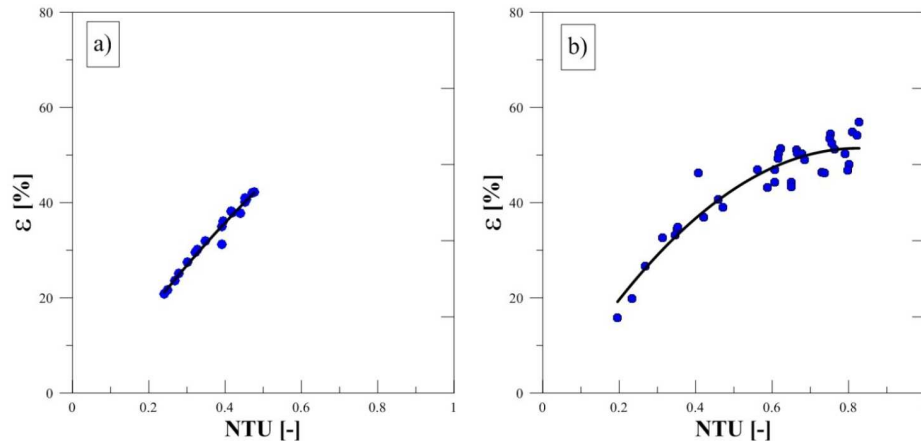


Figure 11: Experimentally obtained reference heat exchanger effectiveness in function of NTU for: a) parallel flow configuration, b) counter-flow configuration.

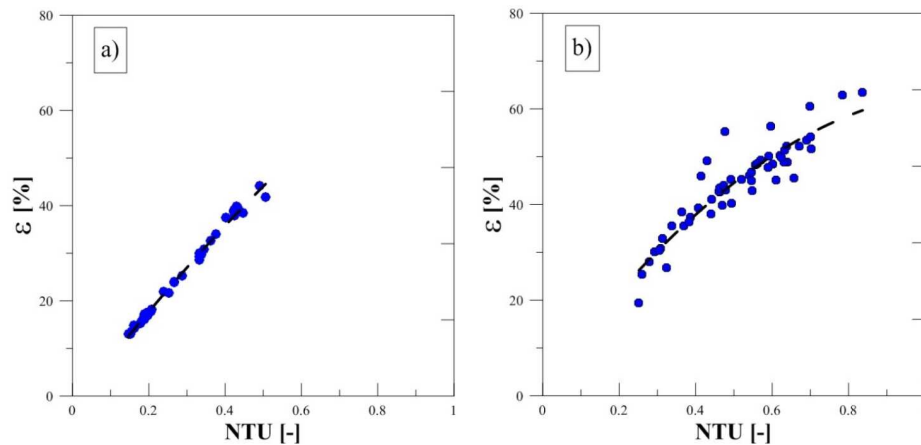


Figure 12: Experimentally obtained modified heat exchanger effectiveness in function of NTU for: a) parallel flow configuration, b) counter-flow configuration.

ness of intensified heat exchanger lower about 5% than reference type, but for lower mass flow rates. This can be explained by measurement error which is higher for lower flow rates.

Counterflow configuration also depicts similar effectiveness for low flow rates, but significantly larger for Dean numbers above 3000. In authors, opinion difference in results may be explained by entrance effects in both heat exchangers. For parallel flow at the inlet of heat exchanger heat is

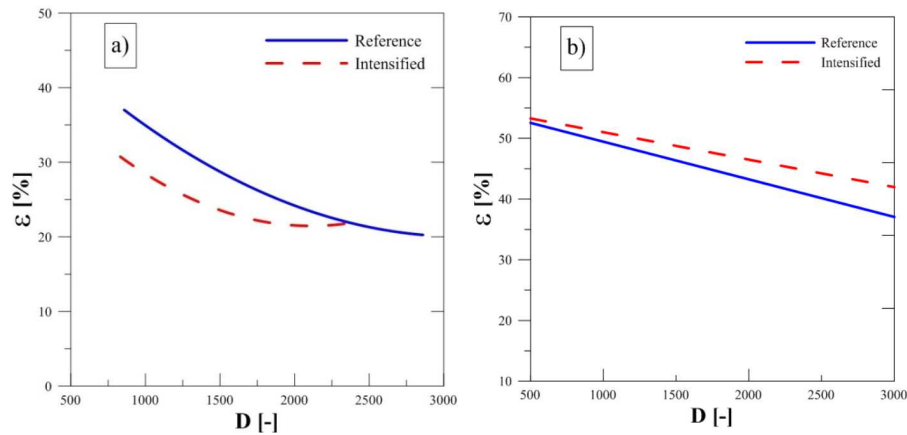


Figure 13: Effectiveness of helical coils heat exchanger, as a function of the Dean number ( $D$ ): a) parallel flow configuration, b) counter-flow configuration.

transferred due to the large temperature difference, also heat transfer coefficient is enhanced due to inlet effects, therefore surface enhancement does not play a significant role in it. Afterward with lower temperature difference in heat exchanger, enhancement of heat transfer coefficient falls within the measurement error. On another hand for counter flow configuration, working fluids have similar temperature gradient along the flow path, therefore after inlet effects are suppressed, modified surface offers heat transfer enhancement that is measurable due to the higher temperature difference.

## 6 Conclusions

Authors presented and successfully implemented, a simple mathematical methodology to model the shell and coil heat exchanger. In this paper, results show a comparison between helically coiled heat exchanger with surface modification by means of micro fins. During the experiments the mass flow rate in the inner tube and the annulus were both varied, both the counter and parallel flow configuration was tested. The experimental values of heat transfer coefficient have been obtained by the Wilson plot method.

It was observed that the overall heat transfer coefficient increases with increase in the inner coiled tube Dean number for a constant flow rate in the annulus region. Similar trends in the variation of overall heat transfer

coefficient were observed for different flow rates in the annulus region for a constant flow rate in the inner coiled tube. It was shown that obtained average Nusselt numbers for the shell side have increased with surface modifications.

The literature predictions for hydrodynamics and fully developed heat transfer were in good agreement with experimental results. The agreement with the numerical and experimental predictions of Nusselt number values was well within 30%.

As was expected based on presented above facts the heat exchanger with surface modification on average has larger effectiveness than reference construction.

Received 20 June 2016

## References

- [1] MUSZYNSKI T., KOZIEL S.M.: *Parametric study of fluid flow and heat transfer over louvered fins of air heat pump evaporator*. Arch. Thermodyn. **37**(2016), 3, 41–58, DOI:10.1515/aoter-2016-0019.
- [2] MUSZYNSKI T., ANDRZEJCZYK R.: *Heat transfer characteristics of hybrid microjet – Microchannel cooling module*. Appl. Therm. Eng. **93**(2016), 1360–1366, DOI:10.1016/j.applthermaleng.2015.08.085.
- [3] MUSZYNSKI T., ANDRZEJCZYK R.: *Applicability of arrays of microjet heat transfer correlations to design compact heat exchangers*. Appl. Therm. Eng. **100**(2016), 105–113, DOI:10.1016/j.applthermaleng.2016.01.120.
- [4] ROZZI S., MASSINI R., PACIELLO G., PAGLIARINI G., RAINIERI S., TRIFIRO A.: *Heat treatment of fluid foods in a shell and tube heat exchanger: Comparison between smooth and helically corrugated wall tubes*. J. Food Eng. **79**(2007) 249–254, DOI:10.1016/j.jfoodeng.2006.01.050.
- [5] JAYAKUMAR J.S., MAHAJANI S.M., MANDAL J.C., VIJAYAN P.K., BHOI R.: *Experimental and CFD estimation of heat transfer in helically coiled heat exchangers*. Chem. Eng. Res. Des. **86**(2008), 221–232, DOI:10.1016/j.cherd.2007.10.021.
- [6] BERGER S.A., TALBOT L., YAO L.S.: *Flow in curved pipes*. Annu. Rev. Fluid Mech. **15**(1983), 461–512.
- [7] KAKAÇ S., SHAH R.K., AUNG W.: *Handbook of single-phase convective heat transfer*. Wiley New York et al., 1987.
- [8] NAPHON P., WONGWISES S.: *A review of flow and heat transfer characteristics in curved tubes*. Renew. Sustain. Energy Rev. **10** (2006), 463–490, DOI:10.1016/j.rser.2004.09.014.
- [9] LIN C.X., ZHANG P., EBADIAN M.A.: *Laminar forced convection in the entrance region of helical pipes*. Int. J. Heat Mass Transf. **40**(1997), 3293–3304.

- [10] KUMAR V., FAIZEE B., MRIDHA M., NIGAM K.D.P.: *Numerical studies of a tube-in-tube helically coiled heat exchanger*. Chem. Eng. Process. Process Intensif. **47**(2008), 2287–2295.
- [11] CONTE I., PENG X.F.: *Numerical investigations of laminar flow in coiled pipes*. Appl. Therm. Eng. **28**(2008), 423–432.
- [12] PATANKAR S.V., PRATAP V.S., SPALDING D.B.: *Prediction of laminar flow and heat transfer in helically coiled pipes*. J. Fluid Mech. **62**(1974), 539–551.
- [13] JAMSHIDI N., FARHADI M., GANJI D.D., SEDIGHI K.: *Experimental analysis of heat transfer enhancement in shell and helical tube heat exchangers*. Appl. Therm. Eng. **51**(2013), 644–652, DOI:10.1016/j.applthermaleng.2012.10.008.
- [14] XIN R.C., AWWAD A., DONG Z.F., EBADIAN M.A.: *An experimental study of single-phase and two-phase flow pressure drop in annular helicoidal pipes*. Int. J. Heat Fluid Flow. **18**(1997), 482–488.
- [15] PETRAKIS M.A., KARAHALIOS G.T.: *Exponentially decaying flow in a gently curved annular pipe*. Int. J. Non. Linear. Mech. **32**(1997), 823–835.
- [16] PETRAKIS M.A., KARAHALIOS G.T.: *Fluid flow behaviour in a curved annular conduit*. Int. J. Non. Linear. Mech. **34**(1999), 13–25.
- [17] DI LIBERTO M., CIOFALO M.: *A study of turbulent heat transfer in curved pipes by numerical simulation*. Int. J. Heat Mass Transf. **59**(2013), 112–125.
- [18] MOAWED M.: *Experimental study of forced convection from helical coiled tubes with different parameters*. Energy Convers. Manag. **52**(2011), 1150–1156.
- [19] Designing\_Helical\_Coil\_Heat\_Exgr\_1982.pdf.
- [20] ANKANNA B.C., REDDY B.S.: *Performance analysis of fabricated helical coil heat exchanger*. Int. J. Eng. Res. **3**(2014), Iss. 1, 33–39.
- [21] KAST W., GADDIS E.S., WIRTH K.-E., STICHLMAIR J.: *L1 Pressure Drop in Single Phase Flow*. In: VDI Heat Atlas, Springer, 2010, 1053–1116.
- [22] BRAUER H.: *Strömungswiderstand und Wärmeübergang bei quer angeströmten Wärmeaustauschern mit kreuzgitterförmig angeordneten glatten und berippten Röhren*. Chemie Ing. Tech. **36** (1964) 247–260, DOI:10.1002/cite.330360314 (in German).
- [23] BELL K.J.: *Delaware Method for Shell-side Design*. Taylor & Francis, New York 1988.
- [24] ACHENBACH E.: *Investigations on the flow through a staggered tube bundle at Reynolds numbers up to  $Re = 107$* . Wärme-Und Stoffübertragung. **2**(1969), 47–52.
- [25] LAZOVA M., HUISSEUNE H., KAYA A., LECOMPTE S., KOSMADAKIS G., DE PAEPE M.: *Performance evaluation of a helical coil heat exchanger working under supercritical conditions in a solar organic Rankine cycle installation*. Energies. **9**(2016), 432, DOI:10.3390/en9060432.
- [26] JO D., AL-YAHIA O.S., ALTAMIMI R.M., PARK J., CHAE H.: *Experimental investigation of convective heat transfer in a narrow rectangular channel for upward and downward flows*. Nucl. Eng. Technol. **46**(2014), 2, 195–206, DOI:10.5516/NET.02.2013.057.

- 
- [27] HEWITT G.F., SHIRES G.L., BOTT T.R.: *Process Heat Transfer*. CRC press Boca Raton, FL, 1994.
- [28] MUSZYŃSKI T.: *Design and experimental investigations of a cylindrical micro-jet heat exchanger for waste heat recovery systems*. Appl. Therm. Eng. (2017), DOI:10.1016/j.applthermaleng.2017.01.021.
- [29] LASKOWSKI R.: *The concept of a new approximate relation for exchanger heat transfer effectiveness for a cross-flow heat exchanger with unmixed fluids*. J. Power Technol. **91**(2011), 93–101.
- [30] CIEŚLIŃSKI J.T., FIUK A., TYPIŃSKI K., SIEMIEŃCZUK B.: *Heat transfer in plate heat exchanger channels: Experimental validation of selected correlation equations*. Arch. Thermodyn. **37**(2016), 3, 19-29, DOI:10.1515/aoter-2016-0017.



## Notes for Contributors

---

ARCHIVES OF THERMODYNAMICS publishes original papers which have not previously appeared in other journals. The journal does not have article processing charges (APCs) nor article submission charges. The language of the papers is English. The paper should not exceed the length of 25 pages. All pages should be numbered. The plan and form of the papers should be as follows:

1. The heading should specify the title (as short as possible), author, his/her complete affiliation, town, zip code, country and e-mail. Please indicate the corresponding author. The heading should be followed by *Abstract* of maximum 15 typewritten lines and *Keywords*.
2. More important symbols used in the paper can be listed in *Nomenclature*, placed below *Abstract* and arranged in a column, e.g.:  
 $u$  – velocity, m/s  
 $v$  – specific volume, m/kg  
etc.  
The list should begin with Latin symbols in alphabetical order followed by Greek symbols also in alphabetical order and with a separate heading. Subscripts and superscripts should follow Greek symbols and should be identified with separate headings. Physical quantities should be expressed in SI units (*Système International d'Unités*).
3. All abbreviations should be spelled out first time they are introduced in the text.
4. The equations should be each in a separate line. Standard mathematical notation should be used. All symbols used in equations must be clearly defined. The numbers of equations should run consecutively, irrespective of the division of the paper into sections. The numbers should be given in round brackets on the right-hand side of the page.
5. Particular attention should be paid to the differentiation between capital and small letters. If there is a risk of confusion, the symbols should be explained (for example *small c*) in the margins. Indices of more than one level (such as  $B_{f_a}$ ) should be avoided wherever possible.
6. Computer-generated figures should be produced using **bold lines and characters**. No remarks should be written directly on the figures, except numerals or letter symbols only. Figures should be as small as possible while displaying clearly all the information requires, and with all lettering readable. The relevant explanations can be given in the caption.
7. The figures, including photographs, diagrams, etc., should be numbered with Arabic numerals in the same order in which they appear in the text. Each figure should have its own caption explaining the content without reference to the text.
8. Computer files on an enclosed disc or sent by e-mail to the Editorial Office are welcome. The manuscript should be written as a MS Word file – \*.doc, \*.docx or L<sup>A</sup>T<sub>E</sub>X file – \*.tex. For revised manuscripts after peer review process, figures should be submitted as separate graphic files in either vector formats (PostScript (PS),

Encapsulated PostScript (EPS), preferable, CorelDraw (CDR), etc.) or bitmap formats (Tagged Image File Format (TIFF), Joint Photographic Experts Group (JPEG), etc.), with the resolution not lower than 300 dpi, preferably 600 dpi. These resolutions refer to images sized at dimensions comparable to those of figures in the print journal. Therefore, electronic figures should be sized to fit on single printed page and can have maximum 120 mm x 170 mm. Figures created in MS World, Exel, or PowerPoint will not be accepted. The quality of images downloaded from websites and the Internet are also not acceptable, because of their low resolution (usually only 72 dpi), inadequate for print reproduction.

9. The references for the paper should be numbered in the order in which they are called in the text. Calling the references is by giving the appropriate numbers in square brackets. The references should be listed with the following information provided: the author's surname and the initials of his/her names, the complete title of the work (in English translation) and, in addition:
  - (a) for books: the publishing house and the place and year of publication, for example:  
[1] Holman J.P.: *Heat Transfer*. McGraw-Hill, New York 1968.
  - (b) for journals: the name of the journal, volume (Arabic numerals in bold), year of publication (in round brackets), number and, if appropriate, numbers of relevant pages, for example:  
[2] Rizzo F.I., Shippy D.I.: *A method of solution for certain problems of transient heat conduction*. AIAA J. **8**(1970), No. 11, 2004–2009.

For works originally published in a language other than English, the language should be indicated in parentheses at the end of the reference.

Authors are responsible for ensuring that the information in each reference is complete and accurate.

10. As the papers are published in English, the authors who are not native speakers of English are obliged to have the paper thoroughly reviewed language-wise before submitting for publication.

**Manuscript submission** Manuscripts to be considered for publication should be electronically submitted to the Editorial Office via the online submission and reviewing system, the Editorial System, at <http://www.editorialsystem.com/aot>. Submission to the journal proceeds totally on line and you will be guided stepwise throughout the process of the creation and uploading of your files. The body of the text, tables and figures, along with captions for figures and tables should be submitted separately. The system automatically converts source files to a single PDF file article, for subsequent approval by the corresponding Author, which is then used in the peer-review process. All correspondence, including notification confirming the submission of the manuscripts to the Editorial Office, notification of the Editors's decision and requests for revision, takes place by e-mails. Authors should designate the corresponding author, whose responsibility is to represent the Authors in contacts with the Editorial Office. Authors are requested not to submit the manuscripts by post or e-mail.

The illustrations may be submitted in color, however they will be printed in black and white in the journal, so the grayscale contributions are preferable. Therefore, the figure

caption and the entire text of the paper should not make any reference to color in the illustration. Moreover the illustration should effectively convey author's intended meaning when it is printed as a halftone. The illustrations will be reproduced in color in the online publication.

**Further information** All manuscripts will undergo some editorial modification. The paper proofs (as PDF file) will be sent by e-mail to the corresponding author for acceptance, and should be returned within two weeks of receipt. Within the proofs corrections of minor and typographical errors in: author names, affiliations, articles titles, abstracts and keywords, formulas, symbols, grammatical error, details in figures, etc., are only allowed, as well as necessary small additions. The changes within the text will be accepted in case of serious errors, for example with regard to scientific accuracy, or if authors reputation and that of the journal would be affected. Submitted material will not be returned to the author, unless specifically requested.

A PDF file of published paper will be supplied free of charge to the Corresponding Author.

Submission of the manuscript expresses at the same time the authors consent to its publishing in both printed and electronic versions.

**Transfer of Copyright Agreement** Submission of the manuscript means that the authors automatically agree to assign the copyright to the Publisher. Once a paper has been accepted for publication, as a condition of publication, the authors are asked to send by email a scanned copy of the signed original of the Transfer of Copyright Agreement, signed by the Corresponding Author on behalf of all authors to the Managing Editor of the Journal. The copyright form can be downloaded from the journal's website at <http://www.imp.gda.pl/archives-of-thermodynamics/> under Notes for Contributors.

*The Editorial Committee*